Propagating Laminar Flame Characteristics for Single and Two Phase Alternative Fuel Mixtures

Daniel de la Rosa-Urbalejo

A thesis submitted for the degree of Doctor of Philosophy

Cardiff School of Engineering

Cardiff University

September 2014

Declaration

This work has not previously been accepted in substance for any degree and is not concurrently in submitted in candidature for any degree.

Signed ………………………………………………. (Daniel de la Rosa-Urbalejo) Date ………………………….

STATEMENT 1

This thesis is being submitted in partial fulfillment of the requirements for the degree of ………………………. (insert MCh, MD, MPhil, PhD etc, as appropriate)

Signed ………………………………………………. (Daniel de la Rosa-Urbalejo) Date ………………………….

STATEMENT 2

This thesis is the result of my own independent work/investigation, except where otherwise stated. Other sources are acknowledged by explicit references.

Signed ………………………………………………. (Daniel de la Rosa-Urbalejo) Date ………………………….

STATEMENT 3

I hereby give consent for my thesis, if accepted, to be available for photocopying and for interlibrary loan, and for the title and summary to be made available to outside organisations.

Signed ………………………………………………. (Daniel de la Rosa-Urbalejo) Date ………………………….

Abstract

This thesis investigates enhanced methods for analysing non-linear effects in propagating laminar flames, enabling more accurate evaluation of laminar flame characteristics such as Markstein length and unstretched flame speed whilst proposing a new method for evaluating extinction stretch rate. Furthermore, a new cloud-combustor is developed and commissioned enabling laminar flame characteristics through droplet fuel mists to be explored again utilising advanced non-linear analysis.

Re-analysis of previous low-ignition energy methane-water flames reveals the analytical non-linear characteristic. The analysis also demonstrates the need for a larger chamber to avoid pressurised effects during the latter stages of propagation, potentially reducing the accuracy of the adopted methodology. Non-linear analysis shows interesting trends concerning Markstein length at higher water loading in particular when it increase to 15% (by volume), and laminar burning rate decreased.

The non-linear analysis technique is deployed to analyse four hydrocarbon fuels, two traditional paraffinic fuels in methane and propane, and two alternative alcohol fuels namely ethanol and methanol.

It is shown that overdriven flame data can be used to predict flame extinction stretch rate, as long as a sufficient time period is disregarded to allow the effects of the early ignition-affected period to subside. The new technique proposed for evaluated critical extinction stretch rate shows good agreement with the traditional counter-flowing flame technique. Results for the four fuels reveal a common profile for extinction stretch-rate as a function of equivalence ratio, which was anticipated due to the similar fundamental combustion characteristics of the chosen fuels. Based on the non-linear analysis, it is shown analytically that this common profile may be represented by a combination of the unstretched laminar burning velocity, the Markstein length and the expansion ratio of the fuel.

Ethanol in air is used to benchmark Cardiff University’s new, large 35Litre ‘Cloud Combustor’ for an investigation of flame propagation through fuel mists across a wide range of equivalence ratios. Non-intrusive, in-situ droplet sizing with concurrent flame propagation is achieved for the first time. The fuel mist flame data was subsequently compared to that for pure vapour mixtures at nominally identical ambient conditions in order to study the reported enhancement in flame speed exhibited in previous studies, and to compare qualitatively against conflicting published views reported in literature. It was found that with the onset of instabilities at certain droplet size an enhancement in flame speed could be shown for rich mist flames compared to those of analogous vapour flames.

Based on mechanisms detailed elsewhere that provide a possible explanation for this enhancement full discussion and correlations that help to understand the nature of flame speed through droplet mists are presented.

Acknowledgements

First and foremost, I would like to thank God for giving me wisdom and guidance throughout my life.

I would like to thank the Mexican National Council of Science and Technology, CONACyT for their financial support of this work.

I wish to express my gratefulness to my supervisors, Prof. Philip J. Bowen and Dr. Andrew P. Crayford for their continuous supervision, positive discussions and important ideas through this research work.

Also, very extraordinary deepest thanks to Dr. Agustín Valera-Medina for his special contribution and help in completing this work.

My deepest thanks, love and gratitude to all of my family. Special thanks to my mom (†), my dad, my brother, cousins, aunts, uncles and grandparents. And extraordinary thanks to my dearest wife Karla for her love, understanding, patience and tremendous support during these years.

I would like to extend my thanks to the staff of the Gas Turbine Research Centre (GTRC), the staff of Cardiff University School of Engineering and the staff of the Mechanical Engineering Workshop for their expert advice, support and technical assistance provided; special thanks to Daniel Pugh, Paul Malpas, Malcolm Seabourne and Gareth Hunt.

To all my friends scattered around the world for listening, offering me advice, and supporting me through this entire process. Thanks for your thoughts, well-wishes/prayers, phone calls, e-mails, texts, visits, dinners, parties, editing advice, and being there whenever I needed for a friend.

List of publications and conference papers

1. Crayford, A.P., Bowen, P.J., de la Rosa, D., Tam, V.H.Y., 2011, "Laminar Burning Characteristics of Methane/Water-Vapour/air Flames", 5th European Combustion Meeting, Cardiff, Wales.

2. de la Rosa, D., Bowen, P.J., Crayford, A.P., Valera-Medina, A., 2012, "Influence of Ambient Conditions on Laminar Burning Velocity, Ignition and Flame Extinction for Ethanol-Air Mixtures", ASME Turbo Expo 2012, Copenhagen, Denmark.

3. de la Rosa, D., Bowen, P.J., Crayford, A.P., Valera-Medina, A., Pugh, D., 2014, "Non-linear Analysis of Outwardly Propagating Flames to Determine Extinction Stretch Rate" (submitted to Combustion and Science Technology journal).

Nomenclature

Latin symbols

A	Surface area
AFR	Air fuel ratio
AFR_{actual}	Actual air fuel ratio
AFR_{stoich}	Stoichiometric air fuel ratio
C_p	Specific heat
CAC	Compressed Air Cylinder
CCVC	Cylindrical Constant Volume Chamber
CM1	Concave Mirror 1
CM2	Concave Mirror 2
c	Capacitance
D	Mass diffusivity
D_i	Droplet diameter in the i th-size class
D_{32}	Sauter mean diameter
DAS	Data Acquisition System
DCCVC	Dynamic Cylindrical Constant Volume Chamber
d_m	Mean droplet diameter
d_o	Droplet diameter
E_a	Activation energy
EI	Electronic Interface
EOC	Emitter Optic Canister
e	Energy
GFC	Gaseous Fuel Cylinder
HSC	High Speed Camera
K_{ext}	Extinction stretch rate
KEA	Knife-Edge Aperture
Ka	Karlovitz number
k	Thermal diffusivity
LS	Light Source
L_b	Burned gas Markstein length
Le	Lewis number
MFC	Mass Flow Controller
M_{fuel}	Molar mass of fuel
m_{fuel}	Mass of fuel
M_{ox}	Molar mass of oxidizer
m_{ox}	Mass of oxidizer
n_{fuel}	Number of moles of the fuel
n_i	Droplet number in the i th-size class
n_{ox}	Number of moles of the oxidizer
P	Pressure/Pre-ignition pressure
PCA	Pneumatic Cylindrical Actuator
P1	Piston (1)
Pe_{cr}	Critical Peclet number
P_{fuel}	Fuel partial pressure
P_{fuel}^{0}	Vapour pressure of liquid fuel
P_{ox}	Oxidizer partial pressure

P_0	Pre-expansion pressure
P_T	Total pressure
ROC	Receiver Optic Canister
R_{fuel}	Specific gas constant of fuel
R_{ox}	Specific gas constant of the oxidizer
R_u	Universal gas constant
r_f	Flame front radius
r_{cbg}	Completely Burned Gas radius
r_{fpz}	Preheat Zone flame front radius
r_{sch}	Schlieren flame front radius
r_w	Wall radius
S_L	Unstretched flame speed
S_{L38}	Unstretched flame speed of flame radius 38mm
S_{Lmax}	Maximum unstretched flame speed
S_n	Stretched flame speed
SMD	Sauter Mean Diameter
T	Temperature/Pre-ignition temperature
T_f	Equilibrium temperature
T_{fuel}	Fuel temperature
T_i	Ignition temperature
T_{ox}	Oxidizer temperature
Tr	Laser transmittance
T_u	Temperature of the unburned gas
T_0	Pre-expansion temperature
TCU	Temperature Control Unit
t	Time
S_{n48}	Flame speed at flame radius of 48 mm
u_L	Laminar burning velocity
V	Voltage
V_w	Water vapour
Vol	Volume of the chamber
VGD	Vacuum Gauge Display
VP	Vacuum Pump
$\bar{x}$	Arithmetic mean

Greek Symbols

α	Flame stretch rate
α_c	Flow field strain rate
α_{Cr}	Critical stretch rate
α_s	Flame curvature
δ	Flame thickness
λ	Thermal conductivity
ρ	Density
σ	standard deviation
$Ø$	Equivalence ratio
$Ø_{eff}$	Effective equivalence ratio
$Ø_o$	Overall equivalence ratio
$Ø_g$	Gaseous equivalence ratio
$Ø_l$	Liquid fuel equivalence ratio

Table of Contents

List of Figures

Chapter 1

> *“We build too many walls and not enough bridges.”*
>
> **Isaac Newton**

Introduction

1.1 Energy production and Climate Change

In recent years the impact of unconventional gas and oil resources on the non- and renewable energy sectors has changed the forecast market trend and fuel prices, mainly because it is expected that industries such as shale gas may contribute to supply growth. However, technology challenges, infrastructure requirements and most importantly the concern of global warming and climate change policies have an important effect on energy production. Nowadays, the world is facing up to the problem of supplying the energy demand and addressing the environmental concerns.

In an environmentally more conscious world, it is becoming ever more critical to tackle the increase of greenhouse gas emissions (GHGE) released into the atmosphere. For example, natural gas is receiving more attention as it represents a cleaner burning alternative than other fossil fuels such as coal for power generation. Moreover, according to Schumann et al. [1] unconventional gas represents more than 40% of domestic gas production in the U.S.A. and more than 10% of world output, it is expected that by 2030 natural gas will be the twice that of oil to meet energy demand.

In addition to the increasing public interest to abate the emissions effects on atmosphere, the International Energy Agency (IEA) in its 2012 Renewable Energy Outlook [2] states that electricity generation from renewables is likely to triple from 2010 to 2035, mainly because of government support, falling costs, CO_2 pricing in some regions, and rising price of fossil fuels. In the long term, IEA predicts that 31% of total generation and comprising hydropower, wind, solar and biofuels. According to this outlook, biofuels production will triple in the same period due to blending mandates, with ethanol dominating demand of biofuels of transport industry.

In terms of legislation, the UK commitment to mitigate climate change is specified in the Climate Change Act of 2008 [3] which mandates and establishes all the measures to be adopted in order to reduce UK emissions in agreement with the aims set by the Kyoto Protocol (1997). In the year the aforementioned Act was published, a report was released setting the targets of a reduction of 80% of GHGE and 34% by 2050 and 2022, respectively. The latest target is likely to rise in the future if an international agreement is reached at the UN Climate Change committee.

1.2 World energy consumption outlook

According to the International Energy Outlook 2013 [4] for the 2010 – 2040 projected period published by the U.S. Energy Information Administration, an increase of 56% in the world energy consumption is projected. This increase is mainly driven by emerging economies where strong, long-term economic growth is expected. Moreover, 80% of the world’s energy use through 2040 is still supplied by fossil fuels; mostly because of the fast growth of natural gas driven by the increasing supplies of tight gas, shale gas and coalbed methane. In addition to these trends, coal use grows faster than petroleum until after 2030 due to a projected increase in China’s consumption.

Furthermore, this outlook also shows that the energy sources with the world's fastest growth – 2.5% per year – are renewable energy and nuclear power. It can be seen in **Figure 1.1** the growth in renewable sources for electricity generation is comprised mostly of hydropower and wind power.

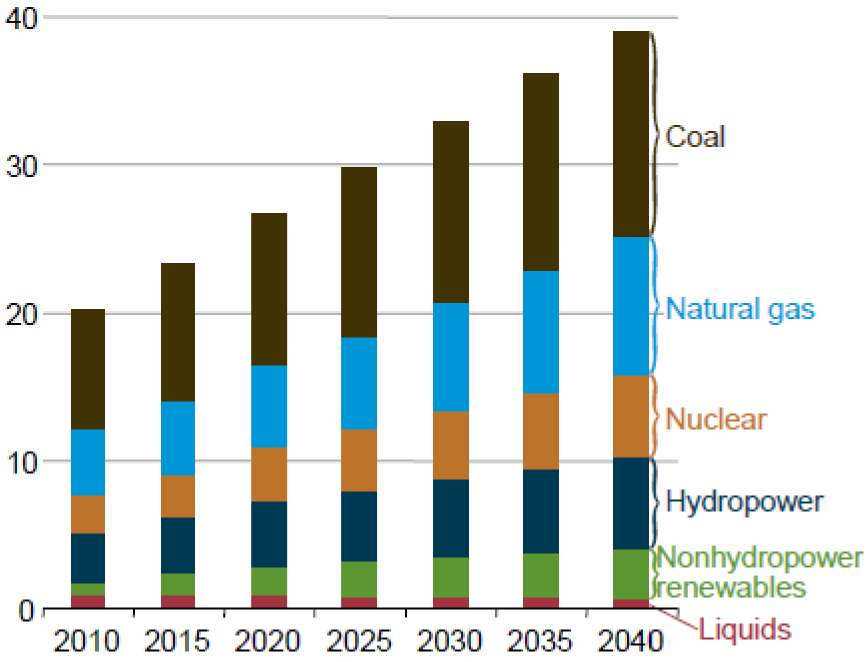

Figure 1.1 World net electricity generation by energy source, 2010-2040 (trillion kilowatt-hours) [4].

Although these trends reflect a relatively small contribution from liquid biofuels in electricity generation compared to other sources, there are certain issues with those sources in their long term use. For instance, the intermittency of wind, consequences of the Fukushima Daiichi disaster, optimal control of the water levels in hydroelectric facilities, public opposition to the fracking technique for environmental impact and the increasing levels of CO_2 in the atmosphere produced by a heavier reliance on coal. Despite the fact that biofuels are also subject to certain legitimate concerns such as food crops supply, there is a possibility that liquid biofuels can contribute in a wider range to the diversification not only in the transport sector but in the electricity market favoured by their use on aeroderivative gas turbines.

1.3 Liquid biofuels in aeroderivative gas turbines

Due to gradual economic and political incentives towards the use of biofuels affected by fuel volatility and environmental sustainability, several efforts have been undertaken to meet GHGE reduction targets. One of these attempts is reported by General Electric [5] in which liquid fuels such as ethanol and biodiesel are used in aeroderivative gas turbines for power generation, the marine industry and research purposes. It was reported that fuel switching incurred little change in the turbine performance. Lower levels of NO_X, CO_2 and particulates emissions were produced compared with diesel. Moreover, internal parts and exhaust filters of the turbine were cleaner after operation. This example shows some of the additional benefits of using alternative fuels instead of the conventional fossil fuels.

On the other hand, issues with biodiesel are apparent, such as rising fuel prices; gas turbine was started on gas, and one unit was not able to reach full power for the same flow volume. Other detrimental effects of biodiesel compared to diesel on power generation units are that gaskets and seals do not last as long when exposed to biodiesel, its lower heating value, its reduced shelf life thus requiring its time-limited utilisation, and its affinity for water. However, this report also concludes that ethanol in comparison to biodiesel presents fewer issues, though its use requires changes to gas turbines and combustion systems due to its lower lubricity and low heating value when it is produced from sugar cane.

Although fossil fuels will remain as the primary source of transportation and power generation for at least a decade or so to come, until biofuels become cheaper, it is important to investigate the use of liquid biofuels during this transition period, for instance in power generation via aeroderivative gas turbine, or in the automotive sector.

Therefore, it is crucial to study the impact of fuel flexibility on the turbine industry in terms of operability and reliability success.

As a biofuel, ethanol represents a viable source of energy. It offers low impact on the air quality when used to replace conventional gasoline in engines due to the elimination of aromatic hydrocarbons (such as benzene) which are particularly toxic. Carbon monoxide emissions have also been shown to be drastically reduced [6]. In addition to environmental benefits, other incentives for ethanol production have been supported by the agricultural sector, as this fuel represents an option in national energy security [7]. Experimental results obtained in a counter-flow burner with fuel-lean mixtures [8] concluded that alcohols (including ethanol) appeared to be more resistant to extinction than some hydrocarbons for the same equivalence ratio.

Wang et al. [9] noted that it is attractive to obtain information related with experimental extinction stretch rates in order to study the reduction of pollutant emissions from turbulent flames witnessed in engine combustion, thus preventing extinction by stretch as a consequence of flame curvature. In the gas turbine industry, extinction tests are usually required to determine a wide range of operating conditions with high levels of combustion efficiency [10].

General Electric (GE) [11] reported a successful experience using pure ethanol in aeroderivative gas turbines for power generation in Brazil in 2010.

The article presents the launching of the world’s first ethanol-fired power plant which has an installed capacity of 87MW, equivalent to power a city of 150,000 inhabitants. These facilities are planned to supply power for ten years.

General Electric was in charge of the two units (GE LM6000) conversion which involved the replacement of the combustion chambers and injector nozzles along with installing peripheral equipment, such as recipient system, tanks, pumps and filters. Little difference in turbine performance was achieved during a five-month demonstration testing engine, equipment, and .environmental concerns. These tests outline the significantly lower amount of CO_2 emissions and water usage; highlighting that in comparison with natural gas and diesel-fired plants, lower levels of NO_X were released without lowering its power generating capacity.

Methanol also has found application in electricity generation. For example, it has the potential to be used in stationary gas turbine engines for peak generation during times of great electricity demand. This crucial backup application makes it ideally suited for bolstering the electric grid’s capacity in a more environmentally friendly way to cover the demand of power. Because of its better heat rate, higher power output – due to the higher mass flow, and lower NO_X emissions are obtained due to the lower flame temperature relative to natural gas and distillates.

Methanol is readily fired and is a fully feasible option as an alternative gas turbine fuel [12]. However, some technical issues such as low heating value, low lubricity, and low flash point make it necessary to do some modifications in the turbine. Despite these concerns, General Electric has demonstrated through some tests [12] that methanol can be successfully burned in GE heavy-duty combustors without requiring major modifications to them; considering this alternative fuel as a superior turbine fuel with the promise of low emissions, excellent heat rate and high power output.

Among its benefits such as lower maintenance costs in the power generation industry, not only ethanol but methanol have been tested in projects involving dual-fuelled gas turbines, exhibiting great viability in its use for island nations and other areas not situated near gas pipelines [13].

The increasing interest in energy efficiency and the security of energy has heightened the need for the study of alternative fuels in combustors at different regimes. Of particular interest to the present study is the measurement of extinction stretch rates at different initial conditions in spherical expanding flames for alternative fuels and the instabilities exhibited during flame propagation in droplet clouds that can lead to an enhance in burning rate compared to those of gaseous flames. This fuel characteristic is particularly influential in stabilising turbulent flames in practical combustors.

Gas turbine manufactures are in constant search of solutions toward greater suppression of NO_X formation. Because of this need, low NO_X combustion systems operate in lean premixed mode near extinction limits. This adjustment implies the challenge to work in a region where the quantity of air/fuel ratio at the burner is barely sufficient to sustain combustion at low flame temperatures while maintaining combustion stability over the broader possible operating range [14]. Because of this concern, it makes it attractive to fire biofuels in gas turbines as some alcohols present higher resistance to extinction at lean region compared with some hydrocarbons.

Droplets and spray combustion are of practical importance in a wide range of applications such as gas turbines. According to Lefebvre [10] atomisation quality affects the combustion efficiency, stability, operating temperatures, emission rate, and pattern factor of gas turbine engines. In the 1880s, spray or aerosol combustion was used as a method of burning relatively involatile liquid fuels due to an increasing of the surface area per unit mass and hence the rates of heat and mass transfer increase as well in small fuel droplets [15]. However, fundamental understanding of two-phase droplet-mist combustion and flame propagation is relatively immature.

1.4 Aims and Objectives

This thesis aims to analyse characteristics of stretched laminar flames, particularly during the sensitive early stage of flame-kernel development, for alternative fuels in gaseous, vapour or droplet-aerosol form enabled by low energy ignition and utilising an advanced non-linear analysis technique. The objectives of the research are to:

- Appraise a statistical method for upgrading low-speed imaging data to derive laminar flame characteristics including unstretched flame speed and Markstein length for methane/water mixtures in air.
- Utilising non-linear analysis from low-ignition flame propagation, appraise a novel methodology for determining extinction stretch rate from propagating flames, comparing the results with albeit limited previous results using the traditional counter-flowing flame technique, assessing the influence of ignition energy and also the potential for re-analysing previous historical data from over-driven flames.
- Assess the influence of initial ambient conditions on these under-driven flames.
- Develop a new, unique integrated 'cloud-combustor' for creating homogeneous, quiescent fuel mists with in-situ measurement of mono-disperse droplet size based on the Wilson cloud chamber principle. Fully integrate the combustion systems and diagnostics for concurrent mist/flame characterisation.
- Utilise the new integrated 'Cloud-Combustor' together with the non-linear analysis technique developed in the earlier single phase studies to generate stretched laminar flame characteristics and derived variables for the alternative fuel ethanol.

- Investigate leading to the onset of instabilities induced by the presence of aerosol clouds of different droplet diameters and overall (and liquid) equivalence ratios and attempt to correlate findings.

1.5 Thesis structure

A comprehensive review of previous laminar premixed flame propagation studies in both gaseous and droplet mist mixtures has been undertaken. A broad range of extinction stretch rate research studies using the well-established counter-flow technique is also presented in Chapter 2.

Chapter 3 describes in detail the test facilities, methods and procedures deployed during the experimental programmes.

Chapter 4 presents and analyses results obtained of the effects of equivalence ratio, water concentration, initial temperature and ignition energy on outwardly-propagating spherically flames, highlighting the study of the low ignition energy system in order to enable the early non-linear stages of the flame propagation against stretch rate. A thorough investigation of a proposed method for evaluating the extinction stretch rate (K_{ext}) using spherical flame propagation is presented for the first time in this chapter.

Chapter 5 appraises the non-linear trends observed during the early stages of flame propagation for ethanol-vapour/air mixtures, including the effect of ignition energy, initial pressure, initial temperature, and the evaluation of the critical stretch rate.

Chapter 6 presents data for outwardly propagating stretched spherical flame for four fuels, namely methane, propane, methanol and ethanol, within the non-linear relationships between flame stretch and flame speed enabling a critical appraisal of an alternative methodology proposed for determining extinction stretch rate. Flame extinction across a range of equivalence ratios at various ambient conditions in under-driven flames are studied for each of the fuels, and the hypothesis is compared against limited published data from the traditional counter-flowing flame technique or chemical kinetic schemes.

In Chapter 7, ethanol in air was chosen to benchmark and investigate droplet flame propagation across a wide range of equivalence ratios at the same conditions as those of corresponding gaseous flames in order to study and contrast two-phase with single phase flame propagation characteristics.

The overall conclusions determined from this work and further recommendations for future work are discussed in Chapter 8.

Chapter 2

“Curiosity will conquer fear even more than bravery will.”

James Stephens

The Crock of Gold (1912)

Literature Review

2.1 General

The understanding of laminar premixed flame propagation in both gaseous and droplet mist mixtures is relevant for many combustion applications. With the development of new numerical models and the availability of new experimental techniques scientists and engineers have attempted to clarify fundamental comprehension of the factors controlling flame propagation. Despite the fact that extinction stretch rates have been previously determined using counter-flow systems, similar analogies utilising spherical expanding flames have yet to be employed in order to determine this parameter. Previous studies have suggested this exponent may be measured from spherical flames but at present this is not scientifically appraised, and it is suggested that in order to extend the analysis the effects of initial ignition energy on flames with pronounced under-driven characteristics, will first need to be clarified. Several important observations have been reported regarding enhancement of laminar flame propagation when comparing a pure gaseous fuelled flame to that of a flame in a dense cloud of ‘fine’ droplets; however, few experimental works have been concerned with the correlation between burned Markstein length and laminar flame enhancement in droplet mists. A summary of research carried out in this field is presented below emphasising the two aforementioned aspects.

2.2 Laminar Burning Velocity

The research of laminar burning velocity is associated with many complex concepts interacting on a flame which according to Griffiths and Barnard [16] is defined as: “the cause of a self-propagating exothermic reaction which usually has a luminous reaction zone associated with it”. In addition, Lefebvre and Ballal [10] also gave a more detailed definition which established a flame: “as a rapid chemical change occurring in a very thin fluid layer, involving steep gradients of temperature and species concentrations, and is accompanied by luminescence”.

Another concept relates flame characterisation with the flame front which Rallis and Garforth [17], in their extensive review, presented as “the region in which the unburned gas is heated and converted into products”. This flame front is of a finite thickness and is taken as an indication of the progress of the flame. Furthermore, the authors also exhibited a temperature profile through a flame front which is comprised by two regions, the preheat zone and reaction zone as shown in **Figure 2.1**.

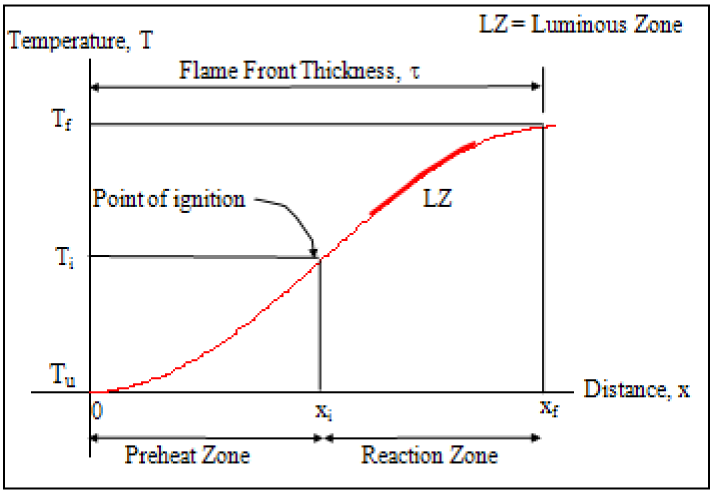

Figure 2.1 Typical temperature profile through a flame front [17].

In this profile it is shown that in the preheat zone, there is a spatial layer between the cold boundary at that of the temperature of the unburned gas (T_u) and the location of the ignition temperature (T_i). The temperature of the unburned gas is raised mainly by heat conduction and some convection from the reaction zone. Because of the temperature increase the unburned gas expands, with decreasing density and is thus accelerated, however, no significant chemical reaction occurs in this zone.

On reaching its ignition temperature, chemical reactions are activated within the flammable mixture producing an evolution of heat release. The temperature continues to rise until an equilibrium temperature (T_f) is reached. Finally, a flame front thickness is established and shown as the distance between the cold and hot boundaries of the flame front which comprises both preheat and reaction zones.

Another two important concepts in the study of self-propagating flame are deflagration and detonation. Lefebvre and Ballal [10] defined deflagration as a fast process by which a flame propagates through an unburned mixture. Compared to the unburned mixture, the burned gases are higher in volume and temperature, and much lower density leading to relatively lower flame speeds. Deflagration waves, for example, in hydrocarbon fuel-air mixtures normally burn at velocities below 1 m/s, typical propulsion and power generation combustion systems e.g. gas turbine combustors fall within this category of combustion. Thus in summary this mode of propagation is primarily associated with molecular thermal conductivity and diffusion [18].

On the other hand, the main characteristic of detonation is the existence of a shock wave that is connected with and supported by the zone of chemical reaction. Detonation waves precede the flame front at supersonic velocities, ranging between 1 and 4 km/s causing a rapid compression of the inflammable mixture by the shock wave. Chemical reactions take place at high rate due to the shock wave rapidly compressing and heating the unburned mixture, causing the (T_i) to be locally exceeded. The shock wave propagates over large distances as a result of the intensive heat release in the chemical reaction [18].

A great number of fundamental studies of flame combustion have been performed using gaseous or pre-vaporised fuels. Although a flame can propagate through a static gas mixture, it is also possible to stabilise the flame at a fixed point by supplying it with a continuous flow of combustible mixture, with these flames often referred to as stationary flames. Under these conditions, flames can be divided into two main classes namely; premixed flames and diffusion flames. Within premixed flames the fuel and oxidant are thoroughly mixed before the active combustion zone whereas in the case of diffusion flames they are mixed by diffusion within the flame zone. As a subset of the aforementioned flames, they can also be classified depending on the prevailing flow regimes, e.g. laminar or turbulent flow.

Griffiths and Barnard [16] state that in premixed gases a combustible mixture is available from the outset. Once the flame has been initiated at some point in the mixture; by means of the hot surface, and electric spark, or some other ignition source, the flame propagates throughout the entire volume of the combustible mixture. Of special interest to the designer of practical combustion systems are the speed at which the combustible mixture and the factors affecting its rate of propagation. Turbulence is of prime importance because most flowing fuel-air mixtures are turbulent and turbulence is known to enhance flame speeds considerably.

According to Kuo [19] first premixed flame experiments were undertaken in 1857 by using a Bunsen burner [20]. One of the seminal theoretical works was produced by Mallard and Le Chatelier [21] who developed the classical laminar flame theories in which the authors studied chemical and physical processes of the flame front, subdividing it into the preheat and reaction zones. Their theory proposed that laminar burning velocity, designated herein as u_L, is proportional to chemical reaction rate and based on Arrhenius law expressed as follows by **Eqn. 2.**:

$$u_L \propto e^{E_a/2R_uT} \tag{2.1}$$

Zeldovich and Frank-Kamenetsky [22] expanded Mallard and Chatellier's theory of premixed laminar flames by using energy equations and species conservation equations that relate u_L with the chemical reaction rate. This theory was valid for high energy reactions and did not predict results accurately, but showed the trend of the flame propagation.

Lewis and Von Elbe [23] by accounting in their model the combined effects of heat flux and diffusion, achieved a good correlation between experimental results and theoretical approximations of the determined flame speed. Improvements to the experimental techniques were made in flame propagation measurement methods; for example, Stevens [24] developed the soap-bubble method and the transparent observation of optical flame growth was subsequently introduced by Chamberlain and Clarke [25].

A review of the experimental techniques to measure the flame speed was presented by Fiock and Marvin [26], in which they showed that optical methods such as soap-bubble and confined chamber could be correlated against pressure rise times. Furthermore, Von Elbe and Lewis [27] introduced a particle tracking technique that improved the flame speed measurement. With the use of a burner that employed glass beads, wire mesh and small diameter tubes, combustion of quasi-laminar flat flames was achieved by Powling [28]. Later Botha and Spalding [29] adapted a water cooled system for Powling's burner, provoking the technique to become known as the flat flame heat flux method.

In 1947 Tanford and Pease [30] derived an equation for burning velocity based on the effect of diffusion of active particles from the flame front on combustion. The main assumption of this equation was that the diffusion of radicals into the unburned gas had a greater effect on the determination of burning velocity than the gradient of temperature.

The study of $\boldsymbol{u_L}$ subsequently gained greater importance due to the fact that it could be used to establish further analyses of the fuel behaviour related to premixed operational instabilities such as extinction, flash back and blow off, along with turbulent flame culminating in numerous propagation characterization studies [31-33]. According to Law [31], this physicochemical property is intrinsic of any given combustible mixture and indicates “its reactivity and exothermicity in a given diffusive medium”. However it is observed that the values of $\boldsymbol{u_L}$ quoted differ not only due to initial conditions such as composition, pressure and temperature, but also due to the particular measurement techniques employed [34-36].

Due to the importance of extracting accurate values of $\boldsymbol{u_L}$, for different combustible mixtures, several measurement techniques of flame propagation were reviewed by Rallis and Garforth [17]. The authors noted that one of the most versatile and accurate measurement techniques is that of the constant-volume vessel method. This method consists of the ignition of a quiescent, homogeneous combustible mixture from central point, resulting in the propagation of a flame throughout the container mixture. Several types of bounding surface have been used, for instance, rigid cylindrical tubes, either enclosed at both ends or open at one; soap bubble or thin elastic membranes solutions, and rigid spherical vessels. Large spherical vessels are one of the best techniques neglecting wall surface effects that could cause heating, quenching or catalytic consequences to the measured flame front.

Classical works that contributed to the evolution of this technique, for example, are those made by Wheeler [37] who observed that the subsequent spread of flame was determined by numerous effects namely; the nature of the boundary that encloses the mixture, the intensity of the ignition point, and the ambient condition of the combustible mixture. Moreover, in 1928 Payman [38] investigated the propagation of many fuels presenting the potential change at different conditions, and also the influence of the confining area on flame propagation [39].

It was also stated that flame propagation is influenced by aerodynamic strain generated by surface curvature. The rates at which stretch occurs during propagation were first investigated by Karlovitz et al. [40], it was proposed that the influence of changes in surface velocity gradient experienced by the flame during its propagation, considered as localised speed is related to the change of surface area (***A***) of the evolving flame front. Result outcome of this investigation was the necessity to consider changing flame surface geometry in flames, resulting in the concept of the definition of the parameter known as stretch rate ($\boldsymbol{\alpha}$), with a relationship of temporal change in surface area expressed by **Eqn. 2.2.2**:

$$\alpha = \frac{1}{A}\frac{dA}{dt} \tag{2.2}$$

The influence of curvature on flame propagation was also studied by Markstein [41]. Diffusive effect theory was later developed by the same author subsequent to his study of curvature effects [42]. The concept of Lewis number (***Le***), which accounts for diffusive effects, was subsequently developed by Lewis [43]. This parameter expressed the ratio of thermal diffusivity to mass diffusivity of the deficient reactant and is given by **Eqn. 2.2.3**:

$$Le = \frac{\lambda}{\rho C_p D} = \frac{k}{D} \tag{2.3}$$

where λ represents thermal conductivity, ρ the density, C_p specific heat, k the thermal diffusivity and D; the mass diffusivity. Through nonunity Le interpretation it is possible to determine whether thermal diffusivity or mass diffusivity effects are dominant on flame propagation. For instance, when $Le > 1$ the flame accelerates as it expands as a consequence of the thermal diffusion being dominant, provoking heat losses of the flame in proportion to the surrounding reactant. This is owing to stretch effects being more influential when the flame is small, and in relation the curvature is large. Conversely the opposite effects are seen when $Le < 1$.

Another parameter directly related to Le – by influencing both polarity and magnitude of the influence of stretch – is the burned gas Markstein length (L_b). The relationship between Le – L_b, and calculations of some related parameters are given in **Appendix A**. The Markstein length [41, 42] is the parameter which accounts for the influence of stretch on flame speed.

Several improvements have been achieved by the different approaches introduced, so as to determine the laminar flame speed and its parameters by using the outwardly propagating spherical flames in a constant-volume vessel method, so that a clearer understanding of the subject is possible nowadays.

Bradley et al. [44] were pioneers in the development of computational studies to determine stretch-free spherical laminar flame speeds at constant pressure for methane-air mixtures. In this study two burning velocities were computed; one based on the rate of disappearance of unburned gas, and the other on the appearance of burned gas – the former also recently studied by Varea et al. [45]. The authors also investigated the nature of flame stretch rate, which is comprised by the flow field strain rate α_s and the flame curvature α_c, by representing the total stretch rate expression given by **Eqn. 2.2.4**:

$$\alpha = \alpha_s + \alpha_c \tag{2.4}$$

An important conclusion of their results was the impact of variation in ignition energy which was presented in order to ascertain its subsequent effect upon flame development, establishing the independency of flame speed from its effect for flame radii of greater than 6mm as exhibited in **Figure 2.2**.

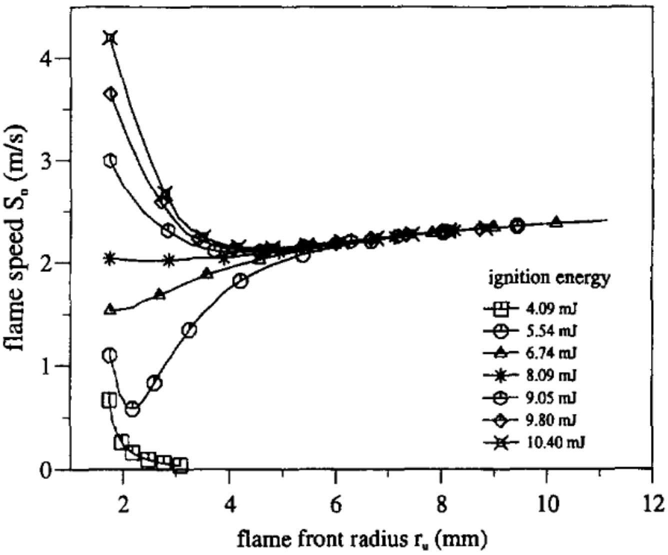

Figure 2.2 Flame speeds plotted against radius for different igniting energies [44].

Subsequently experimental results were undertaken by Gu et al. [46] and were compared with two sets of modelled predictions, the laminar burning velocity was expressed as a function of pressure, temperature, and equivalence ratio for methane-air and iso-octane-air mixtures. The authors observed instabilities/cellularity in the flame structures at high pressure, and established a correlation linking the onset of cellularity with certain values of Markstein length.

The two aforementioned investigations by Bradley and Gu along with that of Andrews and Bradley's [34, 35] works, set the foundation of further studies concerned with the method of burning rate prediction by determination of the unstretched flame speed (**S_L**) when a spherical expanding flame technique is utilised. This method developed by Dowdy et al. [47] and Taylor [48] suggests a linear relationship between **α** and flame speed given by **Eqn. 2.2.5**:

$$S_L - S_n = L_b \alpha \tag{2.5}$$

Where **S_L** is obtained as the extrapolated intercept value of the stretch flame speed (**S_n**) at **α** = 0. Furthermore, in more recent years several modifications have been proposed more accurately determine the unstretched flame speed, most noticeably the works of Tahtouh et al. [49], Kelly and Law [50], Halter et al. [51], Varea et al. [45]. In all these studies in contrast to the historically adopted linear correlation a non-linear extrapolation method is presented as an alternative way to determine **S_L**; with such an expression presented by **Eqn. 2.2.6**.

$$\left(\frac{S_n}{S_L}\right)^2 \ln\left(\frac{S_n}{S_L}\right)^2 = -\frac{2L_b\alpha}{S_L} \tag{2.6}$$

However it should be noted that other studies have also been presented, resulting in good agreement on the determination of flame speed with the aforementioned studies such as Wu and Law [52], Vagelopoulos and Egolfopoulos [53], Kurata et al. [54], and Bonhomme et al. [55].

Recently, the study of alternative fuel sources have become more prevalent, driven by environmental and economic concerns, thus parameters related to the determination of the flame speed for renewable liquid fuels such as ethanol and methanol has impacted the research community. Interest in the characterisation of liquid fuels at different initial conditions such as elevated pressure, temperature and equivalence ratio has been investigated by Bradley et al. [56] and Varea et al. [45] and is relevant to many technologies most notably that of gas turbine combustion.

2.3 Determination of Extinction Stretch rate

One combustion characteristic related to flame stability particularly of concern in gas turbine combustors experiencing issues related to fuel variability and fuel flexibility is flame extinction, which is defined as the limited fuel concentration in a reactant/oxidiser mixture in which chemical reaction is not self-sustaining [57-59]. Mechanisms such as chain-terminating reactions, radiative heat loss, and nonequidiffusion, provoke that local energy loss rate exceeds the energy release rate favouring extinction of the flame [60].

In 1982 Ishizuka and Law [57] investigated the effects of downstream heat loss on the extinction of a stretched premixed flame by proposing an experimental arrangement called the counterflow burner, used to study both lean and rich methane-air and propane-air mixtures. This pioneering work is well documented in other subsequent works concerned with the determination of laminar flame speeds and extinction stretch rates [52, 61-65]. The counterflow system consisted of a planar, twin-flame-counterflow nozzle capable of obtaining the stretch rate at which flames were extinguished ($\boldsymbol{K_{ext}}$). By testing at diminishing fuel/air equivalence ratios it was possible to extrapolate from the results in order to identify an equivalence ratio corresponding to an experimentally unattainable zero-stretch condition.

Law et al. [66] investigated the stretch rates and the associated flame speeds at the state of extinction, brought about due to excessive flame stretching for methane/air and propane/air mixtures. The tests were performed using a symmetrical counterflow flame configuration. According to their observations, in accordance with other works, the simultaneous influence of preferential diffusion and aerodynamic stretching [57, 67-69] resulted in a flame that could be extinguished by (positive) stretch alone, due to the Lewis number being greater than unity (***Le*** >1). On the other hand, when Lewis number was less than unity (***Le*** <1) flame extinction was caused not only by stretch but also by incomplete chemical reaction.

Among their conclusions, they remarked that since mixtures in which ***Le*** > 1 flame temperature was reduced by stretch; extinction could be achieved with smaller values of stretch. On the other hand, at elevated temperatures – at least before the onset of incomplete reaction – flames in which ***Le*** < 1 were more resistant to extinction, therefore, they required larger values of stretch.

Egolfopoulos et al. [70] investigated the interaction between gas phase reactive streams and solid surfaces such as the natural boundaries of a combustor, by comparing the effects of conductive heat losses to the wall with the extinction stretch rate values for the single-jet counterflow configuration. According to the authors this interaction approximated more with realistic situations in which the dependency on thermochemical properties of two phases of complex processes such as heat, mass, and momentum transfer between the solid surface and the gas could not be ignored. They remarked that this interaction was masked by the use of the opposite-jet counterflow configuration due to its adiabatic characteristics.

In their study they proposed the single jet-wall over the opposed-jet counterflow configuration as a more reliable method for the determination of not only the laminar flame speed, but most important the extinction stretch rate. This conclusion came after observing that the presence of the non-adiabatic wall affected the flow field in various ways; for instance, their results indicated that in the hydrodynamic zone due to the non-slip condition at the wall caused a significant reduction of the stretch rate values. Moreover, comparing to an adiabatic system, the conductive heat loss presented on the wall produced flame weakening and therefore a reduction in the extinction stretch rate values when the flame propagation was close to extinction. Finally, they found that the presence of heat loss is more dominant in flame extinction compared to preferential diffusion and stretch effects.

Holley et al. [8] used a single-flame counterflow configuration to determine the extinction stretch rate (K_{ext}) of ethanol, methanol, n-heptane, and iso-octane with air mixtures under atmospheric temperature and pressure. The authors also used a numerical simulation based on a Kee et al. [71] computer code to test a number of kinetic mechanisms against the experimental results.

It was expected that propagation and extinction were controlled by similar chemical kinetics, as both are high temperature phenomena in agreement with previous studies of sensitivity analysis of ethylene/air [72] and methane/air flames [70, 73]. However, the controlling chemical kinetics for the liquid fuels especially for n-heptane and iso-octane studied by the authors differed. Furthermore, it was seen that sensitivities to molecular diffusion could be of the same order as those of kinetics. A major conclusion regarding the experimental determination of extinction stretch rate was that for the same equivalence ratio, alcohols were more resistant to extinction than n-heptane and iso-octane.

Several other works have been undertaken using the single-jet counterflow configuration in conjunction with different chemical kinetic numerical models to calculate flame propagation and extinction of different fuels. A mention of those that were used for comparison in this present work are, for instance, Park et al. for methane [74] and for propane Veloo et al. [75].

In the case of spherically expanded flames Bradley and co-workers [56] made a very important observation, suggesting that by using under-driven spherical flames it was possible to provide an alternative method to evaluate extinction stretch rates. In their work they used a spherical stainless steel bomb in which they obtained measurements of ethanol-air laminar gaseous flame characteristics at high pressures. By detecting a point – represented by **#** symbol in **Figure 2.3** – in which the flame cannot be fully established due to the excessive influence of stretch rate, the authors 'tentatively' stated that the highest stretch rate just before the flame became self-established might represent the extinction stretch rate. Thus, if the value of this point were higher than flame propagation would not be possible.

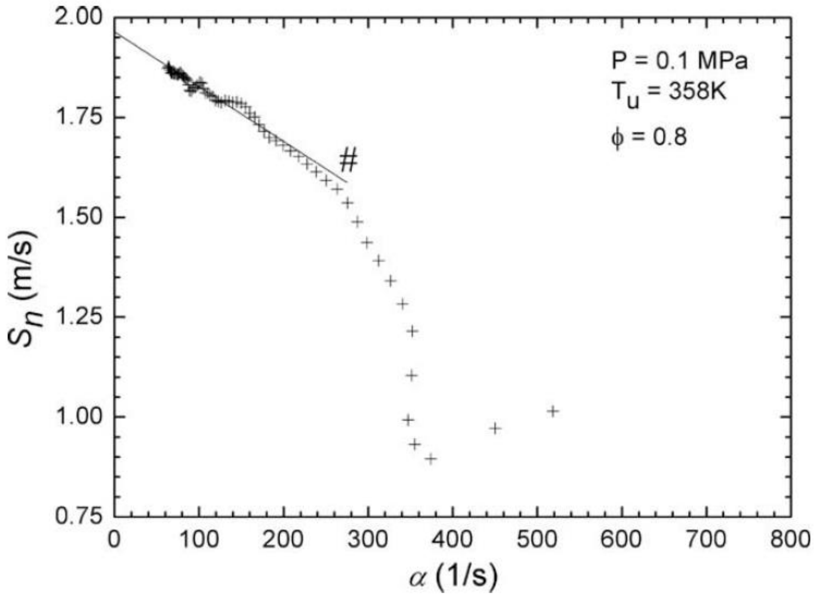

Figure 2.3 Variations of flame speed, Sn, with α, for φ = 0.8 at 358K and 0.1 MPa, at low ignition energy. Inner limit of stable flame indicated by # [56].

The researchers reported that this was the only flame that they could obtain with these under-driven characteristics. Further evidence of nonlinear effects during early stage flame propagation using a low energy ignition system was presented by Crayford et al. [76]. In their study the effects of water vapour as a suppressant of outwardly propagating spherical methane flames was investigated, utilising a constant-volume explosion vessel. Moreover, the authors noted that at rich mixtures and high water loading the flame had to be excessively overdriven in early stages of flame growth in order to avoid flame quench, hence, presenting nonlinear effects during flame propagation at these conditions as it is depicted in **Figure 2.4**.

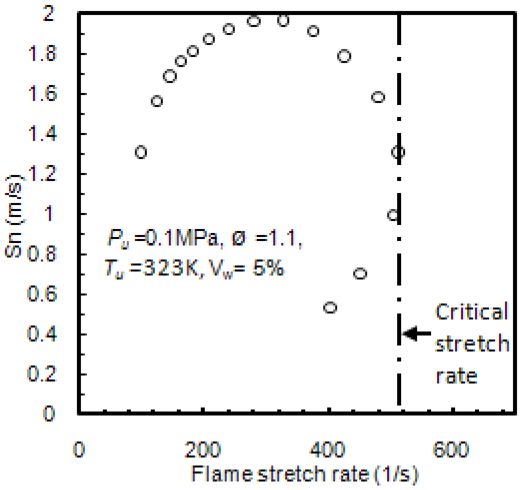

Figure 2.4 Variation of flame speed with stretch rate for 'under-driven' flame at φ = 1.1, T = 323K, water loading 5%.

According to their results, the authors proposed – supporting Bradley et al. [56] observations – a critical stretch rate beyond which the flame is unable to exist without additional energy input and i.e. the turning point highlighted above.

The effects of ignition energy and mixture ***Le*** on the flame kernel growth in a spherical flame by allowing for strongly stretched flames was investigated theoretically and experimentally by Ju and co-workers [77, 78]. They quantified the minimum ignition energy necessary to pass a critical radius in order to start flame propagation. The flame speed initially decreases as flame expansion was observed. However, after passing the aforementioned critical radius the flame branches merged and the flame speed increased with increasing flame radius and finally approached unity at large flame radii. Moreover, non-linear flame trajectory was also seen by the authors; nevertheless, no comparisons of the critical radius' stretch rate value with extinction stretch rates were reported.

Kelly and Law [50] undertook experiments using n-butane at atmospheric conditions in a constant-pressure combustion chamber for establishing a non-linear extrapolation method in order to obtained flame velocity values at zero flame stretch rate. The necessity of developing such expression emerged after the authors observed that there were cases in which the flame propagation was affected by high stretch rates and/or strong mixture non-equidiffusion – giving large values of ***Le*** – provoking that the dataset exhibited curvature. It is important to note that although lean and rich n-butane mixtures needed to be data processed using the non-linear extrapolation method, the investigators found that linear extrapolation was adequate to calculate the unstretched velocity for mixtures which were not as strongly affected by stretch such as hydrogen/air and methane/air mixtures.

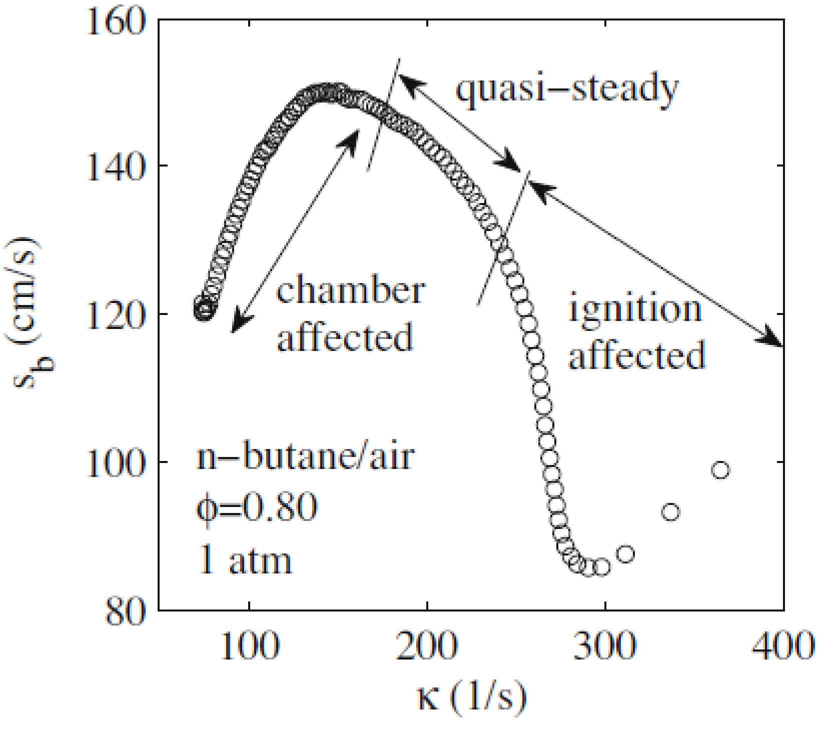

Figure 2.5 Flame speed as a function for a typical n-butane/air outwardly propagating flame experiment. The experiment is influenced by ignition and wall confinement and care must be taken to determine data that are influenced by these effects [50]. The corresponding nomenclature for *Sb* and *k* in the present study is *Sn* and *α*, respectively.

Due to this curvature in the dataset it was important to separate the flame propagation in three regions namely; the ignition affected region, quasi-steady region, suitable for the extraction of unstretched flame velocity at zero stretch and finally the chamber affected region. All three regions are depicted in **Figure 2.5**.

In their study the influence of the ignition kernel on the subsequent flame evolution highlighted that as the influence of the spark energy was dissipated all trajectories merged together in a turning point. In **Figure 2.6**, tests were performed varying two different ignition energies to present the transient period in which the flame trajectory was affected by different spark energies.

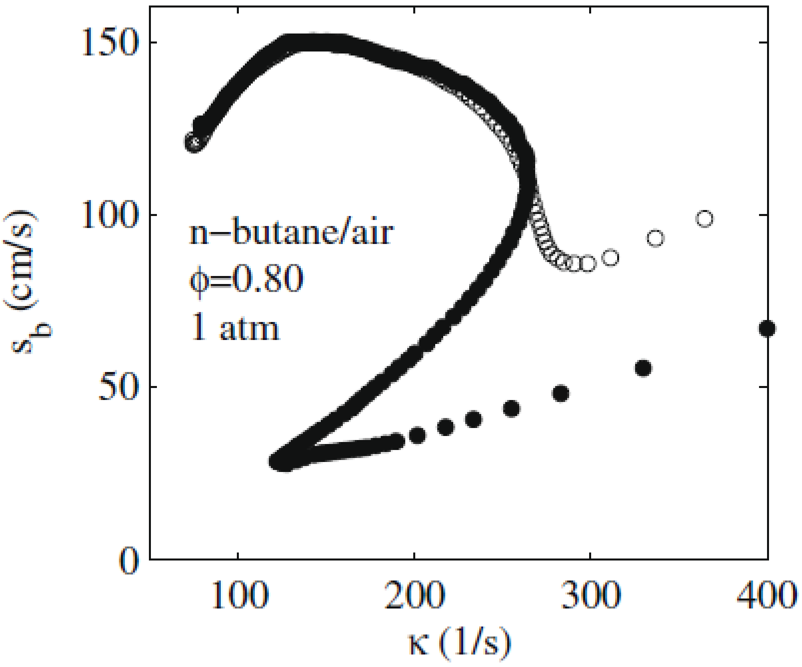

Figure 2.6 Two experiments with differing ignition energies. The region where the two experiments disagree is affected by ignition energy [50]. The corresponding nomenclature for *Sb* and *k* in the present study is *Sn* and *α*, respectively.

Eventually the two flame trajectories aligned on a common turning point when the spark energy was dissipated; therefore, the region of disagreement was discarded in order to determine the laminar burning velocity. However, the region affected by the ignition kernel and this turning point will represent the fundamental part of the investigation of the extinction stretch rate proposed using spherical flames in the present thesis full details of which will be presented in Chapters 4, 5 and 6.

The non-linear extrapolation proposed by Kelly and Law was derived following the work of Rooney and Sivashinsky [79], whose evolution equation was applied for outwardly propagating flames free of small stretch assumptions but considered density variations. In addition, Kelly and Law restricted their analysis of this equation to adiabatic and quasi-steady flame propagation.

De La Rosa et al. [80] studied non-stoichiometric mixtures, heavily influence by stretch and non-equidiffusive flames. Their experiments were undertaken on laminar ethanol-air gaseous spherical flames in a cylindrical constant volume combustion bomb at different ambient conditions, in order to benchmark not only laminar burning velocities and Markstein lengths, but also investigate the effect of minimum ignition energy on the early stages of flame front propagation as a viable method for deriving extinction stretch rates ($\boldsymbol{K_{ext}}$) from non-linear trends exhibited during early flame propagation.

The authors also conducted experiments varying spark energy to assess the influence of the ignition kernel on the subsequent flame evolution at high stretch rates (small radii) for lean ethanol/air mixtures. By the end of the ignition dominated phase, the expected turning point appeared for the lower energy cases – the proposed critical stretch rate ($\boldsymbol{\alpha_{Cr}}$), which is independent of the initial ignition energy below a critical threshold was observed. This point represented the highest stretch rate experienced during flame growth after the effect of ignition energy had dissipated. Similarities between the non-linear trajectory followed by the raw experimental data and the non-linear extrapolation method proposed by Kelly and Law [50], suggested that it might be possible to locate the aforementioned critical stretch rate ($\boldsymbol{\alpha_{Cr}}$) through this low ignition method as it is depicted in **Figure 2.7**.

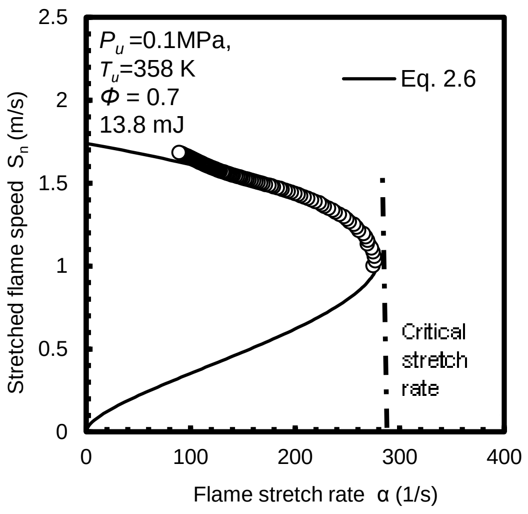

Figure 2.7 Measured Critical stretch rate at low ignition energy for φ = 0.7, 0.1 MPa and 379K.

It should be noted that in **Figure 2.7** the early stages of flame propagation could not be captured due the limitations of the bespoke MATLAB script; however, this script was modified for the present thesis in order to obtain the whole data set of the flame trajectory including the important ignition affected section. In a similar way, several modifications to the experimental methods and also tests of different fuels were undertaken to improve and validate the post-processing analysis of the data set which will be discussed further in the relevant chapters of this work.

Law [31] explained through nonunity ***Le*** interpretation, the relationship between diffusion transport and stretch rate on flame behaviour along with the consequences of this association on flame extinction mechanism in stagnation surface for counterflow burner configurations. The author stated that the flame experienced nonequidiffusion effects during its propagation due to strong flame stretch depending on whether ***Le*** was greater or less than unity; resulting in either a decrease or an increase in the temperature of the flame as it is depicted in **Figure 2.8**.

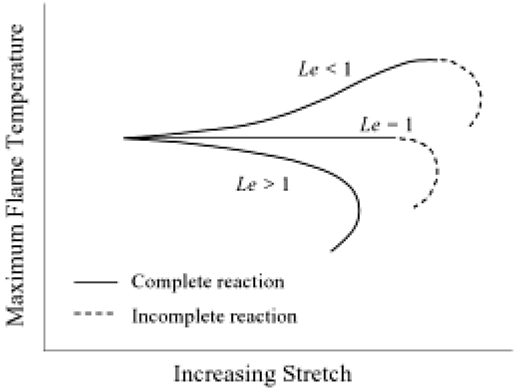

Figure 2.8 Effects of stretch, nonequidiffusion, and completeness of reaction, on the extinction turning point behaviour [31].

In the case where ***Le*** > 1 it was seen that the temperature dropped as the stretch increased; this drop reached a critical turning point in which the burning was not attainable due to the gain in the concentration of the deficient species had fallen behind the associated heat loss. For instance, the stagnation flame scheme as presented in **Figure 2.9a** shows the flame was positioned at a finite distance away from the surface provoking the extinction of the unrestrained flame. Conversely, for ***Le*** < 1 flame extinction appeared when the flame restrained movement impinged the stagnation surface and the associated stretch was high enough to initially increase the temperature, hence, the reaction rate became incomplete due to a reduction in residence time; resulting in a gradual decrease of temperature. Finally, for ***Le = 1*** extinction was observed when the flame movement made contact with the adiabatic-impermeable stagnation surface causing an increase in stretch which induced and incomplete reaction rate.

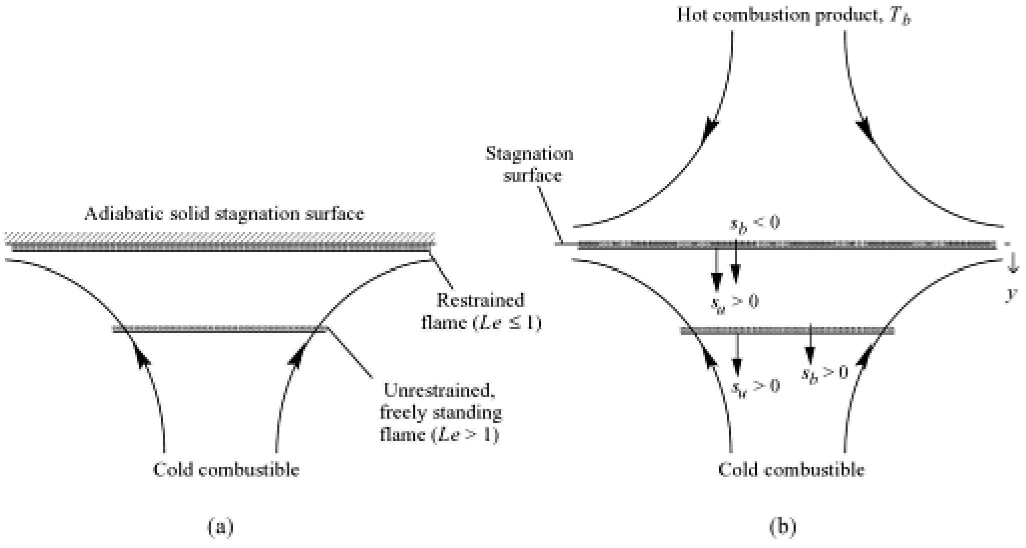

Figure 2.9 Schematic showing different extinction mechanisms and the associate flame location for (a) the stagnation flame, and (b) the counterflow flame [31]. The corresponding nomenclature for *Sb* and *Su* in the present study is *Sn* and *SL*, respectively.

On the other hand, in a counterflow configuration – **Figure 2.9b** – the combustible mixture impinged a hot product gas stream at desirable temperature, creating an adiabatic and permeable stagnation surface enough to sustain the reaction zone avoiding flame extinction due to stretch effects.

2.4 Laminar flame propagation in droplet mists

Mizutani and Nakajima [81, 82] produced one of the first investigations of the effects of what they termed ‘combustion-promoting’ on burning velocities in droplet-vapour-mixtures for an overall fuel-air ratio mixture by using a centrally spark system in a combustion chamber. The authors found that the addition of small amount of kerosene droplets resulted in a markedly increased burning velocity. Among their conclusions, they suggested the existence of an optimum value of the number/concentration of the kerosene droplets added to the propane-air mixture that promoted this effect, with the effect being more prominent for leaner mixtures.

Likewise, Hayashi et al. [83] observed burning velocity promotion for mono-sized droplets of rich ethanol-air and n-octane-air mixtures not seen in homogeneous vapour blends of the same overall fuel-air ratio. Their results came from experimental work carried out in an apparatus based on the Wilson cloud chamber [84]. The authors observed the appearance of roughened cellular flame fronts in heterogeneous mixtures suggesting that this development must be caused by instabilities in the flame front. They concluded that along with cellularity, larger droplet size of 20 µm – compared to that of 7 µm – played an important role in the enhancement of the burning rate.

Although cellularity was witnessed at near-stoichiometry for both fuel-rich and fuel-lean mixtures, only in the former burning rates were promoted, whereas for lean mixtures the burning velocity was reduced. The researchers suggested that this reduction was probably the result of the low vaporisation rate in the flame front which was not sufficiently counterbalanced by the increase in the cellular surface area, hence, resulting in lower burning rates than that of the gaseous flames.

Polymeropoulos [85] investigated the burning velocity acceleration produced by the presence of droplets in iso-octane-air and diesel oil-air mixtures, by developing a numerical model motivated by early experimental work such as that of Burgoyne and Cohen [86] in which acceleration was observed. Polymeropoulos extended Ballal and Lefebvre's [87] numerical model, which was based mainly on thermal flame propagation in a spray, along with the use of the additive criterion of heat release established by Law et al. [88, 89] regarding ignition and evaporation effects on flame propagation of droplets in heterogeneous mixtures.

The final model proposed by Polymeropoulos divided heat release into two parts, one from diffusion flames around single droplets and the second due to the reaction of the gas surrounding the droplets. His results presented the maximum enhancement in burning velocity for the diameter range of between 10 and 15 µm, as shown in **Figure 2.10**. The author highlighted three possible mechanisms that might contributed to the observed increase in velocity of the flame front: a) the presences of wrinkles on the flame front, which in turn provoked an increase in the flame surface, and hence, an increase in the propagation velocity was observed, b) droplet clouds favoured thermal expansion of the gas resulting in an enhancement in the transport process, thus in its velocity as well, and c) an optimum fuel-to-air ratio was created which surrounded isolated droplets during the burning of the fuel, resulting in an acceleration of the local reaction rate of the gaseous fraction of the mixture.

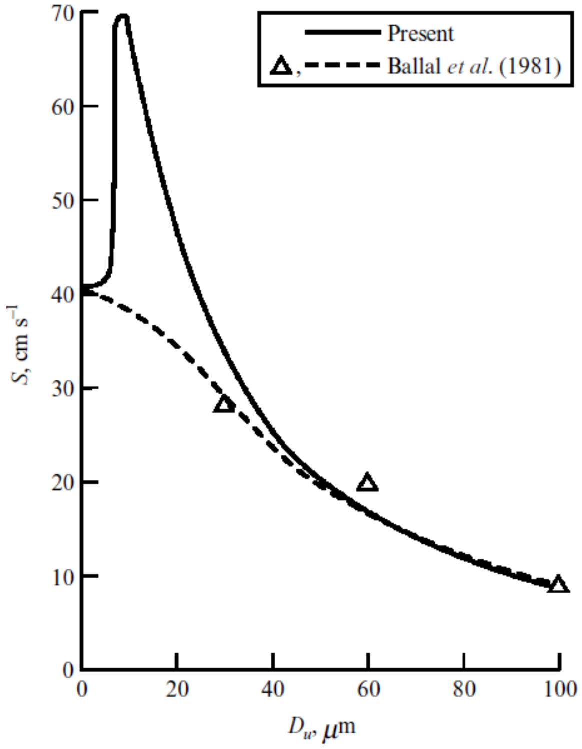

Figure 2.10 Variation of burning velocity with droplet size for medium diesel oil-air sparys at various fuel fractions [85]. The legend "Present" refers to the work of Polymeropoulos.

Among their conclusions a key part of this enhancement observed in the model for small droplets was obtained due to the thermal mechanism, sum of the heat release in the flame front coming from two different sources; one from the droplet combustion and another from the gas surrounding the droplets combustion, assuming quasi-steady vaporisation and chemical rate around the droplets.

In contrast Myers and Lefebvre [90] experimental study showed no enhancement on burning velocity of mixtures of fuel droplets in air at atmospheric conditions. They found that evaporation rates controlled the flame speed affecting the relationship between droplet diameter and flame speed in which the latter is inversely proportional to the former above a critical size. Nevertheless, it is important to note that the range selected of droplet size in which the experiments were carried out comprehended between 30 and 90 µm; relatively large diameters compared with previous works.

By presenting a single numerical model of a flame front propagating through a fuel-rich droplet-vapour-air cloud, Greenberg and co-authors [91] demonstrated similar trends of enhancement of burning rates in droplet flames under certain circumstances where the flame front became cellular while counterpart gaseous flames remained stable. Their results showed the importance of the influence of vaporisation on stability of the flame front mainly due to the heat loss mechanism from the absorption of heat by the droplets. They could establish a correlation between cellularity and the influence of the initial fuel loading and the latent heat of vaporisation giving strong proof of the important role of heat loss mechanism in the instability of the droplet flame front.

Lawes, Lee and Marquez [92] conducted an experimental investigation into the effects of two-phase laminar mixture combustion for small droplets on burning rates and comparing them to single phase iso-octane flames in a combustion bomb. According to their observations there are little differences in the burning velocity between aerosol and gaseous mixtures at the same conditions. Nevertheless, they remarked also that low stretched droplet flames became unstable and cellular at conditions where gaseous flames remained smooth and stable, resulting in some cases, in faster measured burning velocities.

Their results led them to discover that values of burned Markstein lengths (***L_b***) for aerosol flames were lower than those for gaseous flames under the same conditions, as depicted in **Figure 2.11**. This allowed them to suggest that smaller or even negative values of ***L_b*** provoked more susceptibility to the development of instabilities especially for larger aerosol sizes and rich mixtures, due to the fact that thermodiffusive effects were no longer stabilising aerosol flame propagation. The solid line in **Figure 2.11** was calculated using an empirical relationship between ***L_b***, overall equivalence ratio (***$Ø_o$***) and temperature (***T***). The authors remarked that the effect of stretch rate on gaseous combustion is stronger than in droplet flame speeds.

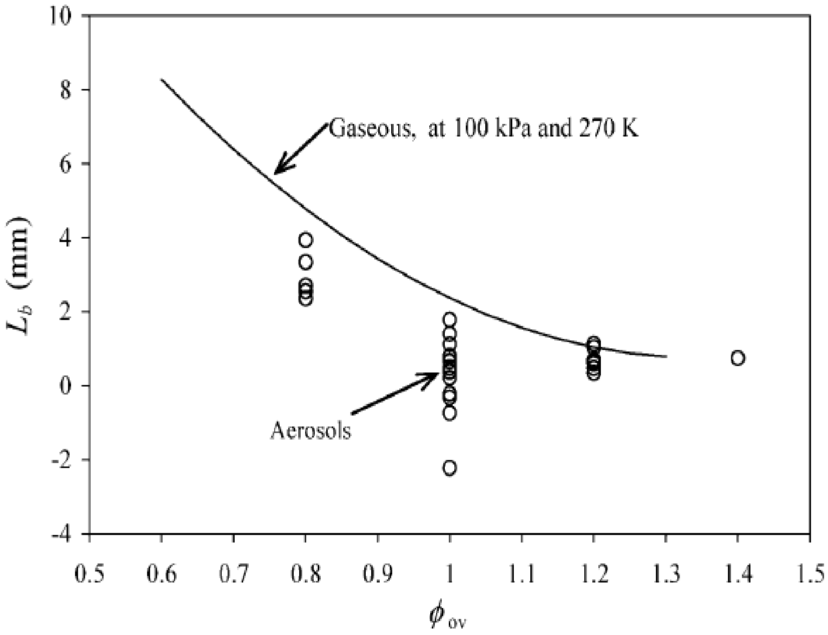

Figure 2.11 Variation of L_b with $Ø_o$ for iso-octane aerosol flames compared to iso-octane premixed flames, at a pressure of 100kPa and an average temperature of 270K [92]. The corresponding nomenclature for *Øov* in the present study is *Øo*.

Among their conclusions, they noted that there was an indication that aerosol flames became unstable more quickly as the Sauter mean diameter (***SMD***) was increased, this was reflected in a corresponding reduction of the critical Peclet (***Pe_{cr}***) number with ***SMD***. The ***Pe_{cr}*** hence described the point where the flame started to accelerate due to the appearance of cellularity and instabilities. Moreover, they stated that during the later stages of flame propagation, where cellularity became noticeable, the effect of strain was dominant over that of curvature. Finally, in their study they proposed that aerosol flames became cellular at smaller radii than did gaseous flames suggesting an enhancement in the burning rate of aerosol flames compared to gaseous flames.

Although a general trend of increasing ***SMD*** lead to a corresponding decrease in L_b, the authors did not outline the existence of an optimum droplet size with which it had yielded an enhancement in the burning velocity.

In 2007 Nomura and co-workers [93] investigated the effects of high pressure on flame propagation in monodispersed droplet clouds using heterogeneous ethanol mixtures in a combustion chamber. According to their work normalised flame speeds in droplet mixtures were faster than those of their counterpart gaseous flames where fine fuel droplets in the fuel-leaner side – between total equivalence ratio of 0.6 and 0.8 – were observed at all tested pressures. The conditions at which this enhancement was found comprised relatively small values of liquid fuel equivalence ratio ($Ø_l$). Conversely, the suppressive effects on flame speed in the heterogeneous mixture were witnessed between $Ø_o = 1.0$ and 1.2.

Furthermore, the researchers reported a similar enhancement in the fuel-leaner side of the mixture of droplet flame speed compared to a comparable gaseous flame, with the relationship between flame speed and the total equivalence ratio at all pressures presented in **Figure 2.12**. The authors attributed this enhancement to the effectiveness of the fuel droplets in increasing the gas equivalence ratio in the reaction zone compared to the same amount of fuel vapour.

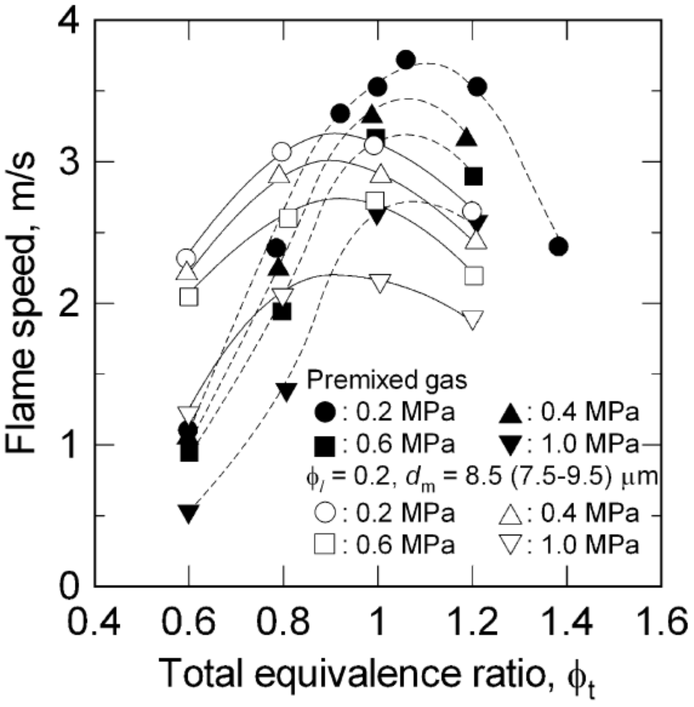

Figure 2.12 Effect of pressure on the relation between the flame speed and the total equivalence ratio [93]. The corresponding nomenclature for *Øt* in the present study is *Øo*. Flame speed on the y-axis in the present work is expressed as *SL*.

In their study the authors outlined that the maximum flame speed of gaseous flames was greater than that of the droplet flames because of a temperature drop provoked by evaporation during flame propagation. After extensive tests Nomura and co-workers concluded that the enhancement in droplet evaporation in the preheat zone was significantly influenced by increased pressure. They remarked the importance of the influence of selected mean droplet diameter and liquid equivalence ratio values –8.5µm and 0.2, respectively– on the resulted enhancement of the flame speed at fuel-leaner mixtures.

Neophytou and Mastorakos [94] investigated the effects of initial droplet diameter, overall equivalence ratio ($\boldsymbol{Ø_o}$) and droplet residence time before reaching the flame front on flame propagation. By using a one-dimensional code with detailed chemistry and transport, they carried out studies of n-Heptane and n-Decane under atmospheric and relight and low temperature and low pressure conditions.

The authors exposed that although the propagation of a gaseous flame at $\boldsymbol{\O_o}$ = 4 was not possible, in case of a droplet flame it was. In addition, by varying the degree of pre-evaporation it was observed that the laminar flame speed ($\boldsymbol{S_L}$) in droplet mists was higher than the comparable gaseous laminar flame speed for a droplet diameter between 50 and 90 µm as shown in **Figure 2.13**. In addition, the researchers presumed that smaller droplets presented similar $\boldsymbol{S_L}$ to gaseous flames which resulted in lower flame speeds; therefore, they suggested the existence of an optimum droplet size with which the flame reached its maximum value.

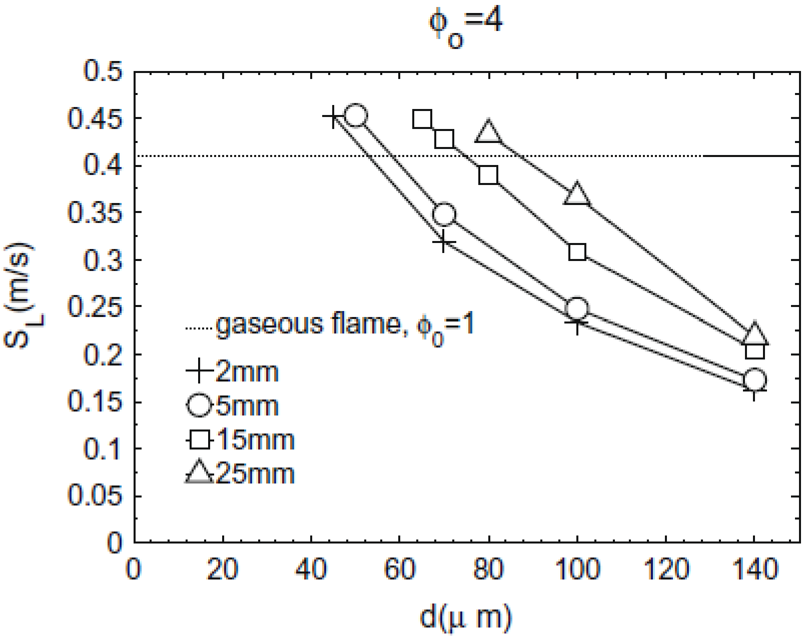

Figure 2.13 n-Heptane flame speed as a function of the initial droplet diameter for different lengths before reaching the preheat zone at Øo = 4 [94].

The authors concluded that there were three scenarios in which the structure of a spray affected the flame front. The first one; the rate of evaporation of small droplets was so high resulting in identical flame speeds as the gaseous flames. In the second scenario little evaporation was witnessed. Less oxidiser reacted in the homogeneous reaction zone; therefore, the rest of the oxidizer was consumed in a long droplet burning zone. And finally the third scenario in which the droplets were large enough to provide enough gaseous fuel to react with all of the oxidizer, hence, the surviving droplets were pyrolysed producing reactive species such as Hydrogen (H_2), acetylene (C_2H_2) and ethylene (C_2H_4). These species diffused back towards the oxidation zone enhancing the reaction rates thus enhancing the flame speed.

Bradley and co-workers [95] performed experimental tests in a cylindrical explosion bomb by using the cloud chamber technique in order to study premixed laminar aerosol spherically i-octane, ethanol and hydrous ethanol with air flames at atmospheric conditions. By measuring gaseous and droplet flame propagation characteristics such as droplet size, droplet number density and flame speed, the authors obtained a methodology for deriving mass burning velocities and entrainment velocities, as well as mass burning fluxes. In their investigation of burning velocities they varied different values of droplet diameter (d_o) and equivalence ratios of liquid phase ($Ø_l$) with minimal stretch effect by selecting the flame speed at a flame radius of 48 mm (S_{n48}) as shown in **Figure 2.14**. The overall equivalence ratio is that of gaseous phase ($Ø_g$) plus that of liquid phase ($Ø_l$); therefore, $Ø_l$ is given by **Eqn 2.7**.

$$\phi_l = \phi_o - \phi_g \tag{2.7}$$

It is important to note that in the case of ethanol/air mixtures (**Figure 2.14a**) the greatest enhancement of flame speed was observed in the lean region, $Ø$ = 0.8, for relatively large d_o and large $Ø_l$, whereas in the case of i-octane-air mixture (**Figure 2.14b**) the greatest enhanced flame speed value was witness at the rich region, especially for $Ø$ = 2.0 at relatively large d_o and large $Ø_l$. Although **Figure 2.14** correlated only at S_{n48} and the overall equivalence ratio, the same tendencies were observed in correlations involving mass burning velocity and entrainment velocities against $Ø$. The authors stated that as $Ø_l$ increases with droplet diameter, so does the flame instability and S_n; therefore, the studies of burning velocities were made for flame radius of 48 mm in which the flame suffers minimal stretch rates effects.

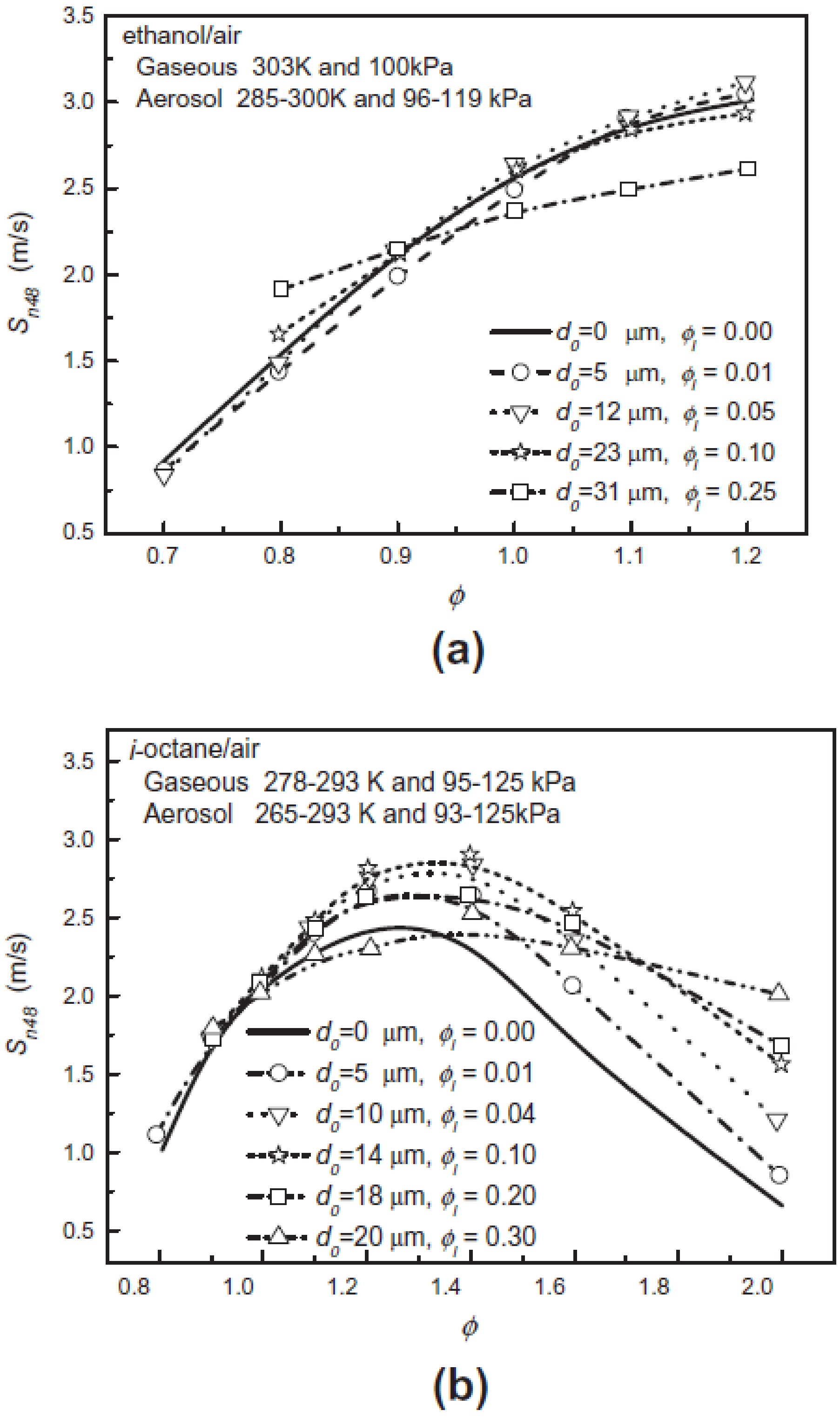

Figure 2.14 . Flame propagation speeds of (a) ethanol/air and (b) i-octane/air flames at a radius of 48 mm, flames with various droplet sizes and liquid equivalence ratios [95].

The authors remarked that there was a development in cellularity as ***Ø*** increases for iso-octane flames above ***Ø*** = 1.2. This phenomenon led the investigators to find that the onset of $\boldsymbol{Pe_{cr}}$ decreased with the presence of the droplets compared to gaseous mixtures, resulting in greater mass burning and entrainment fluxes than those observed for gaseous flames. Furthermore, the authors also reported the presence of oscillatory regime previously studied by Atzler et al. [96]. This regime caused a droplet ethanol flame at lean **Ø** and d_o above 12µm was accelerated – conditions in which gaseous flames showed lower values – due to the creation of a region ahead of the flame in which the $Ø_l$ increased as a result of a deceleration of the droplet flame provoked by drag on the droplets to below that of the gaseous flame. However, when the droplet flame crossed this enriched mixture region cellularity was observed producing an increase in flame speed and gas velocity just ahead of the flame. Finally when the flame passed the aforementioned enriched mixture region, the cellularity disappeared and the values of these parameters fell creating an increase in $Ø_l$ which again induced change. It was observed that the cycle was repeated throughout the entire flame propagation.

The observation made by Bradley et al. [95] showed that the presence of the droplets enhanced the onset of cellular instabilities such as Darrieus-Landau thermo-diffusivity and the associated wrinkled flame surface, and therefore the corresponding flame speed values – especially for iso-octane rich mixtures where less than 90% of droplets were evaporated in the preheat zone – this led the authors to use the explanation of the onset of instabilities in rich droplet flames given by Greenberg et al. [97] which stated that cellular structures, not seen in gaseous flames, were generated by the presence of vaporising droplets inside the reaction zone. This presence favoured the increase in the surface area resulting in an increase in the burning rate. However, according to Bradley et al. [95] turbulence can override aerosol instabilities as exhibited the work of Lawes and Saat [98] and that of laminar instabilities in purely gaseous flames observed by Bradley et al. [99].

2.5 Summary

All previous extinction stretch rate research studies have determined K_{ext} using the well-established counter-flow technique, leaving the study of alternative methodologies of its determination relatively unexplored. Thus the author suggests such an approach using outwardly propagating spherical flames within a constant volume combustion chamber is explored.

A broad range of studies –both numerical and experimental– have reported an enhancement in the droplet flame speed comparing to gaseous flame at the same conditions; however, other studies offer conflicting views with no observed enhancement and at times a negative effect on flame speed. Therefore, it is necessary not only to ensure that experimental performance to be accurate and repeatable with respect to other works, but also to present new correlations that help to understand the nature of laminar flame speed thorough droplet mists.

Chapter 3

"I think that in the discussion of natural problems we ought to begin not with the Scriptures, but with experiments, and demonstrations."

Galileo Galilei

Experimental Methods and Procedures

3.1 Introduction

To realise the objectives set out in Chapter 1 it was necessary to conduct numerous experimental test campaigns, so as each of the discrete variables could be accurately controlled facilitating the generation of accurate data and thus the determination of meaningful conclusions. This chapter describes the test facilities, methods and procedures deployed during the experimental programmes -discussed in detail later in Chapters 5 - 7. The cylindrical constant volume chamber setup used to conduct laminar burning characterisation of single phase gaseous fuels, as discussed in Chapters 5 and 6 is outlined in section 3.2 with detail of the schlieren setup and ignition system given in sections 3.3 and 3.4, respectively. The data acquisition and processing methods required for flame propagation measurement are presented in section 3.5. Subsequently an overview of the experimental procedure used to obtain these parameters is given in section 3.6.

Section 3.7 describes the dynamic cylindrical constant volume chamber set up used to facilitate mist formation, with details of the laser diffraction technique used for droplet sizing also given. This experimental setup allowed the investigation of two phase aerosol combustion the results of which are discussed in detail in Chapter 7.

3.2 Cylindrical Constant Volume Chamber setup

The cylindrical constant volume chamber (CCVC) used for laminar flame speed characterisation was manufactured from stainless steel (type 316) by the School of Engineering at Cardiff University. This combustion chamber is cylindrical in nature and is enclosed at both ends. Having an internal diameter of 0.26m and 0.72m height the chamber provides and internal volume of 34.8 litres. Optical access is afforded via two pairs of diametrically opposed circular 10 cm quartz windows affording ample flame visualisation. The system was designed with a safety factor of seven to withstand an internal maximum pressure of 1.4MPa. A schematic representation of the CCVC is given below in **Figure 3.1** with a photograph of the commissioned rig given in **Figure 3.2**

As can be seen in **Figure 3.1**, the experimental setup of the CVCC requires numerous components namely; a light source (LS), two concave mirrors (CM1 and CM2), knife-edge aperture (KEA), a high speed camera (HSC) to facilitate high-speed schlieren photography (discussed later). A vacuum pump (VP), a vacuum gauge display (VGD), compressed gas cylinders (CAC) containing compressed air, and if under test gaseous fuel (GFC)- and a mass flow controller (MFC) or liquid fuel syringe and septa seal to allow accurate fuel/air ratio control. A temperature control unit (TCU) and pressure transducer to allow pre-combustion ambient conditions to be controlled and finally a data acquisition system (DAS) was used to record ‘real time’ all of the required data. It is important to note that in Chapter 5 the equivalence ratio was assured using a partial pressure method given the ideal gas properties of both ethanol vapour and air. However, in Chapters 6 and 7 it was decided that MFC be adopted offering a more precise control of the $\boldsymbol{AFR}$ for the numerous fuels tested, both gaseous and liquid fuel.

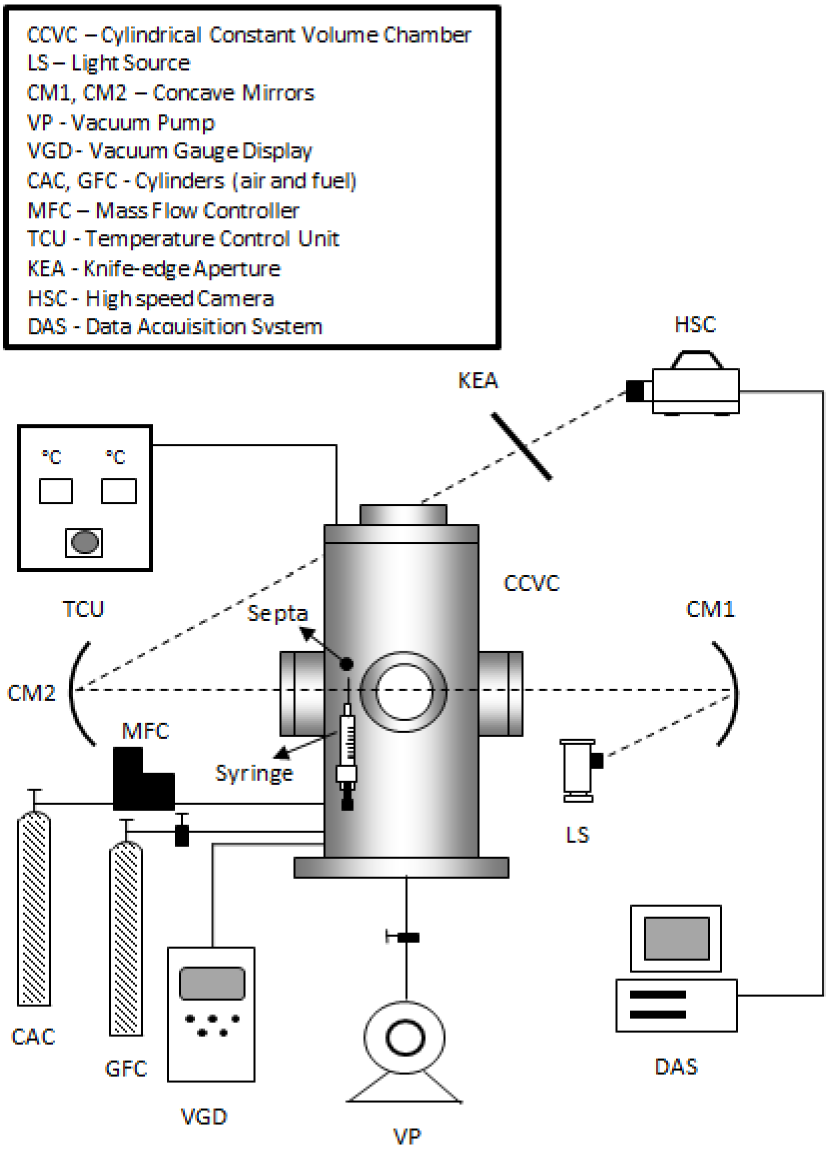

Figure 3.1 Schematic setup of cylindrical constant volume combustion chamber.

The Vacuum Pump employed was a 0.54 hp device, manufactured by Oerlikon Leubold (model SCROLLVAC SC 15D). It was used to evacuate the content of the CCVC between each test at a nominal pumping speed of $15m^3/h$, and ensured all exhaust products of previous experiments were removed. The VGD was produced by BOC EDWARDS (model D39700000) and provided accurate measurement of pressure from 1 to 2000 mbar (A). These two devices were used to ensure accurate mixing of the combustible gas prior to experimentation. All oxidant and fuel gases used for this study were supplied by BOC Industrial Gases UK.

The large design of the CVCC minimised the influence of boundary walls, hence extending the quasi steady pressure region over which unaffected data was obtained. Adjacent internal fans located on the cylinder ends ensured that the metered reactants were well mixed, prior to combustion. Each fan was powered by a Portescap D.C. motor (model 35NT2R82-50) with the 5mm diameter drive shaft sealed using viton ‘O’ ring seals. A bespoke TCU controlling 8 external bands-heaters (Watlow) – 4 of which were attached to the vessel, with the remaining 4 attached around the window mounts –, coupled with suitably rated sealing materials afforded an initial pre-combustion ambient temperature range of 298K – 423K. Four sealed ports were used to house ‘K’ type thermocouples (NiCr-Ni) which ensured uniformity of temperature throughout the internal mixture with a further two ports occupied by the ignition electrodes (discussed later), and the final remaining ports allowing access for pressure transducers.

3.3 Schlieren Setup

Due to the high speed, low light event exhibited by a spherically expanding flame, it was necessary to adopt a Schlieren technique as has been done by numerous other authors (e.g. [44, 50, 78]). Schlieren techniques depend on a change in the refractive index that accompanies density changes across the field to be investigated [100].

The schlieren setup used in this study is photographed in **Figure 3.3**. This picture shows all the devices necessary for the implementation of this technique; namely a 50W straight projector bulb used as the light source, two 0.1m diameter concave, silver, surface mirrors (CM1 and CM2), - produced by Optical Works Ltd-, a knife-edge aperture (KEA) manufactured by Thomas Mercer Ltd, (model 117/C), a Photon FASTCAM APX-RS high speed camera, (HSC), which offers up to a mega-pixel resolution along with filming speeds of up to 250,000 fps, and finally the data acquisition system, DAS, which is presented in detail in section 3.5.

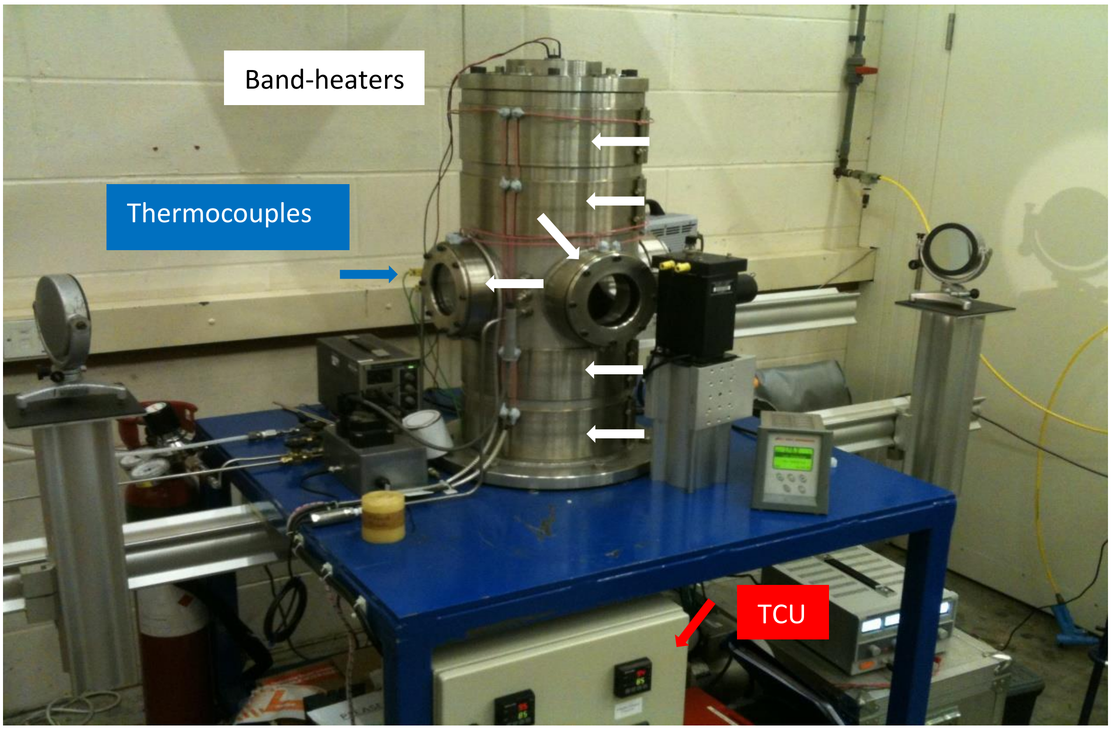

Figure 3.2 Photograph of the CCVC with 8 band-heaters, 4 thermocouples and the TCU. (The rest of the devises are in the back front of the picture).

The schlieren apparatus is sketched in **Figure 3.4**. As can be seen the LS is focused onto concave mirror CM1 providing a collimated parallel light beam which illuminates the CCVC test section. This collimated beam is then refocused using a nominally identical second concave mirror CM2 onto the knife edge aperture. The refracted portion of the beam –created due to changes in gas density – unblocked by the edge focuses imperfectly, thereby creating light intensity gradients. The recorded refracted light can thus be used to identify the isotherm representative of the flame front boundary, which was visually recorded using the aforementioned HSC. One disadvantage of this visualisation technique is that it gives 2D projection of the 3D flame provoking overlapping image effects [101]. Still images were then exported to a DAS to be processed.

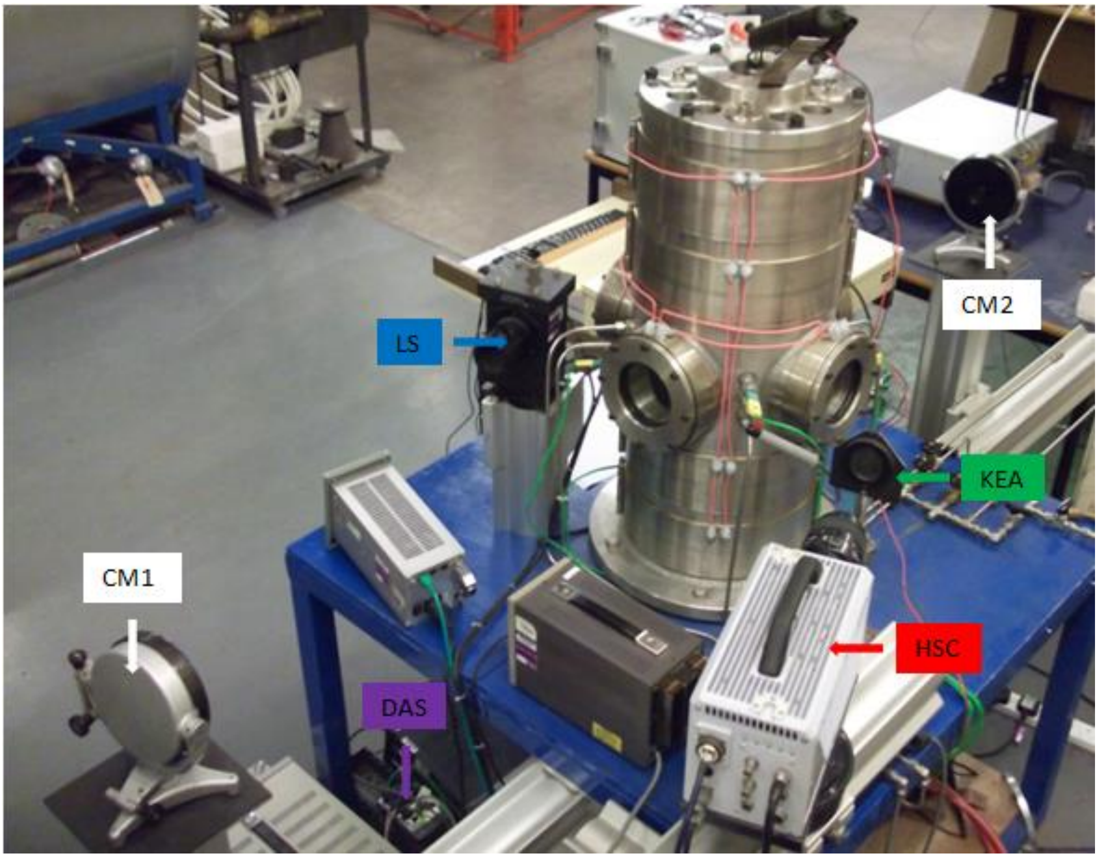

Figure 3.3 Photograph of Schlieren system employed with the Constant Volume Combustion Chamber.

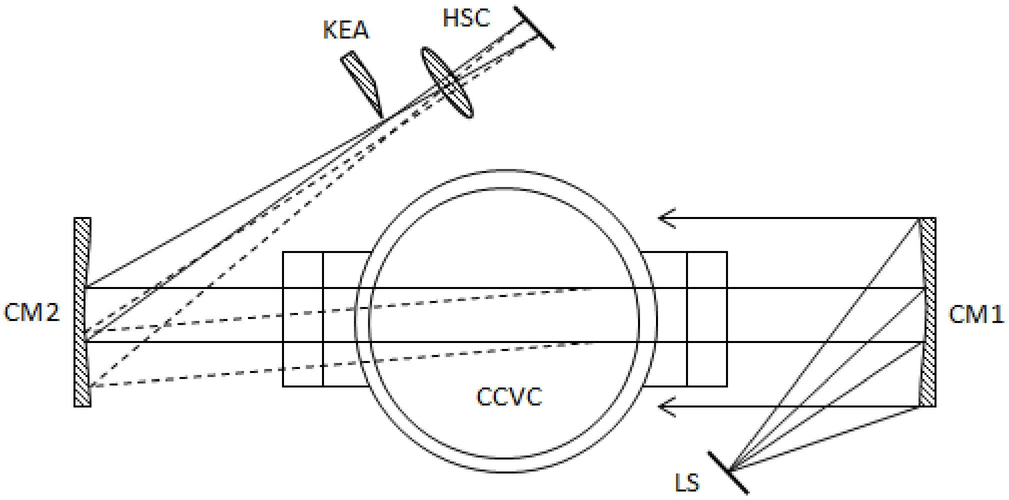

Figure 3.4 Sketch showing the arrangement of typical schlieren apparatus (Undisturbed rays shown full, disturbed rays shown dashed).

3.4 Ignition System

A variable energy capacitive-discharge ignition system was utilised to ignite the reactant mixture. This system was similar to that used by Cameron [15], Crayford [102] and Pugh [103], and a schematic representation is presented in **Figure 3.5**. The circuit consisted of three 0.47μf rapid-discharge capacitors positioned in series that were charged by a variable voltage power supply (0-350V). Using the energy (***e***) equation given by **Eqn. 3.1** and defined in terms of capacitance (***c***) and voltage (***V***), a theoretical discharge of 0-85mJ was provided.

$$e = \frac{1}{2} cV^2 \tag{3.1}$$

The rapid discharge of the stored energy to the primary coil was initiated by a 5V TTL wave to a controlling thyristor. The automobile ignition coil then acted in a similar manner to that of a standard transformer, boosting the energy on the secondary side (100:1), thus providing a theoretical peak voltage of between 0-35,000V.

The electrodes were based on a configuration used by Dreizler et al. [104], and are constructed from 2mm diameter stainless steel wires, ground to a point. The fine electrodes where offset 45° from that of the measurement plane, to minimise their influence on measured flame propagation. The ground tip provided a more repeatable spark gap (2.7mm) and thus a spark was attained. A schematic representation of the ignition system is shown in **Figure 3.5**.

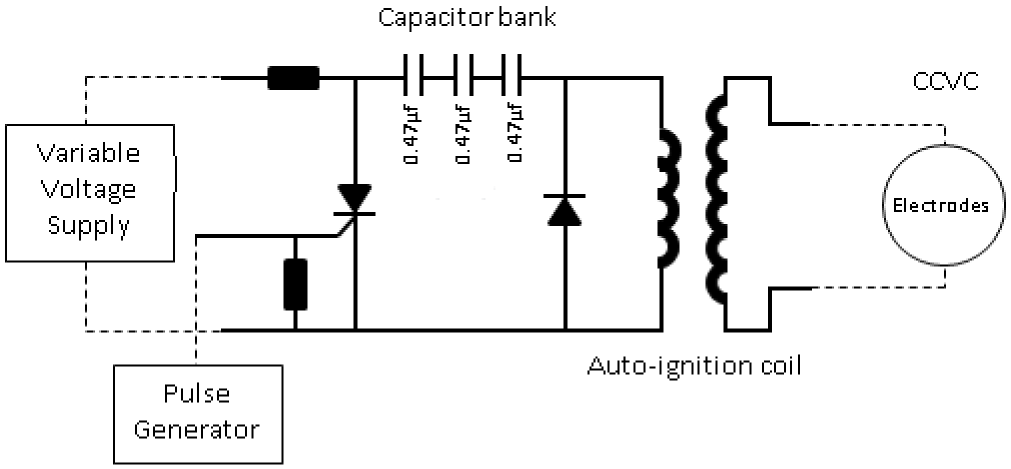

Figure 3.5 Schematic representation of ignition system.

3.5 Data acquisition and processing systems

Data sets obtained in this research during flame propagation were twofold: temperature and pressure of the fuel-air mixture were measured using a National Instruments Data Logging system, and still images were captured and then exported to a bespoke data processing software script utilising Matlab® which outputs flame front position data for prescribed time steps.

3.5.1 Characteristics of the Data Logging system

3.5.2 Monitoring of temperature

As discussed previously the temperature control of this study was conducted using a hardware PID control system. The system was capable of heating the bulk temperature up to 400K using eight external band-heaters and two k-type thermocouples (see **Figure 3.2**) by employing two individual circuits; one for controlling the temperature of the four larger heater bands that were attached to the vessel, and another for the four smaller ones attached around to the viewing windows. The set points were manually adjusted using a WATLOW® EC12RG controller working simultaneously with a WATLOW® HTLV-1LV limit monitor used as a safety circuit to respond to over-temperature conditions. The resolution of the readings obtained was ±1K, and after carrying out temperature calibration tests it was determined that this primary monitoring system was not sufficiently accurate, for data proofing, hence, another measurement system was necessary.

The secondary monitor system provided more accurate data of temperature for logging, comprised two thermocouples connected to a National Instrument (NI) 9213 16-channel thermocouple module. These high precision thermocouples were calibrated with a Hart Scientific 9100 HDRC Dry Block Calibrator. A program was written in NI LabVIEW which allowed accurate live software screen values of temperature, to be provided to the test operator allowing primary system adjustments to be made, if required prior to ignition.

In order to prove data quality, a temperature distribution measurement campaign was conducted concluding that the existence of high gradients of temperature within the test volume were negligible (±2K) and thus could be disregarded as a major source of uncertainty within the test parameters.

3.5.2.1 Data Logging system

To coordinate the data acquisition task a NI cRIO-9012 was employed as a data logging system providing multiple input series modules. Two of these modules were used for measuring temperature and pressure in real-time by utilizing the aforementioned NI LabVIEW program due to it was able to run without having to compile on the cRIO – *scan-interface* architecture. A NI 9213 16-channel thermocouple module was connected to the two k-type thermocouples in order to process the temperature data.

The NI 9205 32 channel, ±10V, input block was used not only for the capture of pressure data through a high frequency pressure transducer – 0-12bar (GE Unik-5000) 0-10V voltage output unit, but also for receiving the output from the 5V TTL pulse generator used to trigger an ignition test. The programing methodology utilized for capturing pressure measurement in real-time was the Field-Programmable Gate Array (FPGA), which facilitated the reduction in time by modifying the capture rates in order to avoid the need for compiling before operation. A DRUCK DPI 610 ±0.04% full scale accuracy unit was used to calibrate the transducer.

3.5.3 Capture and processing of the flame front data

After ignition was initiated by the aforementioned ignition system, the flame front propagation was filmed by the high speed camera (HSC) discussed in the Schlieren setup, video images were exported as movies (*.avi format) – and subsequently compiled into a series of still images (*.tiff format) in order to obtain each frame of the temporal rate of flame growth – this data handling was conducted using Photron FASTCAM Viewer (PFV), version 338 data acquisition software.

3.5.3.1 Data processing

The *.tiff files were subsequently processed by a bespoke Matlab®, version R2010a script. Data points recorded at a flame diameter greater than 10cm – corresponding to the size of the viewing windows – were removed from the final file to be processed, in order to speed the processing time whilst reducing the stored data size. Using the processing commands of the script, the final file was submitted to an edge detection algorithm first developed by Pugh [105] and subsequently modified for this work in order to capture the early stages of flame propagation where ignition effects were observed, crucial for this study. After obtaining the diameter of the spherical flame front at each time step the data were exported allowing calculation of the flame front velocity necessary for the data analysis required for the present work. A selected example of the script is given in **Appendix B**.

3.5.3.2 Image processing using the Matlab® script

To facilitate all of the testing conducted in this body of work it was necessary that the flame imaging script was adjusted for depending on the particular circumstances; for instance, to obtain small diameters during the early stages of flame propagation in Chapter 6.

A general description of the algorithm's sequential image process is given below.

- First, the script imported the relevant files from a directory into the Matlab® workspace specifying the folder containing the final *.tiff images, and then assigning a file name.

- Images from the final location were then examined with a series of viewing commands in order to set the boundaries of the spherical flame from which the measurement of flame growth was derived. With the use of the '*edge*' function the grayscale image was taken as an input and then was returned as a black and white binary image to facilitate an edge-finding task. For this task the '*canny*' algorithm was utilised to find the maxima of the magnitude and direction (angle) gradient of the input image, by adjusting the threshold value to a scalar; the edges of the spherical flame circumference could be defined as shown in **Figure 3.6**. With the use of the '*canny*' algorithm the pixels are numerically compared. If the difference in pixel intensity exceeded a specified threshold value, an edge was assigned to that point. This threshold was typically in the range of 0.08 to 0.15 depending on the image brightness and early strength of the flame front.

Edges were assigned in the numerical array as one, with all other pixel set to zero, converting the collection into a binary image.

- A '*for*' loop was used to create a variable that stored the entire image sequence. This variable was used to obtain the sequential measurement of flame diameter during its growth. Within the loop the '*imcrop*' function was utilised to crop a vertical rectangle located at a normal to the centre of the electrodes running from the top to the bottom of the viewing window. The vertical position of this cropped rectangle was changed to a horizontal position dependant on the quality of the binary image achieved. To measure the flame diameter the function '*find*' was employed which located all nonzero elements, corresponding to pixels at the circumference edge, returning the '*first*' and the '*last*' indices. An '*if else*' statement was used to evaluate the '*empty*' condition in the array.

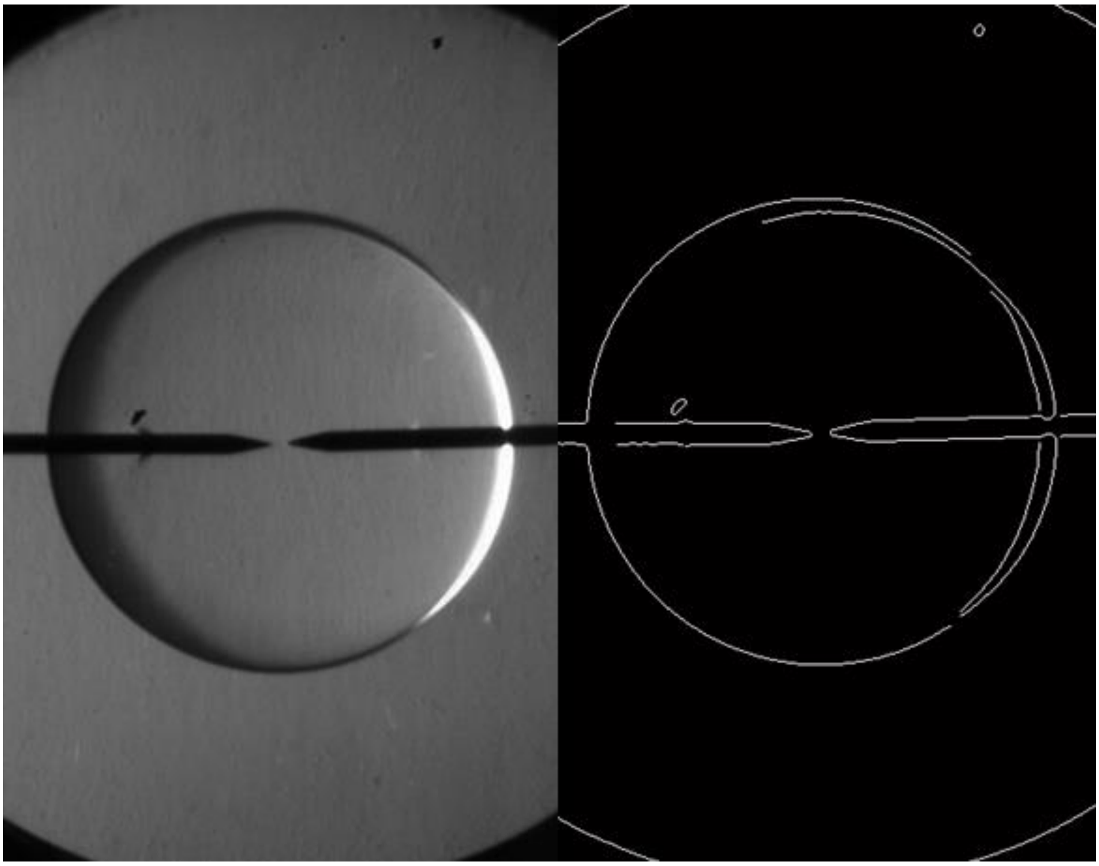

Figure 3.6 Grayscale image (left hand side) turned into a black and white binary image.

- Finally, the resulting row vectors for each image were transposed and exported to a spreadsheet database for further flame position analysis.

It is important to note that in order to obtain accurate diameter measurements, a datum scale factor had to first be measured to allow pixel locations to be equated to a scalar distance. This was achieved by filming a set of digital Vernier callipers with the aforementioned Schlieren setup at typical settings of 5, 10 and 20 mm in both the vertical and horizontal planes. Pixel projection resolutions typically in the order of 0.14mm per pixel were derived. This procedure was conducted prior to experimentation, and subsequent to any changes in experimental set.

3.6 Experimental procedure

Outwardly-propagating spherical flame methodology was applied in this study, providing information required for the determination of parameters such as flame speed (S_n) and corresponding laminar burning velocity (u_L) and Markstein Lengths (L_b) necessary for the objectives of the present work. As such a brief introduction of spherical flame theory is presented along with details concerning reactant preparation in the combustion vessel prior to ignition. Experimental procedures devised to ensure, repeatable accurate data are also presented.

3.6.1 Determination of the laminar burning velocity

A premixed flame can be defined as a thin reaction zone of great complexity, embedded in a flow system [106]. These complexities have been previously studied by numerous authors as discussed earlier in Chapter 2. However, a more thorough appreciation of heat transfer mechanisms, chemical reactions rates, chain reactions, molecular diffusion and transport properties of the mixtures, is required to better understand the controlling factors of premixed laminar flame propagation.

Currently, numerical computation of the structure of premixed laminar flames is possible for most basic fuels using complete chemical kinetics along with thermodynamic and molecular transport properties. These numerical models include both temperature and species concentration profiles. To validate these simulations, many experimental methods namely; planar, stationary, and adiabatic flame have been developed in an effort to determine u_L. with assumptions required for its determination representing major difficulties [31]. However, numerous authors (e.g. [17, 31, 107]) have proposed that outwardly-propagating spherical flame methods represent one of the most suitable options for burning rate determination.

3.6.1.1 Outwardly-propagating spherical flame method.

In this work, the CCVC was filled with a combustible mixture and subsequently ignited by a centrally located spark, in order to determine the laminar flame speed a method that has been adopted by numerous studies (e.g.[45, 50, 55, 78, 108]). The increase in temperature of product compared to the unburned reactants in the chamber causes a uniform increase in pressure whilst compression of the unburned gas upstream of the propagating flame front causes simultaneous heating. A schematic representation of spherical flame propagation is shown in **Figure 3.7**.

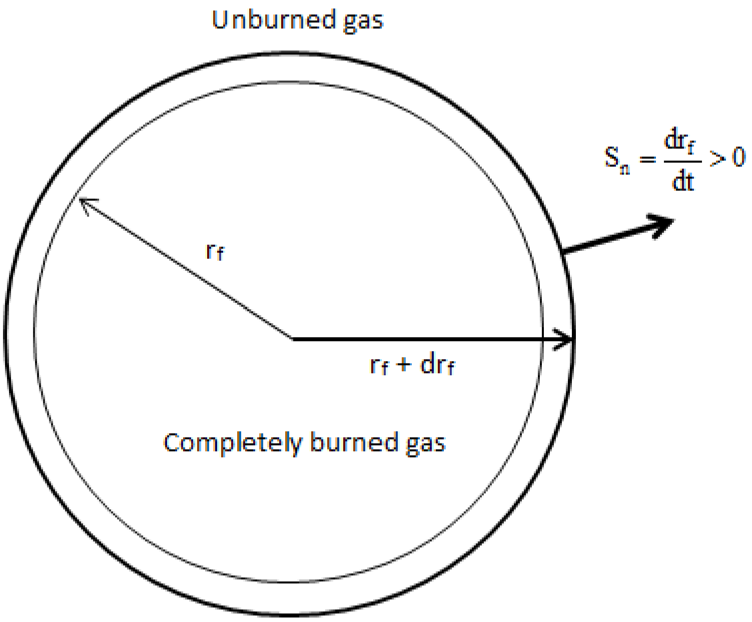

Figure 3.7 Schematic representation of outwardly-propagating spherical flame.

The measured rate of increase in flame front radius (***r_f***), for a given time period (***dr_f/dt***), may be identified as the instantaneous flame speed (***S_n***), which is influenced by flame stretch (***α***).

The present technique is a well-documented methodology for the determination of flame front position, and as such has been used by several authors [15, 17, 50, 56, 76, 106, 108, 109] to optically measure the propagation of spherical flames. The stretched flame speed (**S_n**) in this work is thus a differential measurement of Schlieren flame front radius (**r_{sch}**) and time (**t**), as given in **Eqn. 3.2**:

$$S_n = \frac{dr_{sch}}{dt} \tag{3.2}$$

In this study the instantaneous stretched flame speed was derived from the differential of a 'fitted' polynomial applied to the distance-time distribution data. This technique has been utilised in previous studies [44, 108], with its accuracy discussed by Pink [110], whom concluded that it lead to a reduction in uncertainty associated with variability due to camera resolution.

Bradley et al. [108] demonstrated through numerical studies that by applying the differential of the measured flame radius versus time, the difference between using the cold front radius – the isotherm that is 5 K above the temperature of the reactants – and **r_{sch}** is of little consequence.

Recent modifications have been proposed to improve the measurement of laminar flame speed compared with classical methods. One such improvement is an expression which depends on both pressure and flame radius [55], with a second based on the rate of disappearance of cold unburned gas, in addition to extracting values of unburned Markstein length (**L_b**) [45]. The classical approach has been used in this work as the objective is to present the study of extinction limits; however, it is accepted that implementation of both methods could enhance the laminar flame speed results detailed in this analysis.

3.6.1.2 Flame stretch rate

Laminar flame speed is subjected to curvature and non-stationary effects during flame propagation using the spherically expanding method. Also Lewis number (**Le**) nonlinearity of the blend is influenced by these effects provoking opposite trends in flame speed for lean and rich mixtures [31]. Flame stretch effects encompass both phenomena. The flame stretch rate (***α***) can be defined as a measure of the deformation of the flame surface resulting from its motion and the underlying hydrodynamic strain. The intensity of the stretch without the occurrence of cellular structure is represented by ***α***, defined in this work as the normalised differential change in flame surface area (***A***) as a function of time given by **Eqn. 3.3**:

$$\alpha = \frac{1}{A}\frac{dA}{dt} = \frac{2}{r_{sch}}\frac{dr_{sch}}{dt} = \frac{2}{r_{sch}} S_n \qquad (3.3)$$

Stretch effects exist because of coupling between flame surfaces and flow fields. Bradley et al. [44] gave a unified equation of the total stretch rate in terms of both two components of stretch, defining them as those attributed to flame curvature and those influenced by flow-field strain, as given in the expression below (**Eqn. 3.4)** explained the influence of Markstein length (***L_b***) on flame propagation, describing it as the parameter which expresses variations in burning velocity due to stretch associated with curvature and strain.

$$\alpha = \alpha_c + \alpha_s \qquad (3.4)$$

3.6.1.3 Linear extrapolation method

Flame speed can be affected by stretch; however it has been shown that in many cases this effect varies approximately linearly with the associated stretch rate, with the influence also qualitatively dependent on the deviation of ***Le*** from unity.

The linear relationship between stretch and flame speed has been presented as in **Eqn. 3.5**, with the gradient defined as the burned gas Markstein length (***L_b***) [46, 51, 111] and the unstretched flame speed (***S_L***) obtained by extrapolating to an intercept value of S_n at $\alpha = 0$:

$$S_L - S_n = L_b \alpha \tag{3.5}$$

3.6.1.4 Non-linear extrapolation method

More recent studies [51] have shown in some cases, linear extrapolation may lead to inaccuracy in determination of unstretched flame speed, as such a relationship proposed by Kelly and Law [50] takes into account the nonlinearity of S_n against α when the flame is heavily influenced by stretch, especially in lean and rich regions, and is given by **Eqn. 3.6**.

$$\left(\frac{S_n}{S_L}\right)^2 \ln\left(\frac{S_n}{S_L}\right)^2 = -\frac{2L_b\alpha}{S_L} \tag{3.6}$$

Difference in L_b measured between each methodology was underlined in previous work [51]. This is attributed to overestimation of the stretch influence induced by the linear methodology. There also appears through the following chapters to be higher relative dispersion in L_b data, with a respective averaged standard deviation of four and five percent, for the linear and non-linear techniques.

3.6.1.5 Laminar burning velocity

Using continuity and quasi-steady, quasi-planar and constant pressure assumptions the unstretched laminar burning velocity (u_L) may be obtained from S_L by applying the density ratio of burned (ρ_b) and unburned gases (ρ_u); given by **Eqn. 3.7**.

$$u_L = S_L\left(\frac{\rho_b}{\rho_u}\right) \tag{3.7}$$

In this body of work theoretical values were calculated by chemical kinetic models using GRI-Mech [112] and San Diego [113] mechanisms in the Premix coded package CHEMKIN™ at different initial conditions.

3.6.2 Selection of appropriate data

Along with initial pressure and temperature effects, several authors [17, 50, 51, 114] have underlined the impact of ignition energy and confinement on the data selected for linear and nonlinear extrapolations of flame propagation, required to quantify values of $\boldsymbol{S_L}$.

Bradley et al. [108] proposed that the flame kernel growth was unaffected by the spark energy at a critical radius of approximately 6mm. However, in the context of previous works suggest several scenarios resulting from spark influence on stretched flame propagation; firstly, when the ignition energy is low, the apparent flame front initially decelerated before accelerating back up to a characteristic propagation speed as stretch decreased. Conversely, an increase in spark energy, to levels above the minimum ignition energy can lead to an enhancement in initial flame speed owing to higher levels of heat release [108], before slowing back to a more characteristic speed. It was highlighted that this phenomena was exacerbated when the flame was less influenced by stretch, minimum ignition energy was low, and the heat release rate from the flame was enhanced. Therefore, for this study to ensure the effects of spark were negated when utilising the non-linear extrapolation equation to attain $\boldsymbol{u_L}$, a minimum value of 10 mm was applied.

Confinement of reactants ahead of the flame front results in a pressure rise (together with temperature from reactant compression), as such there in any closed volume combustion vessel there is a limited usable flame radius to which propagation is deemed pressure unaffected. For this investigation a maximum value of 38 mm was adopted, which was equal to ~0.66% of the chamber volume, which is comparable to equivalent values published in the literature by several authors [49, 50, 115, 116] who infer values between 0.5-1.25% of the combustion chamber volume representing their pressure unaffected region. Moreover, Burke et al. [114] indicated that the effect of confinement can be negated for flame radii less than 0.3 of the wall radius (r_w), while still achieving acceptable accuracy. Hence to ensure the data presented in this body of work is neither spark nor pressure effected a typical usable range of flame radii between 10 and 38 mm was adopted from which values of S_L and L_b could be derived.

3.6.3 Preparation of fuels samples

Within this study the grade of ethanol and methanol used was a Sigma Aldridge reagent grade (≥ 99.7%). Methane and Propane used was a BOC grade N2.5 (≥ 99.5) compressed gas.

To ensure accuracy of results, the equivalence ratio was rigorously determined using a partial pressure method and validated in the case of liquid fuels by calculation of mass of fuel injected. A precision scale was used to weigh a specified mass before introducing it to the chamber via syringe, through a self-sealing septa housing. Gaseous fuels were introduced through a manifold with fine needle valve control. Dry synthetic air was subsequently supplied using high precision MFC to regulate to the desired initial pressure and equivalence ratio. The calculation of AFR was carried out using the following equations (**Eqns. 3.8 - 3.9**) in order to determine the method of controlling fuel to oxidiser ratio during experimentation.

By using the stoichiometric air fuel ratio (AFR_{stoich}) and equivalence ratio ($Ø$) the following expression was obtained, where m_{fuel} and m_{ox} are the masses of fuel and oxidiser, respectively.

$$m_{fuel} = \frac{m_{ox}\phi}{AFR_{stoich}} \tag{3.8}$$

From **Eqn. 3.8** and employing both the ideal gas law and Dalton's law, an expression can be derived for calculating the $\boldsymbol{m_{fuel}}$ to inject into the constant volume of the chamber (***Vol***) in which the fuel was to measure at different initial conditions. As such $\boldsymbol{P_T}$ is the total pressure required pre combustion, $\boldsymbol{R_u}$ is the ideal gas constant, $\boldsymbol{AFR_{actual}}$ is the actual air fuel ratio, $\boldsymbol{T_{fuel}}$ and $\boldsymbol{T_{ox}}$ are the fuel and oxidiser temperatures, respectively, and $\boldsymbol{M_{fuel}}$ and $\boldsymbol{M_{ox}}$ are the molar masses of the fuel and oxidiser, respectively.

$$m_{fuel} = \frac{\dfrac{P_T Vol}{R_u}}{\dfrac{T_{fuel}}{M_{fuel}} + \dfrac{AFR_{actual} T_{ox}}{M_{ox}}} \tag{3.9}$$

The masses are then subsequently used to calculate the number of moles of the fuel and oxidiser required ($\boldsymbol{n_{fuel}}$ and $\boldsymbol{n_{ox}}$), thereby allowing the calculation of the partial pressures of both the fuel and oxidizer ($\boldsymbol{P_{fuel}}$ and $\boldsymbol{P_{ox}}$).

$$P_{fuel} = P_T \frac{n_{fuel}}{n_{fuel} + n_{ox}} \tag{3.10}$$

$$P_{ox} = P_T \frac{n_{ox}}{n_{fuel} + n_{ox}} \tag{3.11}$$

A more comprehensive derivation of this process is provided in **Appendix C**.

3.6.4 Development of experimental procedure

The general procedure for combustion experiments within the CVCC is presented below followed by specific procedures when liquid and gaseous fuels were employed in the experimental programme.

3.6.4.1 General combustion procedure

a) Set TCU to the required pre combustion ambient temperature, allowing sufficient time for the CCVC to stabilise with a uniform heat distribution.

b) Confirm uniformity of temperature by comparing distributed calibrated thermocouples.

c) Ensure all pipe-work and chamber are leak tight, by pulling a vacuum using the vacuum pump, and that entire system is in good working order including mixing fans and associated seals and that ignition system is operational.

d) Calibrate HSC and Schlieren setup by taking optical scaling measurements utilising digital Vernier callipers.

e) Configure DAS and ensure data is logging to correct directory with sufficient space for data files.

3.6.4.2 Liquid fuels

1) Conduct steps (a-e).
2) Prior to each experiment purge the chamber with clean dry air, and fully evacuated a further twice to < 30 mbar to ensure any residual exhaust gas from previous trials is removed. Thus limiting the resultant maximum contamination error to <0.01% vol.
3) At the desired unburned pressure and temperature of oxidiser, calculate the required mass of liquid fuel to be tested for the desired equivalence ratio.
4) Withdraw correct mass of fuel into syringe and confirm weight using precision balance ensuring accuracy of $\boldsymbol{AFR}$. When chamber is at correct conditions inject fuel through the self-sealing septa.
5) Leave a sufficient period of time – dependant on the equivalence ratio and fuel injected – to ensure fuel is completely vaporised.
6) Fill CCVC to the required starting pressure with the oxidiser.

7) Energise fans to instigate reactant mixing for approximately 90 seconds, and then turn off fans allowing turbulence to subside.
8) Ensure required temperature of calibrated live readout from DAS is maintained.
9) Initiate Data capture of high frequency pressure transducer.
10) If safe to do so press ignition switch to simultaneously trigger ignition system and HSC camera image capture.
11) After ignition and combustion witnessed evacuate all products from the chamber.
12) Download all pressure and temperature data, together with video files to relevant storage file.

3.6.4.3 Gaseous fuels

1) Conduct steps (a-e).
2) Prior to each experiment purge the chamber with clean dry air, and fully evacuated a further twice to < 30 mbar to ensure any residual exhaust gas from previous trials is removed. Thus limiting the resultant maximum contamination error to <0.01% vol.
3) Using relevant valves fill gaseous fuel to the calculated partial pressure required for the set equivalence ratio.
4) Fill CCVC to the required starting pressure with the oxidiser.
5) Energise fans to instigate reactant mixing for approximately 90 seconds, and then turn off fans allowing turbulence to subside.
6) Ensure required temperature of calibrated live readout from DAS is maintained.
7) Initiate Data capture of high frequency pressure transducer.
8) If safe to do so press ignition switch to simultaneously trigger ignition system and HSC camera image capture.

9) After ignition and combustion witnessed evacuate all products from the chamber.
10) Download all pressure and temperature data, together with video files to relevant storage file.

The following section describes the Experimental Method and Procedures used in Chapter 7 underlining the difference between this chapter and the Chapter 5 and 6. It is important to note that the same Schlieren setup, Ignition system and Data processing methods were used for the study of flame mist propagation.

3.7 Dynamic Cylindrical Constant Volume Chamber setup

In order to study flame propagation through two phase vapour/mist fuel air combustible mixtures. New components were added to the CCVC setup shown in Section 3.2 namely; a pneumatic cylindrical actuator (PCA), a piston (P1), the Malvern Instruments Spraytec system comprising an electronic interface (EI), emitter and receiver optics canisters (EOC and ROC), and the associated DAS, valves and connections. A schematic setup of the new experimentation unit, henceforth referred to as the Dynamic Cylindrical Constant Volume Chamber (DCCVC) is given in **Figure 3.8**.

The double acting PCA was manufactured by NORGREN type PRA/182063/M/180 with a cylinder diameter of 63mm, effective stroke length of 160mm, and maximum operating temperature and pressure of 80°C and 16bar, respectively. This device was attached to the piston (P1) in order to provide a rapid decompression in the chamber provoking a drop in temperature of the reactants, hence, forcing the saturated vapour out of the gas phase resulting in a mist formation inside the chamber. The size distribution of the droplets were subsequently measured by the Malvern Instruments Spraytec system's laser beam which crosses the internal span between the emitter and receiver optics (EOC and ROC), details of the measurement technique are described in detail in the following section.

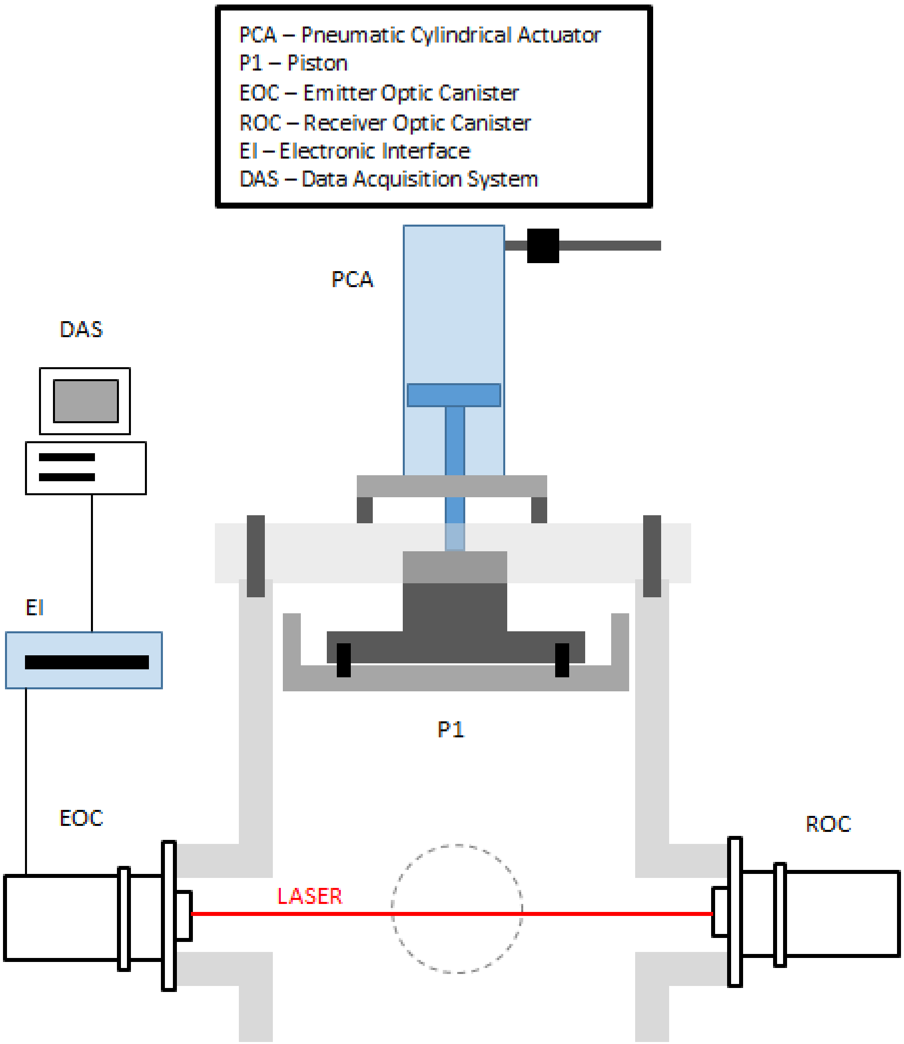

Figure 3.8 Schematic setup of the additional devices to cylindrical constant volume combustion chamber (DCCVC)

3.7.1 Malvern Spraytec system

The Spraytec system is capable of continuous measurement of particle size distribution for aerosol sprays and jets using a laser diffraction technique [117]. In the present work this system was utilised to capture the droplet size of the mist produced by the rapid decompression that took place in the chamber. The Spraytec with associated optics used in this study provides particle measurement in the size range from 0.5 to 1000 microns at measurement rate of up to 2.5 kHz, which was deemed suitable for the expected mists anticipated to have a size distribution in the 5-25 micron range.

The Spraytec setup is shown in **Figure 3.9**. The measurement region of the Spraytec is located in the middle of the chamber's windows, at a slightly higher elevation than that of the electrodes to ensure they do not obstruct the 10mm diameter laser beam, due to the chamber having 4 viewing windows simultaneous Schlieren and laser measurement could be conducted at right angles to one and other across the same measurement volume.

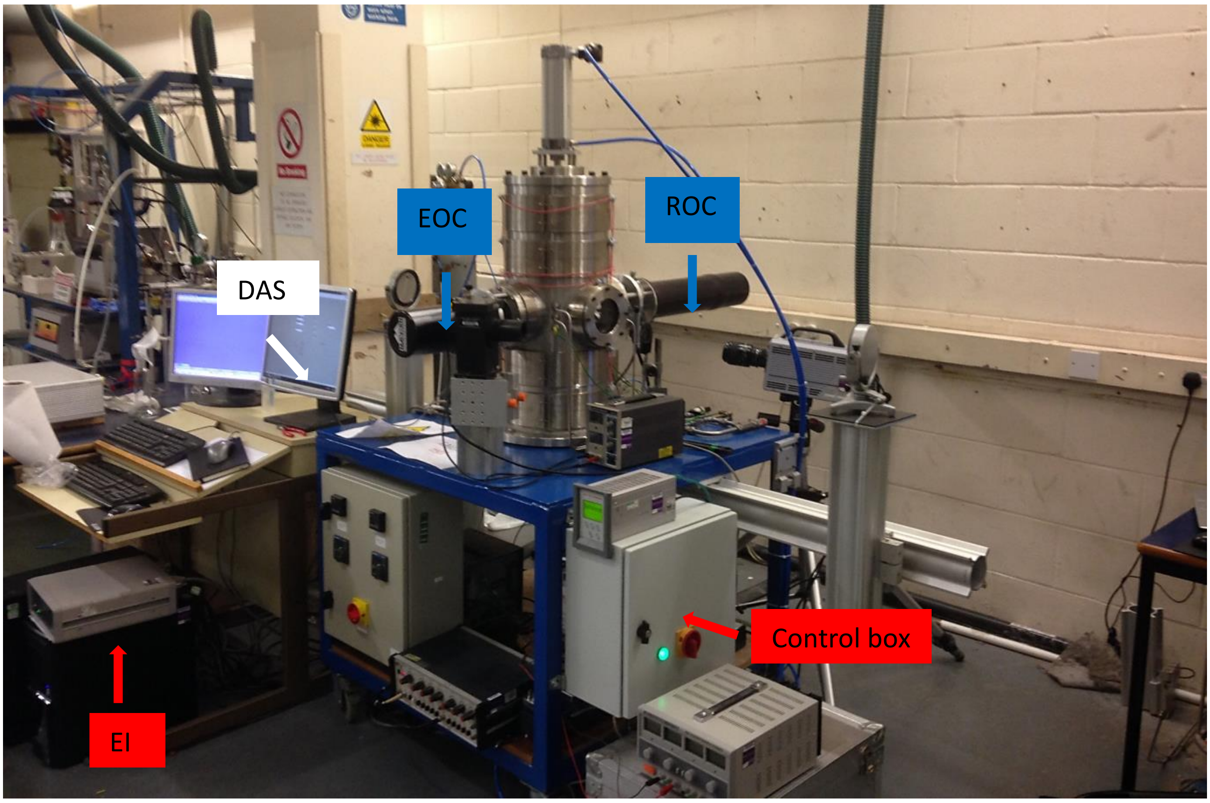

Figure 3.9. Picture showing the Spraytec setup and the devices for the implementation of the Schlieren technique.

The raw scattering data was acquired and transmitted to the computer interface card. Processed scattering data was saved to the PC's hard drive, where the RTSizer™

software was used to interpret into size distribution information. This software will be explained in detail in section 3.7.3.2.

3.7.2 Capturing scattering pattern fundamentals

This section describes the principles of the Spraytec operation through the following diagrams:

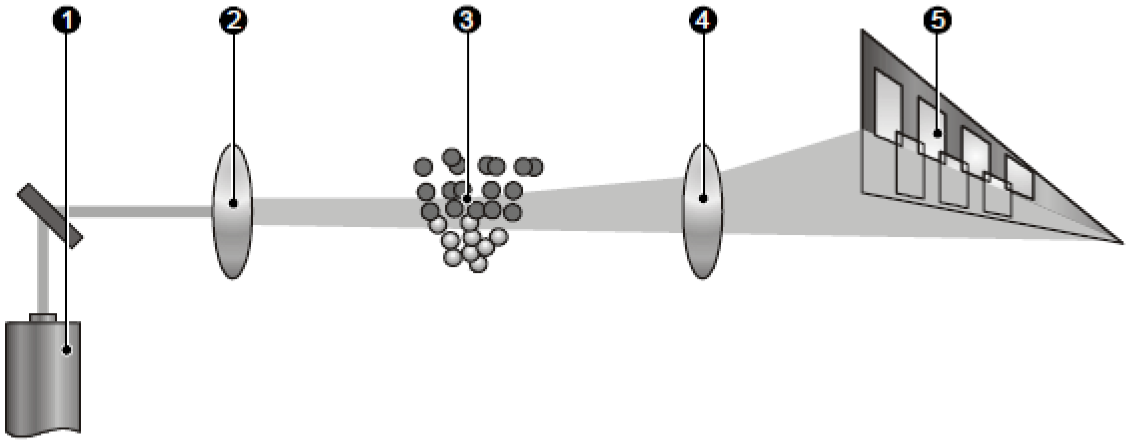

Figure 3.10. Diagram of fundamentals of the Spraytec measurement.

Figure 3.10 shows how the laser's light (1) is first expanded - in order to provide a wide parallel beam - by the collimating optics (2), the light is subsequently scattered by the mist droplets (3), before a Fourier lens (4), is used to focus the scattered light onto the detector array (5) where a measurement is made.

At the centre of the detector array (5) there was a pinhole in which the unscattered light unaffected by the focusing lens (4), provides a measurement of the total light transmitted straight through the mist (***Tr***), this gives a measure of the mists density.

The following diagram (**Figure 3.11**) illustrates how the angle of diffraction is used to determine the size of different particles. The angle at which a particle diffracts light is inversely proportional to its size [118]. An array of 32 individual detectors is used to collect the light scattered at a particular range of angles, with each detector assigned an individual channel, from which a size distribution can be determined.

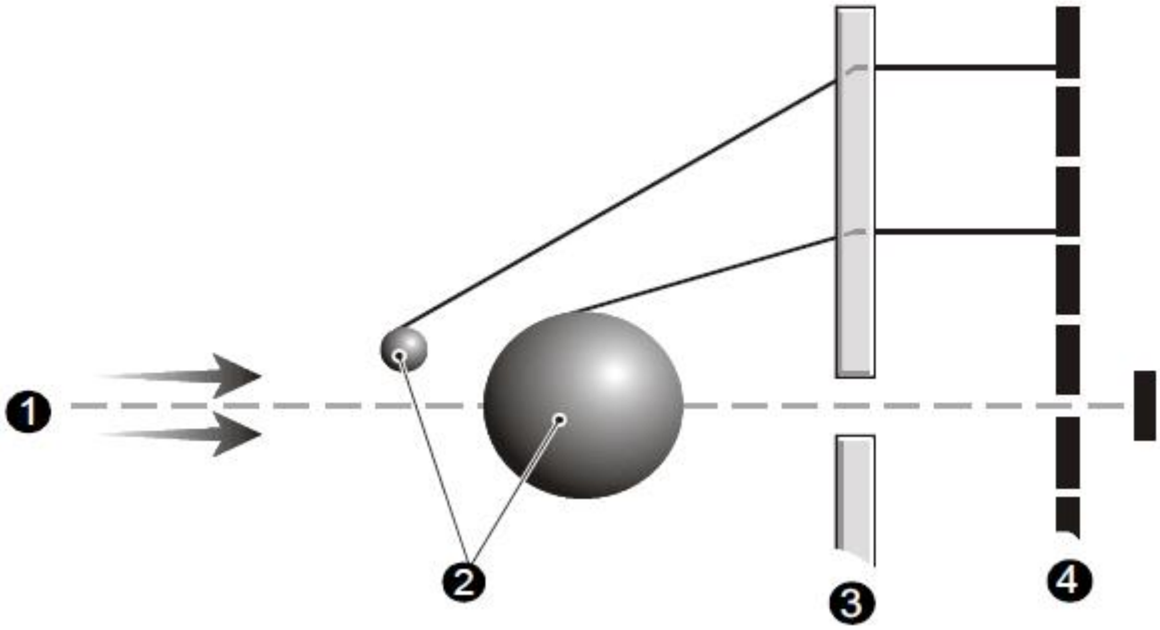

Figure 3.11. Diagram of different particles sizes and the detector array.

The light source (1) intercepts mist droplets of different sizes (2) causing a different scattering angle, which is subsequently focused the by the lens (3) to a particular detector array (4).

3.7.3 Data Acquisition System

In a similar way to Chapter 6 methodology data sets were obtained in Chapter 7 employing Data Logging system for measuring temperature and pressure with some modifications such as the addition of pneumatic control along with the synchronization of the ignition spark, imaging capture and mist droplets diameter measurements which are explained bellow. The use of the RTSizer™ software and the Flash Mode will also present.

3.7.3.1 Data Logging System

In a similar way NI cRIO-9012 was also employed as a data logging system along with the two modules used in chapters 5 and 6 methodology for measuring temperature and pressure by using also the NI LabVIEW program. However, a new main screen was designed capable not only of measuring the initial temperature and live pressure trace, but to control and synchronise ignition spark, piston retraction and imaging capture. It is important to note that live temperature readings were not able to be obtained due to the limitation in time response from two k-type thermocouples. Therefore, it was decided to approximate the temperature drop caused by rapid decompression using the ideal gas law, from the initial and final pressures and volumes given a constant mass of combustion mixture.

3.7.3.2 RTSizer™ software

The RTSizer software was able to continuously collect particle size information and report both the particle size distribution and pertinent attributes of this distribution [119]. There were two separate measurement options with which this data could be collected; ‘The Time History Window’ mode that allowed data acquisition at 1-2 seconds updates interval or using the ‘Flash Mode’ module which was the one used in the present work for acquiring data at rates of up to 2500 Hz. In the latest mode the user must specify the time period and data acquisition rate for measurement due to displaying the size distribution data in real time is not possible. More details are given in the following section.

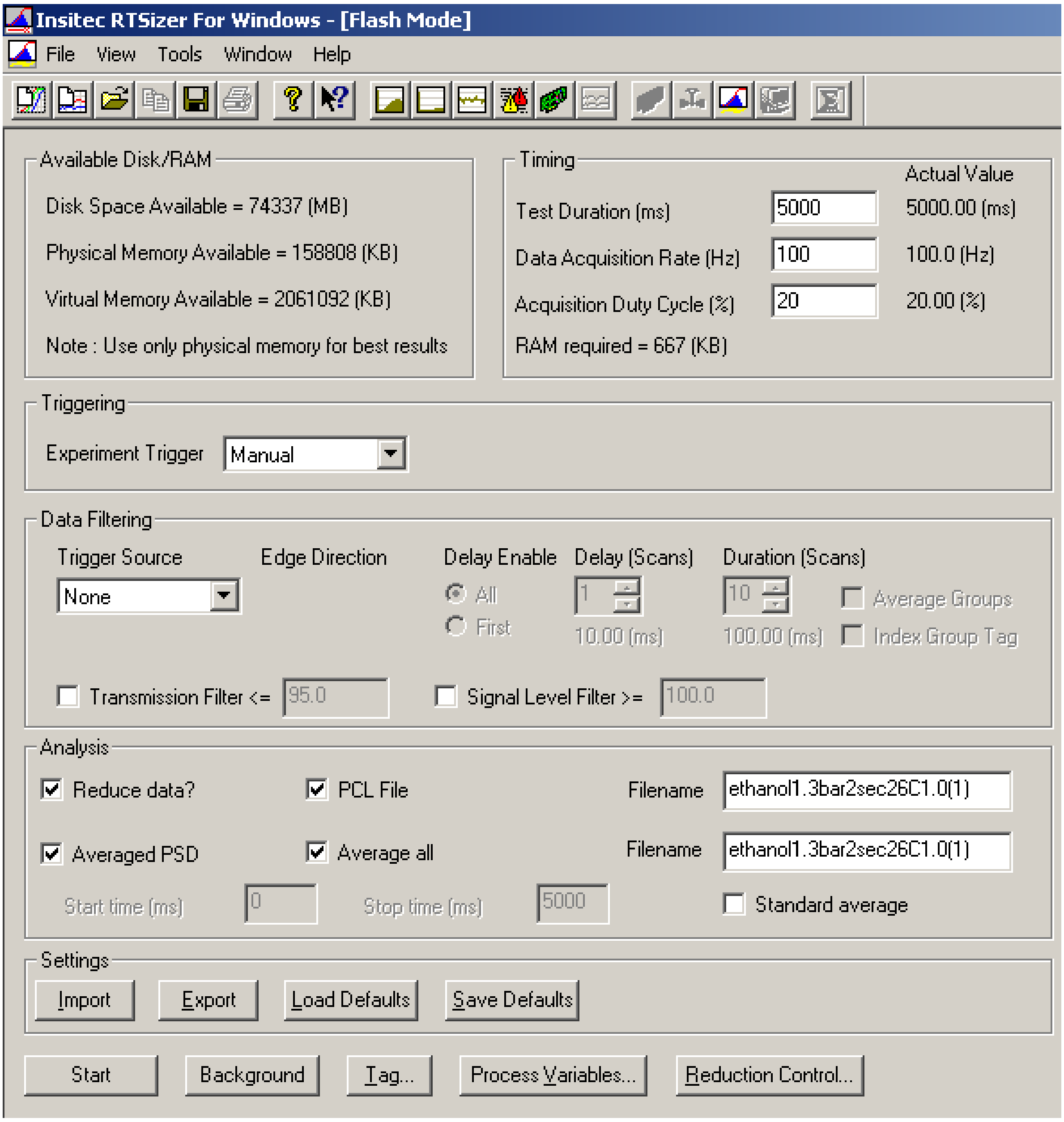

Available Disk/RAM

Disk Space Available = 74337 (MB)

Physical Memory Available = 158808 (KB)

Virtual Memory Available = 2061092 (KB)

Note : Use only physical memory for best results

Timing

		Actual Value
Test Duration (ms)	5000	5000.00 (ms)
Data Acquisition Rate (Hz)	100	100.0 (Hz)
Acquisition Duty Cycle (%)	20	20.00 (%)

RAM required = 667 (KB)

Triggering

Experiment Trigger: Manual

Data Filtering

Trigger Source: None

Edge Direction

Delay Enable: ● All ○ First

Delay (Scans): 1 — 10.00 (ms)

Duration (Scans): 10 — 100.00 (ms)

☐ Average Groups

☐ Index Group Tag

☐ Transmission Filter <= 95.0

☐ Signal Level Filter >= 100.0

Analysis

☑ Reduce data?

☑ PCL File — Filename: ethanol1.3bar2sec26C1.0(1)

☑ Averaged PSD

☑ Average all — Filename: ethanol1.3bar2sec26C1.0(1)

Start time (ms): 0

Stop time (ms): 5000

☐ Standard average

Settings

Figure 3.12. Snapshot of the Flash Mode dialog.

3.7.3.3 Flash Mode

As previously mentioned this mode is designed to measure particle size distribution data at a high rate of acquisition with available rates from 1 to 2500 Hz. The Flash Mode dialog is shown in **Figure 3.12**.

Before starting the measurement process it is necessary first to set the acquisition speed, triggering mechanism, data reduction settings and process variables. In the present work the time that it took the piston to reach the top of the chamber was approximately

800ms; therefore, for safety reasons the minimum ignition spark time was set to 1 second after piston retraction initiation; otherwise, the explosion could take place before the piston reached its final position causing unnecessary stress on the equipment. In the present work the total test duration was set up to 5 seconds, the data acquisition rate was set to 100 Hz and the triggering mode was set to manual.

When all data was completed a new ‘Time History Window’ file was created displaying the record view shown in **Figure 3.13**.

Three views are shown in a typical record; at the top left-hand side ‘Measurement Parameters’ view gave textual information on the way the instrument was set up. At the top right-hand side ‘Particle Size Distribution’ view showed a histogram and a cumulative “percent volume smaller than” line, and finally at the bottom ‘Process Control variable Time History: Size vs Transmission’ view displayed the droplet size and transmission transient development. During this work the droplet size growth reached its peak approximately after one second and remained constant for almost a further two seconds.

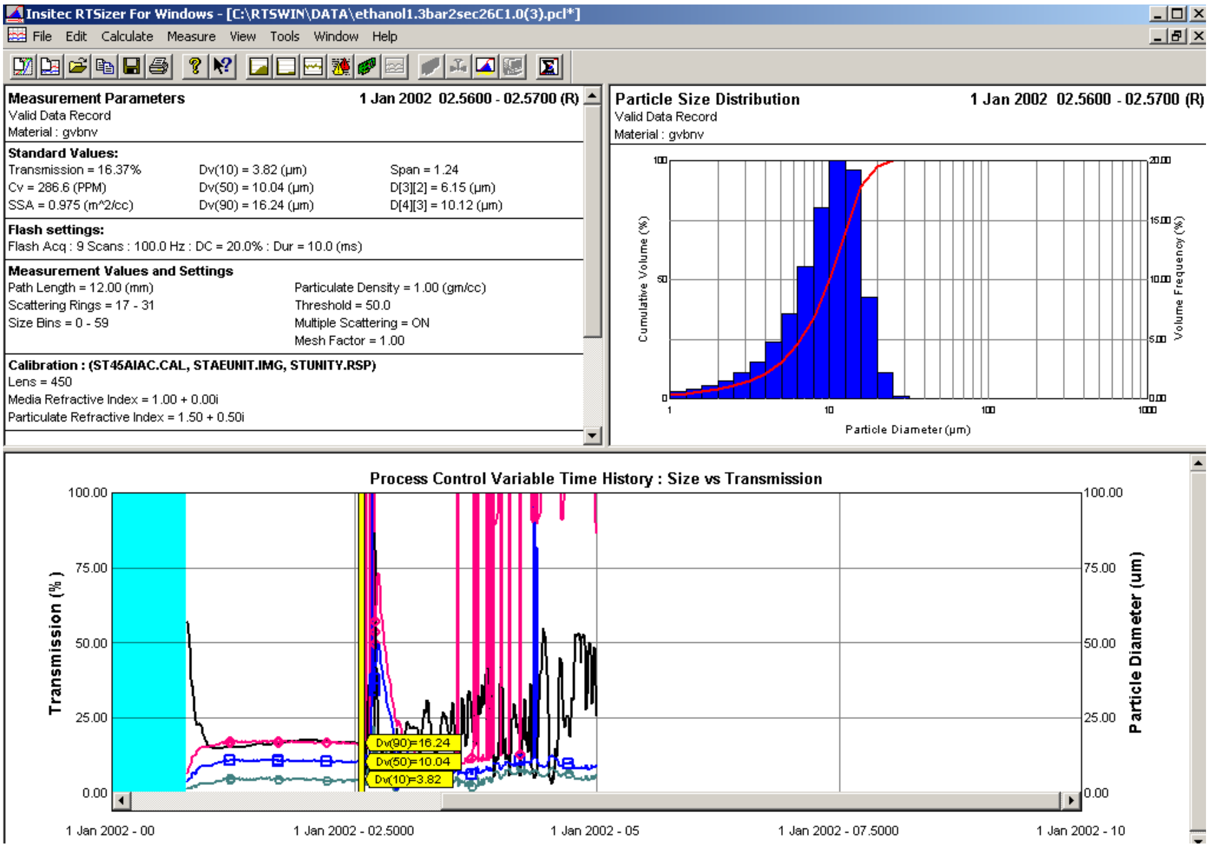

Measurement Parameters **1 Jan 2002 02.5600 - 02.5700 (R)**
Valid Data Record
Material : gvbnv

Standard Values:
Transmission = 16.37%
Cv = 286.6 (PPM)
SSA = 0.975 (m^2/cc)
Dv(10) = 3.82 (µm)
Dv(50) = 10.04 (µm)
Dv(90) = 16.24 (µm)
Span = 1.24
D[3][2] = 6.15 (µm)
D[4][3] = 10.12 (µm)

Flash settings:
Flash Acq : 9 Scans : 100.0 Hz : DC = 20.0% : Dur = 10.0 (ms)

Measurement Values and Settings
Path Length = 12.00 (mm)
Scattering Rings = 17 - 31
Size Bins = 0 - 59
Particulate Density = 1.00 (gm/cc)
Threshold = 50.0
Multiple Scattering = ON
Mesh Factor = 1.00

Calibration : (ST45AIAC.CAL, STAEUNIT.IMG, STUNITY.RSP)
Lens = 450
Media Refractive Index = 1.00 + 0.00i
Particulate Refractive Index = 1.50 + 0.50i

Figure 3.13. Snapshot of the record view.

3.7.4 Preparation of fuel samples

The mass of both liquid fuel and air were achieved using Antoine Equation that allowed calculating the vapour pressure of liquid fuel $\boldsymbol{P^0}$ given the temperature and validated by calculation of partial pressure method.

$$\log_{10} P^0_{fuel} = A - \frac{B}{T+C} \tag{8}$$

Where A, B and C are constants [120]. A precision scale was used to weigh a specified mass before introducing it to the chamber via syringe, through a self-sealing septa housing. Dry synthetic air was subsequently supplied using high precision MFC to regulate the desire initial pressure and equivalence ratio. This procedure was carried out using the following equations in order to determine the method of controlling fuel to oxidiser ratio during experimentation.

By using the ideal gas law the following expression was obtained, where $\boldsymbol{R_{fuel}}$ and $\boldsymbol{R_{ox}}$ are the specific gas constant of fuel and oxidizer, respectively.

$$m_{fuel} = \frac{M_{fuel} P^{0}_{fuel} Vol}{R_{fuel} T} \qquad (9)$$

$$m_{ox} = \frac{M_{ox} P_{ox} Vol}{R_{ox} T} \qquad (10)$$

From the above equations and employing the ***AFR*** for ethanol the desirable equivalence ratio (***Ø***) was obtained.

3.7.5 Development of experimental procedure

Before starting to use Spraytec for obtaining size distribution measurements, the following steps were followed:

a) The 'Scattering' mode was displayed. In order to check the system alignment and the background light scattering level this module was used. The system is aligned when the beam power (ring 0) is maximized and the rest of the beams are minimised.

b) The 'Reference Noise' was recorded (this measurement was typically done once every day). This reference noise is the measurement of a dark background measurement, or in other words, a measurement of the electronic noise present in the system.

c) The ‘Background’ scattering pattern was measured in order to eliminate any errors caused by drift in the background scattering levels. This error was minimised owing the study region was inside the pressurised chamber.

3.7.5.1 Combustion procedure

1) Conduct steps (a-e) as discussed in section 3.6.4.2.
2) Prior to each experiment with the piston down, purge the chamber with air, and fully evacuate twice to < 30 mbar to ensure any residual exhaust gas is removed, resulting in a maximum contamination error of <0.01% vol.
3) At the desired unburned pressure and temperature of oxidiser, calculate the required mass of liquid fuel to be tested for the desired equivalence ratio.
4) Withdraw correct mass of fuel into syringe and confirm weight using precision balance ensuring accuracy of $\boldsymbol{AFR}$. When chamber is at correct conditions inject fuel through the self-sealing septa.
5) Leave a sufficient period of time – dependant on the equivalence ratio and fuel injected – to ensure fuel is completely vaporised
6) Fill of DCCVC to the required staring pressure with oxidiser.
7) Energise fans to instigate reactant mixing for approximately 90 seconds, and then turn off fans allowing turbulence to subside.
8) Ensure required temperature of calibrated live readout from DAS is maintained.
9) Initiate Data capture of high frequency pressure transducer.
10) If safe to do so press ignition switch to simultaneously trigger ignition system, piston retraction, droplet size distribution and HSC camera image capture.
11) Positioned the piston at the start point (down).
12) After ignition and combustion witnessed evacuate all products from the chamber
13) Download all pressure and temperature data, together with video files and droplet size to relevant storage file.

3.8 Summary

The materials, methods, and procedures involve in the laboratory experiments carried out in this study were discussed in this Chapter. The Cylindrical Constant Volume Chamber (CCVC) setup was explained in section 3.2 while the main features of the Schlieren setup and Ignition system were outlined in section 3.3 and 3.4, respectively. Schematic illustrations were shown of the setups of the experimentation unit, namely, the CCVC with 8 band-heaters, 4 thermocouples and the temperature control unit (TCU), the CCVC with all the devises necessary for the implementation of the schlieren technique, the schematic representation of ignition system, and the DCCVC setup. In section 3.5 the data acquisition and processing systems were explained. Aspects of the data logging system were described, followed by the capture and determination of the flame front data using the bespoke Matlab® script. The outwardly-propagating spherical flame method for obtaining the laminar burning rate was outlined and the outcomes of the tests were processed using two extrapolation methods described in sections 3.6.1.3 and 3.6.1.4. Selection of appropriate data and preparation of fuel samples were described in sections 3.6.2 and 3.6.3, respectively. For the study of flame mist propagation the Dynamic Cylindrical Constant Volume Chamber (DCCVC) setup was presented in section 3.7 along with the Malvern Spraytec system in section 3.7.1, the capturing scattering pattern fundamentals in section 3.7.2, and the data acquisition system in section 3.7.3. The general combustion procedure of each experiment was presented followed by the procedures of liquid and gaseous fuels with which an experimentally programme was conducted at the end of each section. The physical experimentation results obtained are discussed in Chapters 5, 6 and 7.

Chapter 4

"Science wins when its wings are uninhibited with imagination."

Michael Faraday

Analysis of 'under-driven' Methane/Water-Vapour/Air Flames in Early Stages

4.1 Chapter Overview

An analysis of a detailed experimental investigation of the effect of water vapour as a suppressant on freely propagating methane flames was conducted. Through this study, data from Crayford [102] was used to generate the work presented by Crayford et al. [76] which is included in more detail in this chapter. A Cardiff University cloud chamber, was utilized to investigate the effects of equivalence ratio, water concentration, initial temperature and ignition energy on outwardly-propagating spherically flames. Laminar flame speed (S_L) and Markstein length (L_b) have been measured using a modified linear extrapolation method derived from numerous experiment repeat points, highlighting that utilising a low ignition energy system early non-linear stages of the flame propagation are observed, a phenomena fully studied in the subsequent chapters of the present thesis. The use of a proposed method for evaluating the extinction stretch rate (K_{ext}) using spherical flame propagation was presented for the first time in this work.

4.2 Introduction

Water has been considered as an explosion suppressant, for many years, due to its benign nature and relative abundance with comprehensive studies found in literature [121-128]. The effect of water on freely propagating flames was studied in order to have a better understanding of the interaction of water vapour on highly stretched propagation flames. This interaction along with low ignition energy effect provoked that fundamental studies of non-linear trajectories of early flame propagation were analysed in the present work. Not only the suppression effect of water vapour on explosions was investigated, but also the effects of low ignition energy and stretch as a potential method for evaluating extinction in outwardly-propagating spherically flames.

4.3 Experimental Methodology

The cylindrical stainless steel combustion bomb used in this study was different to that described previously in Chapter 3 and the rig was developed from a Cardiff University designed 'Cloud Chamber' which is fully described elsewhere [15, 102, 129]. The cylinder has an internal diameter of 120mm, enclosed at one end by a round quartz window and on the other by a round flat piston head, attached to a pneumatically driven piston facilitating initial pre-combustion volumes of 910-1650cm^3.

Optical access was afforded via two diametrically opposed rectangular (45x60 mm) quartz windows which were centrally aligned perpendicular to the electrodes. A custom heating jacket afforded initial temperatures in the range of 298-373K. Methane (CP grade 99.7%) and distilled water were injected into the chamber utilising high precision gas tight syringes and micro-pipettes, respectively. Well-mixed combustion blends were ensured using a gas tight oil-free heated recirculation system.

Due to the necessity for the water to be present as a vapour in the combustible mixture it was necessary to raise the initial temperature from atmospheric condition to ensure that a sufficient vapour pressure could be achieved. All vapour experiments were conducted at either 323 K which allowed the study of 0, 5 and 10% water vapour fractions or 373 K affording the measurement of 0, 5, 10 and 15% water vapour fractions. Temperature readings had an accuracy of ± 2 K. The combustion mixture was equilibrated to 1013 mbar prior to ignition.

To guarantee repeatability of data typically 5 nominally identical repeats of each experiment were undertaken. It is important to note that owing to the relatively small cloud chamber’s volume and that the high speed camera was set to 1,000 fps, limited data per experiment was achieved. However from the 5 nominally repeats a minimum of 18 reliable data points were combined ensuring the derivation of sufficient data to apply the linear extrapolation method as is given by **Figure 4.1**. To establish a representative value of S_L and L_b, instantaneous values of S_n and α from the differential of the fitted polynomial function at each of the values of r_{sch} in the spark and pressure unaffected region were derived following the methodology discussed in Chapter 3. This was conducted for each of the 5 individual repeats, and all unaffected data points plotted against each other to predict values of S_L and L_b.

4.4 Results

4.4.1 Dry Methane-Air Flames

Smooth spherical flame kernels were witnessed in all cases confirming that the mixture was quiescent and well blended. The flame radius was measured in the horizontal plane ensuring any electrode effects caused by surface cooling did not bias the flame speed measurement.

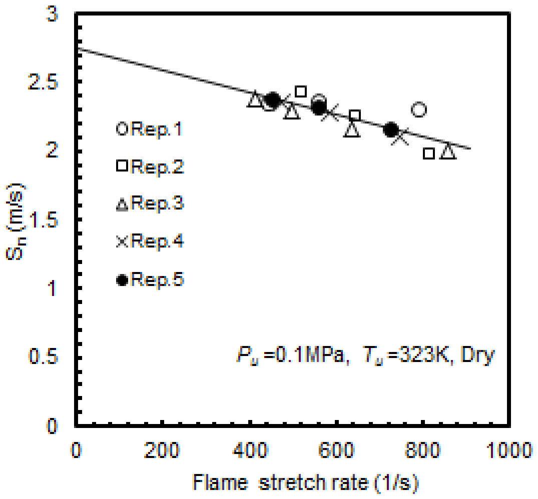

Figure 4.1. Five nominally repeats combined to apply the linear extrapolation method.

To determine the influence of water on initial flame propagation, care was taken to ensure that all experiments were undertaken utilising minimal ignition energies. The influence of ignition energy on early flame development is presented in **Figure 4.2**; as can be seen the higher ignition energies are shown to cause an early acceleration, 'overdriving' of the flame. However, even for the highest ignition energy case, this effect had decayed before reaching a flame radius of 6 mm, subsequently demonstrating good agreement with the work of others [108].

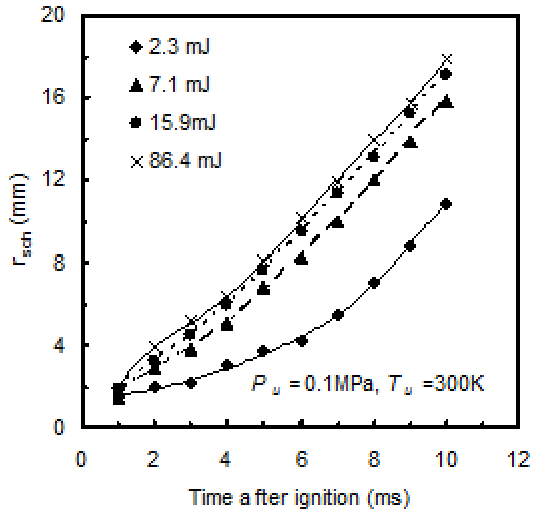

Figure 4.2 . Effect of ignition energy on early flame propagation.

A long region of slow flame growth was observed when low ignition energies were used, which could lead to the flame quenching. However, for flames that achieved self-sustained propagation it was noted that when the flame reached a radius of approximately 6 mm, the burning rate was similar to that measured by experiments utilising higher ignition energies.

The effect of equivalence ratio on flame growth is presented in **Figure 4.3**. It should be noted that in order to achieve self-sustaining flame propagation for each of the different mixtures, higher ignition energies were required under non-stoichiometric conditions, with highest energies required for the initiation of rich mixtures. Again for all mixtures it was shown that after a minimum flame radius of 6 mm the flame settled to a characteristic flame speed.

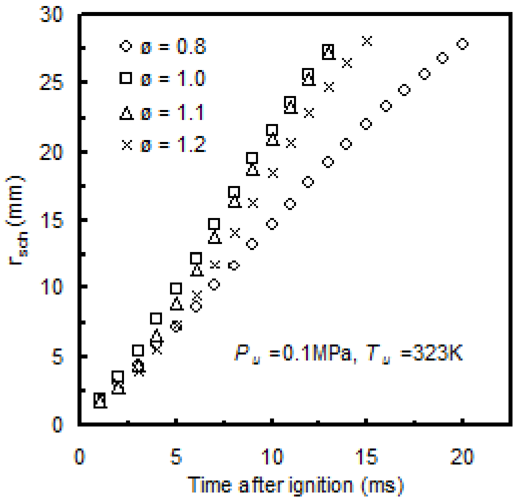

Figure 4.3 Effect of equivalence ratio on initial flame propagation.

To enable the effects of water vapour to be decoupled from ambient temperature, dry methane-air benchmark experiments were studied at elevated temperatures corresponding to the water vapour pressures necessary to give the required water loading fractions. The experimental set-up and methodology were shown to be repeatable, enabling the data from 5 individual experiments to be used to derive flame speeds and Markstein lengths for each case.

Dry methane-air data conducted at three different temperatures (298, 323, and 373K) are presented in **Figure 4.4**. Increasing temperature results in an increase in S_L as expected, and good agreement was noted with previous studies [46, 108].

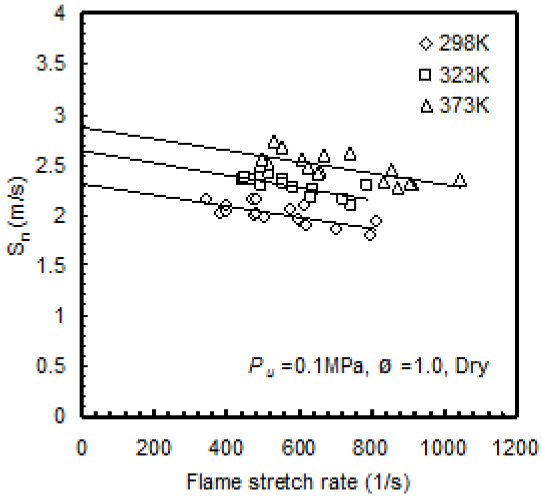

Figure 4.4 Measure flame speeds at different stretch rates at different unburned gas temperatures for dry methane-air mixtures.

4.4.2 Methane-Air-Water Flames

The experimental programme for mixtures including water vapour (V_w) comprised loadings of 5 and 10% (by volume) at 323K and 5, 10 and 15 % at 373K. The effect of water fraction on the measured flame speed is presented below (**Figure 4.5** and **Figure 4.6**).

Figure 4.5 shows that increasing water vapour fractions reduces S_L and increases L_b, with u_L at water loadings of 0%, 5% and 10% and unburned gas temperatures of 323K measured at 39.1 cm/s, 31.9 cm/s and 27.0 cm/s, respectively. Similar reductions in unstretched flame speed and increase in L_b are observed at 373 K (**Figure 4.6**) with u_L

of 46.1 cm/s, 42.6 cm/s, 33.7 cm/s and 30.9 cm/s observed for the 0%, 5%, 10% and 15% cases, respectively.

It is observed at the highest water loading fraction of 15% (**Figure 4.7**) that ***L_b*** and the corresponding ***u_L*** appear to be larger than expected.

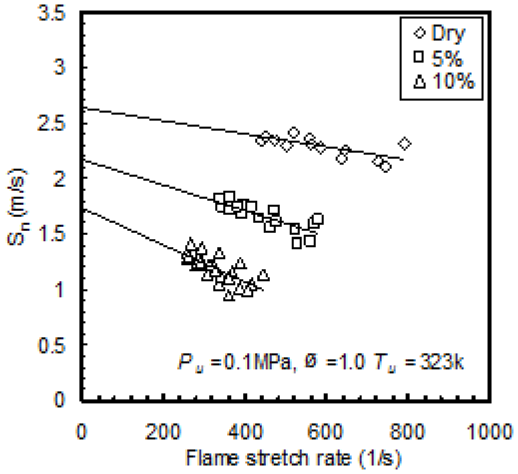

Figure 4.5 Measured flame speeds at different stretch rates for water loadings of 0%, 5%, and 10% for methane-air-water mixtures, *T* = 323K.

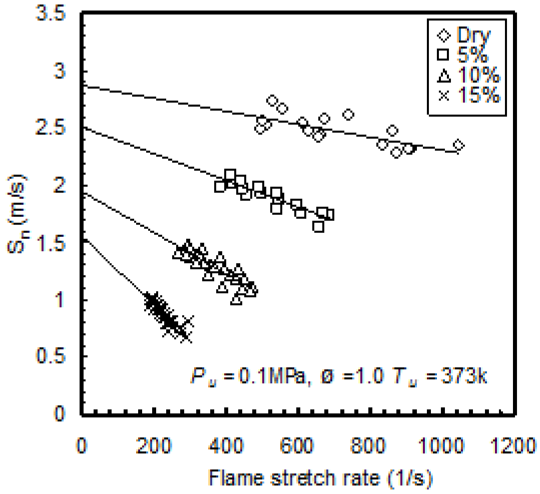

Figure 4.6 Measured flame speeds at different stretch rates for water loadings of 0%, 5%, and 10% for methane-air-water mixtures, *T* = 373K.

The reason proposed for this high value of L_b and corresponding over-predicted value of u_L is highlighted in **Figure 4.7** where seems to be a linear increase in L_b associated with increasing water loading fraction for both the 323 K and 373 K cases, up to a water fraction of 10 %. However, L_b for the 15 % case increases non-linearly to 3.6 mm.

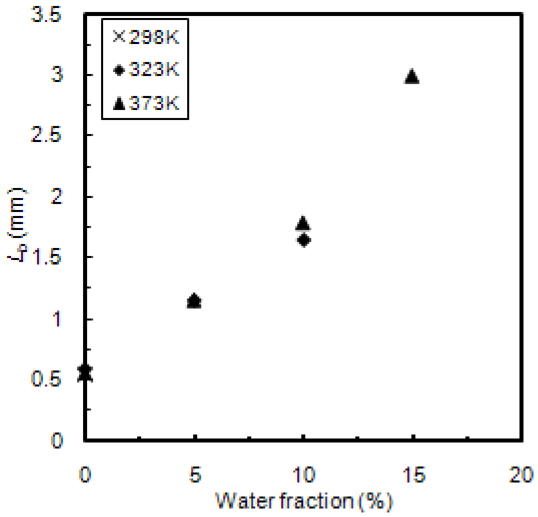

Figure 4.7 Effect of initial temperature and water vapour concentration on L_b using the linear extrapolation method.

Another reason proposed for this high value of L_b and corresponding over-predicted value of S_n is highlighted in **Figure 4.8**, which presents the flame speed versus stretch data for a single experiment with highest loading of 15%, due to the relatively slower flame speeds observed at high water loadings it is seen that even with the relatively small measurement volume and low filming rates that there are sufficient data points to investigate the early flame growth. The filled data points represent data for flames which were considered 'naturally propagating', unaffected by overdriven effects (at higher stretch rates, to the right) and data influenced by the effects of increased pressure due to interaction of the unburned gas with the chamber boundary walls (to the left), in line with definitions from previous studies [108, 114]. As can be seen in contradiction with early flame propagation works [46] the flame growth during this 'naturally propagating' flame region, assumed a definite non-linear trend, a phenomena which has been discussed more recently by [49-51]. As can be seen from the falling speed versus stretch on the right hand side of the graph, this flame had the requirement of excessively overdriving it, with high ignition energy in order to avoid flame quench in the early stages of flame growth. And it is seen that even after the suggested 6mm threshold that the flame appears to never attain a constant rate of acceleration.

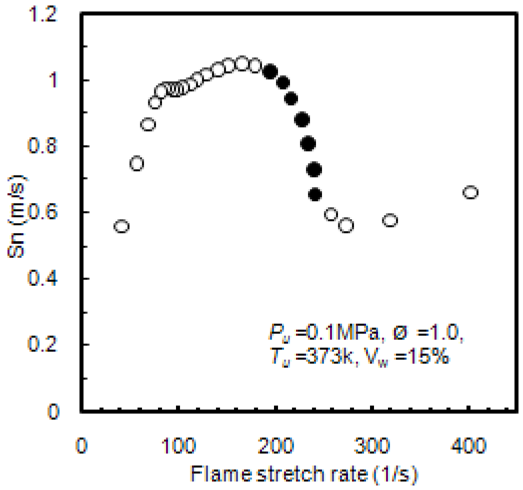

Figure 4.8 Variation of flame speed with stretch rate for an overdriven flame at Ø = 1.0, T = 373K, and water loading 15%.

Further evidence of non-linear effects witnessed in this data set, observed during the early stages of flame propagation is presented in **Figure 4.9 - Figure 4.11**. It was noticed when interrogating the data that these non-linear tendencies occurred also at low water vapour fractions, when lower ignition energies and initial temperatures of 323 K were studied. Typically this phenomena was observed at fuel rich equivalence ratios of 1.1 and 1.2, with so-called 'under-driven' flames resulting. Theoretically, if a sufficiently small ignition energy was assumed these characteristic curves pass would grow from the origin [50], though this is impossible to achieve in practice, and usually some evidence of ignition effects is present in the data (see **Figure 4.10** and **Figure 4.11**). At the time of this work, experimental data showing these characteristics was scarce, primarily due to previous studies employing insufficiently low-energy ignition systems.

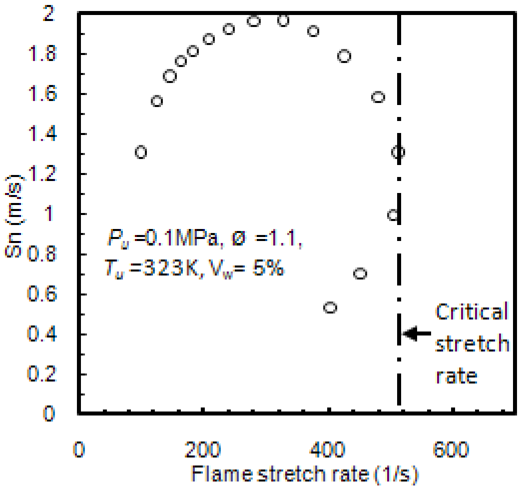

Figure 4.9 Variation of flame speed with stretch rate for 'under-driven' flame at Ø = 1.1, T = 323K, and water loading 5%.

Having attained the additional 'early stage' data for 'under-driven' flames, it was possible to observe that a maximum turning point could be derived at a stretch rate specific to the fuel and water concentration. It was postulated that this maxima may represent the stretch rate beyond which the flame is unable to exist without additional energy input i.e. point highlighted in **Figure 4.9** and also seen in **Figure 4.10** and **Figure 4.11**, henceforth referred to as the critical stretch rate (α_{Cr}). This finding gave support to what Bradley et al. [56] tentatively suggested as the point that might offer an alternative method for evaluation of extinction stretch rates (K_{ext}) to the well-established counter-flow burner method [8].

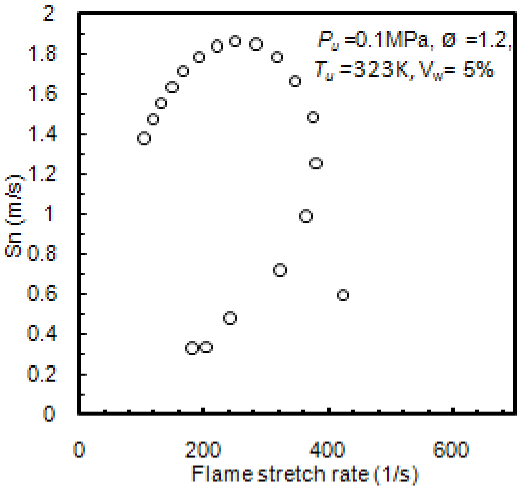

Figure 4.10 Variation of flame speed with stretch rate for ‘under-driven’ flame at Ø = 1.2, T = 323K, and water loading 5%.

A preliminary analysis of this critical stretch rate ($\boldsymbol{\alpha_{Cr}}$) from the current data-set showed this diagnostic to be consistent with established or anticipated trends of the extinction stretch rate ($\boldsymbol{K_{ext}}$), in that it reduced with increasing water vapour fraction, increased with increasing initial temperature, and peaked around or slightly rich of stoichiometry. Further studies are presented in Chapter 5 and 6 of the present thesis, to support this theory.

Assuming that there is a link between the critical and extinction stretch rates, for a methane flame with an equivalence ratio of 1.2 and initial mixture temperature of 323K, extinction stretch rates were measured as 600s^{-1} for dry mixtures, reducing to slightly less than 400s^{-1} for $\boldsymbol{V_w}$ = 5 %, and circa 300s^{-1} for $\boldsymbol{V_w}$ = 10% and 373 K. It increased again beyond 500 s-1 for the $\boldsymbol{V_w}$ =5% case when equivalence ratio was reduced to 1.1.

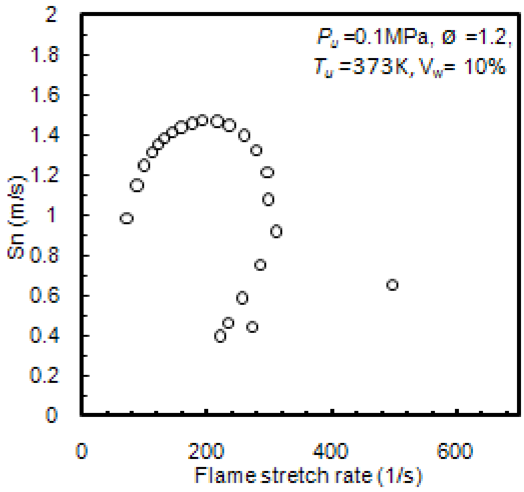

Figure 4.11 Variation of flame speed with stretch rate for 'under-driven' flame at Ø = 1.2, T = 373K, and water loading 10%.

4.5 Discussion

Through the analysis of **Figure 4.8 - Figure 4.11** it can be unveiled the strong dependence of the unsteady effect in the early stages (at small radii) of flame propagation on water vapour fraction and ignition energy. For example, in these figures non-linear trends were accentuated due to both effects, producing a heavily non-linear trend to that usually obtained at analogous dry conditions. Furthermore, to understand the nature of non-linear trajectory it is convenient to give a qualitative explanation in terms of the linear relationship between L_b and Le discussed by Bradley and Harper [130]. The cooling effect of water vapour on the flame preheat zone causes an absorption of heat resulting in a reduction of the heat diffusion from the reaction zone diminishing also the chemical reaction rate; therefore, the effect of water vapour causes a reduction of Le and, hence, L_b.

More important is the effect of ignition energy on the flame turning point referred as the critical stretch rate (α_{Cr}) in the present work – defined by Chen et al. [77] as the maximum Karlovitz number (***Ka***). According to Chen et al. [77] a change of flame thickness when a flame is initiated by the lowest ignition energy during the flame propagation before reaching the maximum ***Ka*** is the cause of the flame speed reverse and, therefore, resulting in the witnessed unsteadiness in flame trajectory. This maximum Karlovitz number ($Ka = \alpha\delta / S_L$) is expressed in terms of flame thickness (δ), stretch rate (α) and unstretched flame speed (S_L).

Moreover, Chen et al. [77] also showed that ***Ka*** decreases with increasing ***Le*** indicating that outwardly propagating spherical flames do not exist at large ***Le*** due to the quenching caused by the combined effect of flame curvature and stretch.

The strong dependence of flame trajectory on these two effects (water loading and low ignition energy) show clearly that care must be taken in the selection of the data points for determining the correct laminar flame speed and, hence, the laminar burning rate. Consequently, the selection of data range suitable for the measurement of laminar flame speed in **Figure 4.8** must be after the aforementioned turning point – avoiding over-predicted L_b and S_L values – suggesting also that this flame speed reverse should provide a potential method to obtain the K_{ext} through outwardly spherically flames, if ignited with sufficiently low ignition energies. In addition, the evolution of an unsteady flame near the adiabatic extinction limit provokes that the absolute value of L_b becomes smallest when ***Le*** is close to a critical value (***Ka*** or α_{Cr}) which is slightly less than unity [31] a phenomena which is also dependant on equivalence ratio and initial conditions.

The witnessed experimental trends and possible explanations, along with the considerations of Bradley et al. [56] thus lead the author to pursue further experimental programmes using low ignition energies to try and ascertain whether a true link between α_{Cr} and K_{ext} could be proven, which it was thought would give an alternative method to counterflow burners for the determination of extinction stretch rate.

4.6 Conclusions

- Laminar stretched methane-air-water flames were studied using high-speed Schlieren photography in a cylindrical fixed volume vessel originally designed for fuel mist studies. Particular attention had been paid to reducing the ignition energy input to initiate flame propagation, and experimental repeatability.
- On analysis of the data set it was found that sufficient data existed prior to the influence of increased pressure within the bomb to enable the study of stretched laminar flames, thus enabling the influence of water vapour on flame characteristics to be investigated. Laminar burning rate and Markstein lengths were thus determined, from limited individual data sets by combining numerous repeat points for methane/air flames at elevated temperatures in the first instance, providing benchmark data for the subsequent water-vapour studies.
- Increased ignition energies were required to develop freely propagating flames as water vapour fraction increased, with lower ignition energies resulting in flame quenching during the early stages of flame propagation, when stretch was known to be high. At initial temperatures of 323 and 373K, the laminar burning rate decreased and positive Markstein lengths increased with increased water loading to 15 % (by volume). Increased Markstein length derived for the 15 % water loading case was attributed to non-linear trends in the stretched flame speed data, consistent with recent discussion by Kelley and Law [50] provoking the requirement to set a new criteria for the selection of the suitable data range in order to conduct a valid flame speed extrapolation. These findings suggest the unsteady outwardly spherically flame transition at high water loadings and low ignition energies cause a flame speed reverse phenomenon at a critical point ($\boldsymbol{Ka}$ or $\boldsymbol{\alpha_{Cr}}$) providing an alternative method to obtain not only valid $\boldsymbol{L_b}$ and $\boldsymbol{S_L}$

values, but also K_{ext} comparable to those measured by the well-established counter-flow burner method. Further studies of this proposed method and its correlation with extinction stretch rate were thus proposed and are fully discussed in Chapters 5 and 6.

- Further analysis of the early stage 'under-driven' flame growth, enabled by the sufficiently low ignition energies employed, revealed interesting non-linear features rarely before captured, and supported and developed the suggestion of Bradley et al. [56] that 'under-driven' propagating flames provide an alternative method for evaluating extinction stretch rates to counter-flowing flame experiments. In this study, derived critical stretch rates decreased by about 50% when increasing water vapour fraction from 0-10% at $\emptyset$ =1.2, increased with reduction in equivalence ratio to stoichiometry, and increased with increasing initial temperature.

Chapter 5

“Make everything as simple as possible, but not simpler.”

Albert Einstein

Non-linear Analysis of Ethanol-Air Flames in Early Stages under Atmospheric and Raised Ambient Conditions

5.1 Chapter Overview

In order to further appraise the non-linear trends observed during the early stages flame propagation as discussed in Chapter 4, the fundamental combustion properties of ethanol-air flames were investigated in the constant volume bomb. Low ignition energies were again employed enabling the sensitive early stages of flame propagation and extinction limits to be studied. Data is presented in terms of flame speed against stretch rate from which Markstein lengths and laminar burning velocities are derived for a variety of different initial conditions. The effect of ignition energy, initial pressure along with the effect of increasing initial temperature was studied, with a focus on the investigation of the critical stretch rate observed. Results are discussed in terms of those of previous workers, and compared with predictions from detailed chemical kinetic schemes.

5.2 Introduction

This study was conducted, to further improve the understanding of the combustion of ethanol, with particular attention being given to non-linear flame propagation and the determination of a critical stretch rate (α_{Cr}) of the spherically expanding flames. It is proposed that this value may well offer a good approximation of the extinction stretch rate (K_{ext}), which there is currently a scarcity of data for in published literature. As such it is proposed that if extinction stretch rate may be derived using the outwardly-propagating spherically flame method proposed in this work for gaseous phase ethanol flames, then much required additional data concerning extinction may be readily added to the literature.

5.3 Results and Discussion

As discussed in Chapters 2 and 4 flame propagation was characterised by plotting flame front position against time, as has been employed by numerous other authors [49, 50, 76, 109, 115, 131-135] with the effect of the fuel-air equivalence ratio (**Ø**) on flame growth shown below in **Figure 5.1**.

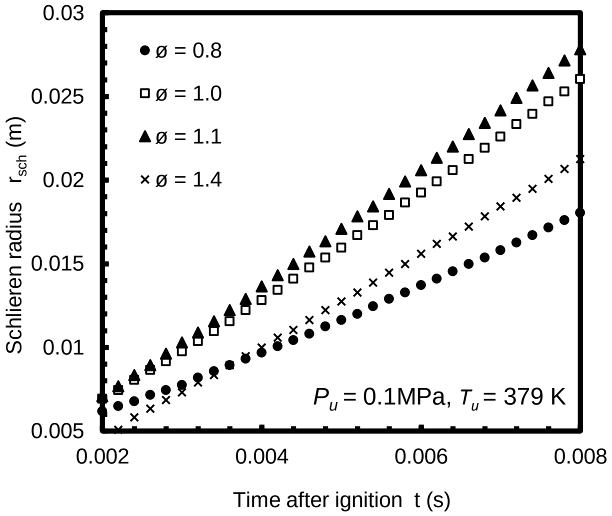

Figure 5.1 Effect of fuel-air equivalence ratio on initial flame propagation at 0.1MPa and 379K.

The increase in flame radius with time was much greater for flames near stoichiometric condition with maximum growth rates observed at slightly rich mixtures of $\boldsymbol{\emptyset}$ = 1.1 getting gradually slower towards the leanest and richest mixtures, in agreement with previous studies of ‘light’ hydrocarbon fuels [56, 136].

It is also observed in agreement with past works [36, 44, 108] that all mixtures above a minimum flame radius of 6 mm witness established flame propagation with apparently constant growth. Thus, as discussed in Chapter 3 only data taken from a flame radii above this characteristic radius was used to ensure its independence of initial ignition spark effects. However, this criteria will change in the following chapter due to the discussion given by Chen et al. [77].

As discussed earlier in Chapter 3 measured flame speeds at different stretch rates for ethanol-air mixtures using non-linear extrapolation method were derived and are presented in **Figure 5.2**. Increasing equivalence ratio towards stoichiometry brought about an increase in resultant unstretched flame speed ($\boldsymbol{S_L}$) with the maximum unstretched flame speeds observed slightly rich of stoichiometry ($\boldsymbol{\emptyset}$ = 1.1). A change in the polarity of Markstein length ($\boldsymbol{L_b}$) was also noted at $\boldsymbol{\emptyset}$ = 1.5 (further analysed in n-linear extrapolation for **Figure 5.3**), along with the characteristic turning point given by the no each equivalence ratio which will be fully analysed in **Figure 5.14**.

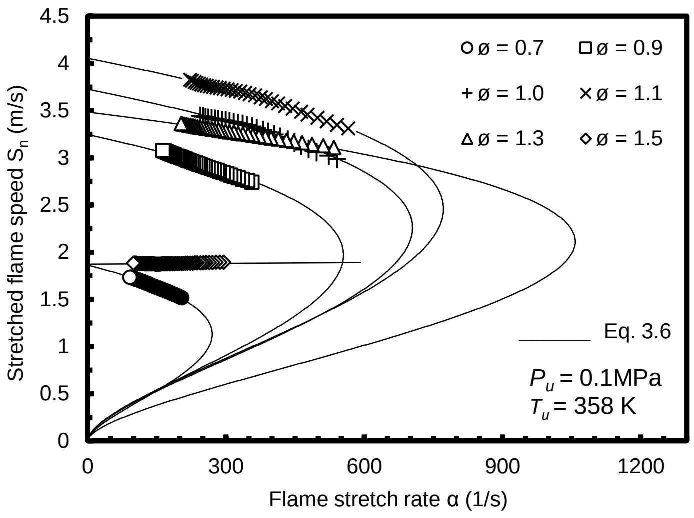

Figure 5.2 Measured flame speeds at different stretch rates at 0.1MPa and 379K.

Burned gas Markstein length (***L*_b**) data derived from the gradient of the spark unaffected region as discussed earlier in Chapter 3 is presented below in **Figure 5.3**.

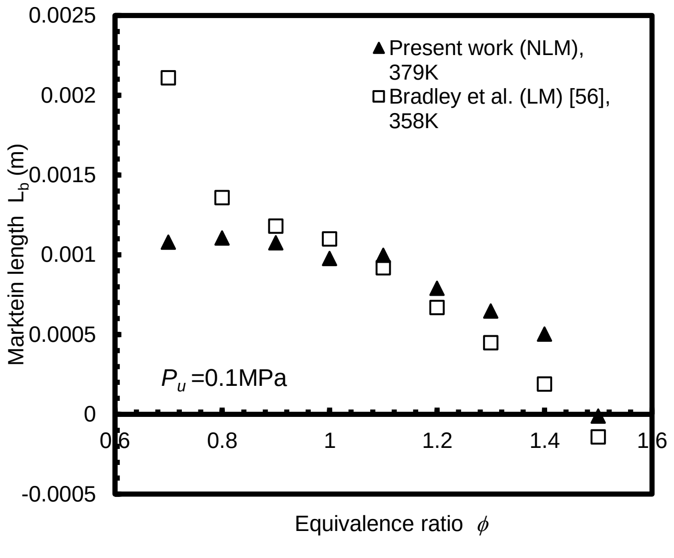

Figure 5.3 Measured Markstein lengths of ethanol-air flames as a function of fuel-air equivalence ratio at 0.1MPa. The corresponding nomenclature for LM and NLM in the present study is linear methodology and non-linear methodology, respectively.

The influence of ethanol-air equivalence ratio on the flame/stretch interaction is shown by the decreasing measured burned gas Markstein length (***L*_b**) of ethanol-air mixture decreased observed at increasing equivalence ratio, which is in agreement with other published experimental results [56, 137]. It is interesting to note that a shift in the slope direction of the richest mixture was achieved at $\boldsymbol{\emptyset}$ = 1.5, indicating that the richest flames are positively affected by flame stretch with the increase in $\boldsymbol{\emptyset}$. This is the result of the change in Lewis number ($\boldsymbol{Le}$) – defined as the ratio of thermal to mass diffusivity – provoked by the influence of $\boldsymbol{\alpha}$ on $\boldsymbol{S_n}$. In the shifted point ($\boldsymbol{\emptyset}$ = 1.5) mass diffusion was favoured over heat conduction causing a mixture in which $\boldsymbol{Le} < 1$. The $\boldsymbol{Le}$ value below unity means that less heat is losing than in that of an unstretched flame and, hence, accelerates when positively stretched, with the opposite effects observed for leaner mixtures with $\boldsymbol{Le} > 1$ [31, 138].

The laminar burning velocity ($\boldsymbol{u_L}$) derived (as discussed in Chapter 3) from the unstretched flame speed ($\boldsymbol{S_L}$) is presented over a relatively wide range of equivalence ratios below in **Figure 5.4**, with maximum burning velocities as expected being observed at equivalence ratios slightly richer than unity.

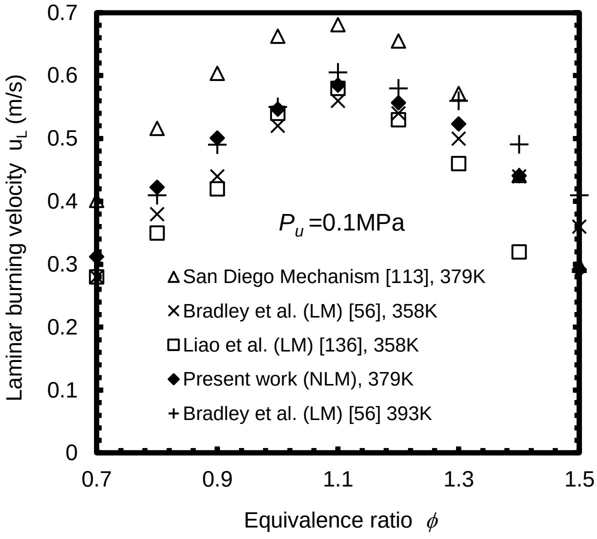

Figure 5.4 Experimental laminar burning velocities for ethanol-air flames at 0.1 MPa. The corresponding nomenclature for LM and NLM in the present study is linear methodology and non-linear methodology, respectively.

It may be seen that data from the current study lies within the expected range of other previous experimental studies, given the subtle variations in reactant temperatures employed and demonstrated the usual observed offset with results obtained via the San Diego Mechanism [113]. The maximum laminar burning velocity measured experimentally at 379K in this study was approximately 0.58m/s which as would be expected sits between the two maximum velocities quoted by Bradley et al. [56] measured at 358k and 393K of 0.56 and 0.6 m/s, respectively. However, it was lower than the modelled idealised value of 0.68m/s. It was noted that the agreement between experimental data sets reduced as the mixtures composition moves away from stoichiometry. This trend was likely caused by the increasingly nonlinear flame propagation behaviour seen in the experimental results, at equivalence ratios further from stoichiometry, a situation that occurred due to different criteria being used for the selection of data between different experimental studies coupled with the adoption of the different linear and non-linear processing approaches.

A confidence limit of 95% was chosen as a representation of the dispersion of the data, which occurred between ($\bar{x}$-2σ) and ($\bar{x}+2\sigma$), where $\boldsymbol{\sigma}$ was the standard deviation around the arithmetic mean, for the normal distribution. Thus, the data was finally presented as given by **Figure 5.5**. In this figure, a representative experimental data-set comprising four repeats together with associated error bars was presented, demonstrating a high level of repeatability.

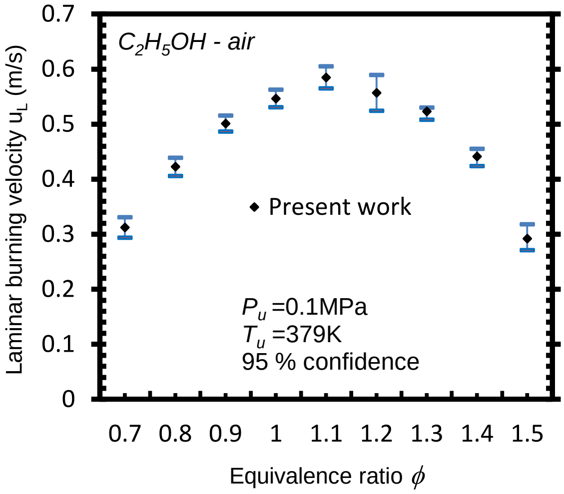

Figure 5.5 Example of laminar burning velocities with error bars indicating 95% confidence.

5.3.1 The Effect of Initial Pressure

Figure 5.6 presents a comparison of S_L at three different initial reactant pressures namely; 0.05, 0.1 and 0.15 MPa. With each mixture being composed at nominally identical fuel-air ratios and reactant temperatures (**Ø** =0.7 and 379K).

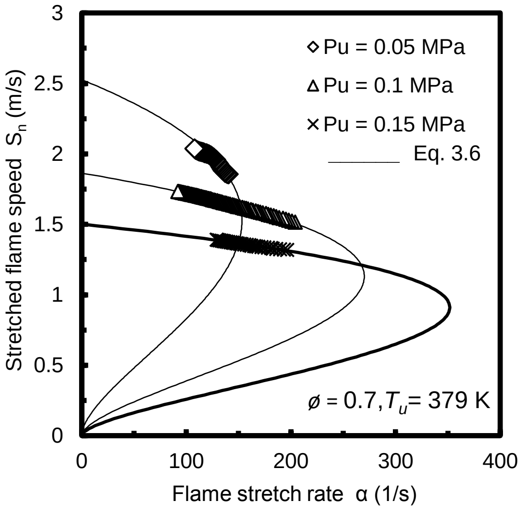

Figure 5.6 Comparison of Sn for Ø = 0.7 and 379K at different initial pressures.

It is observed in **Figure 5.6** that unstretched flame speed (***S_L***) increased with decreasing initial pressure again in agreement with earlier works [56].

The trend for Markstein length increase, with decreasing initial pressure was also observed and is presented in **Figure 5.7**. Correspondingly, the Markstein length more readily changes polarity as the ambient pressure increases. Hence negative Markstein lengths were increasingly prevalent in richer fuel mixtures at elevated pressures. A positive gradient demonstrates acceleration in flame speed with stretch rate and corresponds to a negative value of ***L_b***. This indicates that the mass diffusivity of richer mixtures becomes more dominant in proportion to reactant heat conduction giving as a result Lewis numbers less than one.

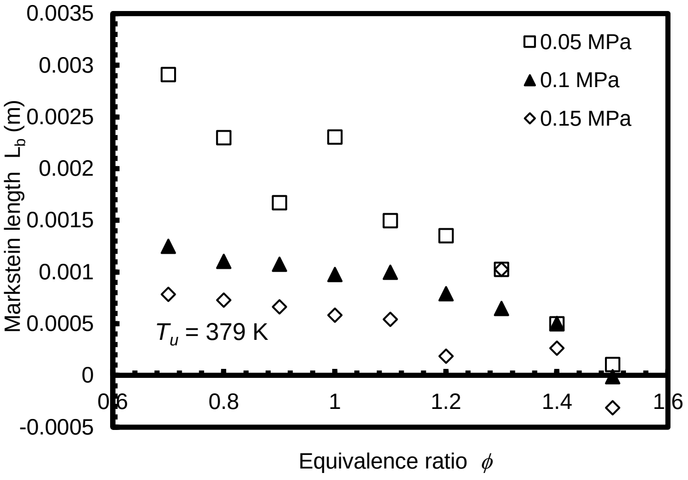

Figure 5.7 Measured Markstein lengths of ethanol-air flames as a function of fuel-air equivalence ratio at different initial pressures and 379K.

Table 5.1 and **Table 5.2** show a summary of the measured arithmetic averages of Markstein lengths (***L_b***) and laminar burning velocities (***u_L***) at different equivalence ratios (***Ø***), initial pressures and temperatures, respectively.

Table 5.1 Measured Markstein lengths as a function of fuel-air equivalence ratio at different initial pressures and temperatures.

P_u (MPa)	T_u (K)	L_b (m)								
		$\phi = 0.7$	$\phi = 0.8$	$\phi = 0.9$	$\phi = 1.0$	$\phi = 1.1$	$\phi = 1.2$	$\phi = 1.3$	$\phi = 1.4$	$\phi = 1.5$
0.05	379	0.0029	0.0023	0.0017	0.0015	0.0014	0.0013	0.001	0.0005	0.0001
0.1	372	0.0013	0.0014	0.0012	0.0011	0.0009	0.0008	0.0008	0.0	-0.003
0.1	379	0.0012	0.0011	0.001	0.0009	0.0009	0.0008	0.0006	0.0005	0
0.1	399	0.0012	0.001	0.001	0.0009	0.0008	0.0007	0.0006	0.0002	-0.0001
0.15	379	0.0008	0.0007	0.0006	0.0005	0.0005	0.0002	0.0002	-0.0005	-0.00031

Table 5.2 Measured laminar burning velocities of fuel-air equivalence ratio at different initial pressures and temperatures.

P_u (MPa)	T_u (K)	u_L (m/s)								
		$\phi = 0.7$	$\phi = 0.8$	$\phi = 0.9$	$\phi = 1.0$	$\phi = 1.1$	$\phi = 1.2$	$\phi = 1.3$	$\phi = 1.4$	$\phi = 1.5$
0.05	379	0.448	0.544	0.6	0.66	0.69	0.63	0.588	0.468	0.351
0.1	372	0.294	0.365	0.396	0.48	0.529	0.501	0.435	0.401	0.267
0.1	379	0.312	0.422	0.5	0.546	0.584	0.556	0.523	0.44	0.291
0.1	399	0.372	0.501	0.544	0.614	0.632	0.596	0.524	0.415	0.297
0.15	379	0.265	0.365	0.36	0.497	0.524	0.515	0.493	0.374	0.313

In **Figure 5.8** laminar burning (***u***u_L) are displayed over the full range of equivalence ratios (***Ø***) studied; with the maximum value of u_L attained at ***Ø*** =1.1 at the lowest initial pressure of 0.05MPa.

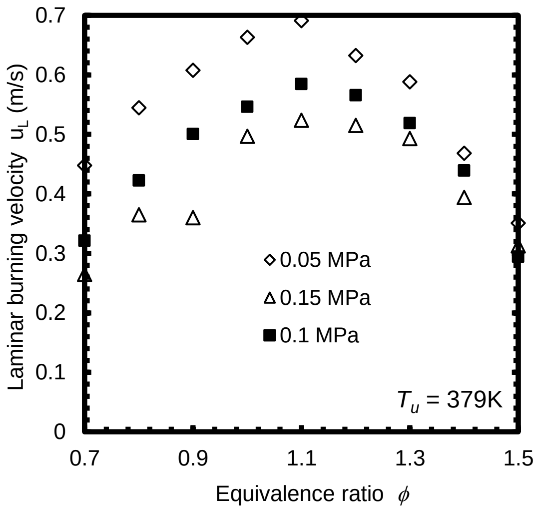

Figure 5.8 Experimental laminar burning velocities for ethanol-air flames at different pressure for 379K.

5.3.2 The effect of initial temperature

Experiments were undertaken at several initial reactant temperatures in order to obtain the effect of temperature on unstretched flame speed. The results were plotted in **Figure 5.9**.

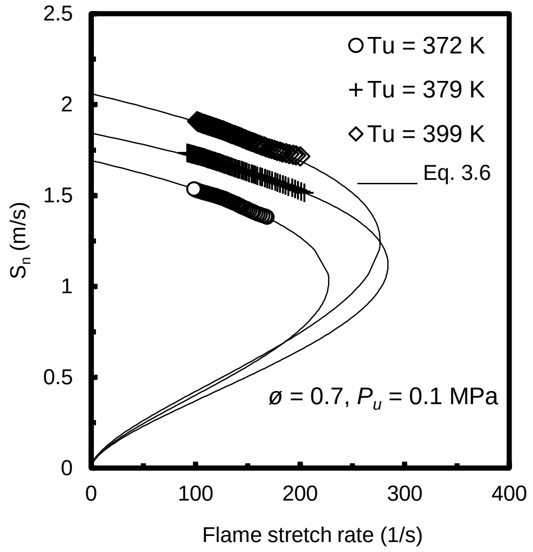

Figure 5.9 Comparison of S_n for Ø =0.7 at different initial temperatures.

Markstein lengths were shown to decrease with increase in ambient temperature in **Figure 5.10**. The change in the polarity became more likely with temperature decreased. The susceptibility to change in polarity increased with fuel richness at lower temperatures.

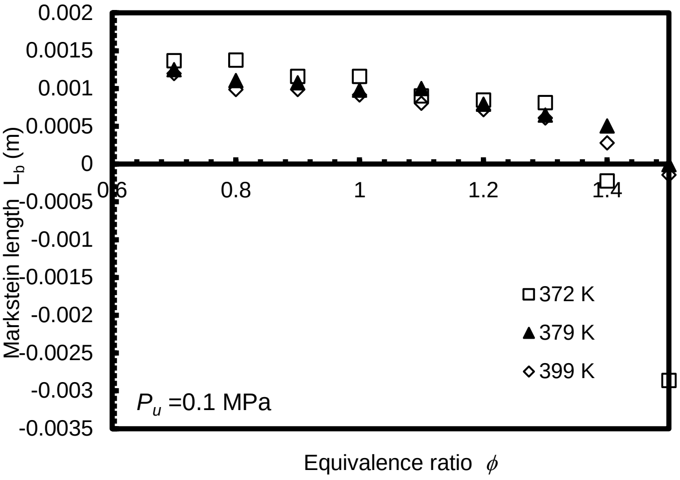

Figure 5.10 Measured Markstein lengths of ethanol-air flames as a function of fuel-air equivalence ratio at different initial temperatures and 0.1 MPa.

It can be noted in **Figure 5.11** that the unstretched flame speed (***S_L***) and the laminar burning velocity (***u_L***) increased with increasing initial temperature again in agreement with previous studies [56].

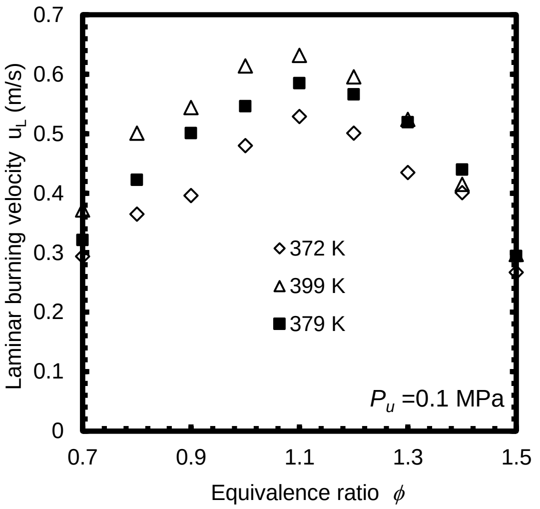

Figure 5.11 Experimental laminar burning velocities for ethanol-air flames at different temperature for 0.1MPa.

5.3.3 Critical Stretch Rates

The effect of ignition energy on early flame development and its relationship to stretch rate is now considered. Experiments were conducted at varying spark energies to assess the influence of the ignition kernel on the subsequent flame evolution at high stretch rates (small radii) for lean ethanol – air mixtures (**Ø**= 0.7), the results of which are presented in **Figure 5.12**.

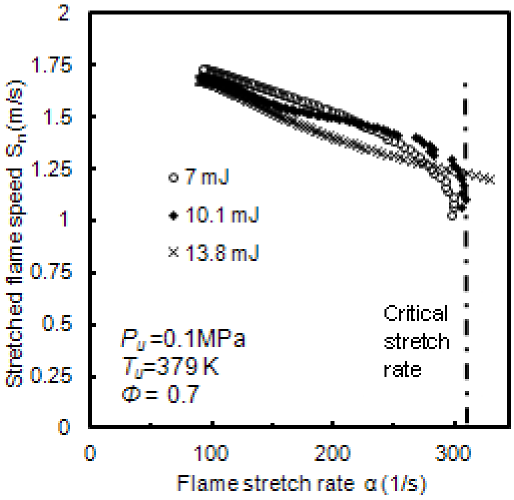

Figure 5.12 Three experiments varying ignition energies at early lean mixture flame propagation at Ø =0.7, 0.1MPa and 379K.

It is seen that three flame trajectories align as the influence of the ignition kernel was dissipated, meaning that similar unstretched flame speeds would be observed independent of ignition energy. Comparing the three cases, the low ignition energy flame increases and stabilises quicker than the high ignition energy flames. By the end of the ignition-dominated phase, a turning point appeared for the lower energy cases - the proposed 'critical stretch rate' – which was independent of the initial ignition energy if below a critical ignition energy threshold. The overdriven flame at 13mJ did not attain the critical turning point, demonstrating the crucial influence of low ignition energies for the application of this methodology. However, in Chapter 6 the Matlab script written for the analysis of the flame front was modified in order to extract the small radii at the flame early stages resulting in a more detailed study of the whole flame front propagation history and, hence, of the critical stretch rate. In the following chapter it is demonstrated that even overdriven flames attain this critical point.

In the present study this turning point is denoted as the critical stretch rate (α_{Cr}), as described earlier in Chapter 4 and represents the highest stretch rate experienced during flame growth after the effect of ignition energy has been dissipated. It is proposed that if the highest stretch rate just before the stabilization of the flame were to be higher, a normal propagating flame would not be possible [56].

Similarities between the nonlinear trajectory followed by the raw experimental data presented in **Figure 5.12** and the nonlinear extrapolation method proposed elsewhere [50], suggest that it may be possible to locate the aforementioned α_{Cr} through this low ignition energy method.

Based on the earlier discussion, by employing minimal ignition energies it was possible to directly measure this nonlinear effect, then comparisons with the data fit generated using the methods proposed elsewhere [50] could be made with data presented for a fuel-air ratio of $\emptyset$ =0.7 in **Figure 5.13**.

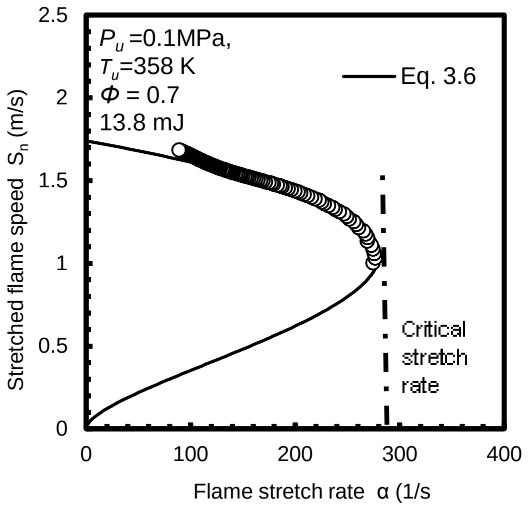

Figure 5.13 Measured critical stretch rate at low ignition energy for Ø =0.7, 0.1 MPa and 379K.

It can be seen in **Figure 5.13** where ignition effects were limited, there was good agreement in the data highlighting that a critical stretch (α_{Cr}) may be deduced as the highest observed stretch rate witnessed in the self-propagating spherically expanding flame front.

Table 5.3 presents a summary of measured critical stretched rates (α_{Cr}) at different equivalence ratios, initial pressures and temperatures, respectively.

Table 5.3 Measured critical stretch rates as a function of fuel-air equivalence ratio at different initial pressures and temperatures.

P_u (MPa)	T_u (K)	α_{Cr} (1/s)								
		$\phi = 0.7$	$\phi = 0.8$	$\phi = 0.9$	$\phi = 1.0$	$\phi = 1.1$	$\phi = 1.2$	$\phi = 1.3$	$\phi = 1.4$	$\phi = 1.5$
0.05	379	160.84	266.88	434.22	357.19	401.47	590.8	716.94	1156.12	-
0.1	372	227.45	304.51	419.17	530.08	759.39	824.57	682.11	-	-
0.1	379	304.76	432.27	561.46	713.05	764.64	892.99	1005.51	1407.77	-
0.1	399	312.61	553.74	640.63	814.63	952.73	1009.07	1042.36	1760.82	-
0.15	379	351.84	565.83	655.57	1074.39	1233.96	-	-	-	-

The early stage data affected by the ignition energy were carefully selected in order to avoid inaccurate determination of the unstretched flame speed (S_L) using the nonlinear extrapolation method.

The procedure of extracting this critical stretch rate from the analysis described above consists of locating the maximum value from the stretched flame speed (S_n) against flame stretch rate (α) tabulation calculated by the nonlinear extrapolation method. A comparison between critical stretch rates (α_{Cr}) for ethanol – air lean mixtures obtained in the present study and extinction stretch rates from other works [8, 9] is shown in **Figure 5.14**.

As can be seen the critical stretch rates (α_{Cr}) measured in this study showed similar characteristics to the extinction stretch rates derived by various authors using a counter-flow burner technique in previous studies [8, 9]. It was observed that the critical stretch rates increased with increasing equivalence ratio (**Figure 5.2** and **Figure 5.14**), they decreased with decreasing initial pressure (**Figure 5.6**), and finally they increased with increasing initial temperature (**Figure 5.9**).

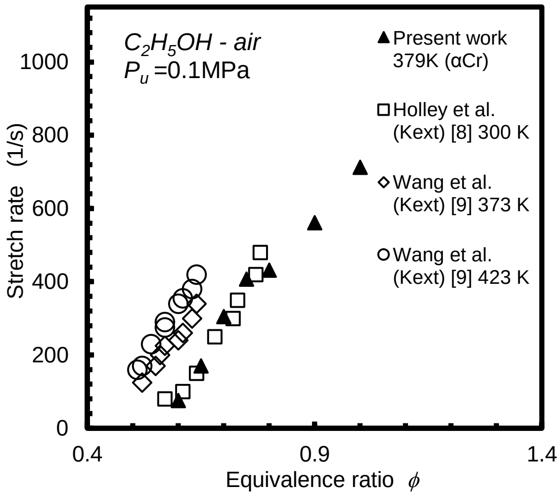

Figure 5.14 Comparison of the experimental determined critical stretch rates (α_{Cr}) with extinction stretch rates (K_{ext}) from other works for ethanol-air mixture at 0.1 MPa.

At richer equivalence ratios (**Ø** >1.4) the measured Markstein Length (L_b) observed a change in polarity, this implied that as flame stretch increased the witnessed flame speed also increased meaning that flames showing a negative Markstein length will not display a critical stretch rate (**Figure 5.2**). **Table 5.3** shows that this tendency towards negative Markstein Length at richer equivalence ratios was even more prominent at lower temperatures and elevated pressures.

Although this data set was generated using an outwardly propagating flame front, it had been demonstrated that the analysis applied in this study was capable of generating similar approximations and trends of extinction stretch rate to data produced by utilising the counter-flow burner method, which is a well-established technique for the direct measurement of extinction stretch rate. Further studies are presented in Chapter 6 to validate this statement testing to see the trends still hold for different fuels.

5.4 Conclusions

The effects of initial pressure and temperature on flame speed, Markstein length and critical stretch rate of ethanol – air mixtures were studied experimentally using high speed Schlieren photography deployed in a cylindrical constant volume combustion bomb.

It was observed that laminar burning velocity increased with increasing temperature, whilst decreased with increasing pressure. It was also observed that Markstein Length decreased with increasing equivalence ratio. At different pressures Markstein length increases as pressure decreases. Similar trend was observed for different temperatures. These findings were in agreement with both theoretical values calculated by a chemical kinetic model and with previous authors' experimental studies.

A new approach for the determination of extinction stretch rate was proposed utilising spherically expanding flames. Experiments conducted utilising 'low' ignition energies showed promise for directly measuring a proposed critical stretch rate (α_{Cr}) experimentally. Furthermore, it was also observed that the nonlinear fit proposed by

Kelley and Law [50] which was derived using data traditionally thought to be both unaffected by ignition and boundary effects might also be used to approximate this value.

This technique comprises of extracting the aforementioned maximum value of stretch located at the turning point of the non-linear plot of S_n against α (**Figure 5.12** and **Figure 5.13**). However, it should be noted that the early stage data affected by the ignition energy were carefully selected in order to avoid inaccurate determination of the unstretched flame speed using the nonlinear extrapolation method.

New experimental data, regarding stretch rate is provided (**Table 5.3**) in terms of the previous ´tentative´ suggestion of how to estimate extinction strain rates using outwardly propagating spherical flames.

By comparison to previous studies using the more established counter-flow burner technique it had been demonstrated in this study that critical stretch rate (α_{Cr}) might be representative of the extinction stretch rate with the following trends observed: increases in equivalence ratio increased the critical stretch rate, decreasing initial pressure brought about a reduction in critical stretch rate, and with increasing initial temperature the observed critical extinction limit increased.

In Chapter 6 a more detailed study is presented, to provide further evidence as to this link for not only ethanol, but an additional alcohol namely; methanol is studied. Finally to further validate this proposed methodology gaseous fuels namely; methane and propane are also tested and compared with other studies, already published in the literature. This Chapter 6 is focused on the validation of this method not exhibited in the present chapter – which is fundamental in the determination of whether spherically expanding flames can be used to provide extinction stretch rates.

Chapter 6

"I am a great believer in the simplicity of things and as you probably know I am inclined to hang on to broad & simple ideas like grim death until evidence is too strong for my tenacity."

Ernest Rutherford

Non-linear Analysis of Outwardly Propagating Flames to Determine Extinction Stretch Rate

6.1 Chapter overview

Outwardly propagating spherical flames within a constant volume combustion bomb were studied to analyse the non-linear relationship between flame stretch and flame speed, enabling a critical appraisal of an alternative methodology proposed for determining extinction stretch rate. Four fuels, namely methane, propane, methanol and ethanol in air, were chosen to investigate flame extinction across a range of equivalence ratios at various ambient conditions in under-driven flames, and to compare the hypothesis against limited published data from the traditional counter-flowing flame technique. Flame propagation was recorded via high-speed Schlieren photography, and low ignition energies are achieved via a variable capacitive-discharge supply, enabling the critical early stages of flame propagation, extinction limits and the sensitivity of the non-linear methodology to ignition energy to be systematically analysed. The non-linear methodology showed favourable agreement with extinction stretch rate from counter flowing flames, particularly in the case of gaseous fuels; the fuel vapour data lies between previous extinction stretch rate measurements using the counter-flowing flame methodology, and predictions from contemporary chemical kinetic schemes. The non-linear analytical methodology was used to extrapolate previous data from overdriven flames to predict flame extinction stretch rate, as long as a sufficient time period was disregarded to allow the effects of the early ignition-affected period to subside. Results for the four fuels reveal a common profile for extinction stretch-rate as a function of equivalence ratio, which was anticipated due to the similar fundamental combustion characteristics of the chosen fuels. Based on the non-linear analysis, it was shown analytically that this common profile may be represented by a combination of the unstretched laminar burning velocity, the Markstein length and the density ratio of the fuel.

6.2 Introduction

The aim of this work was to appraise the hypothesis conjectured in Chapters 4 and 5 that the measured critical stretch rate ($\boldsymbol{\alpha_{Cr}}$) was quantitatively equivalent to the extinction strain rate ($\boldsymbol{K_{ext}}$) as quoted in the literature for counterflow burners supporting Chen et al. [78] proposed critical radius as the radius above which an ignition kernel can lead to a successful ignition. This chapter thus presents analysis and discussion of experimental results undertaken for four fuels (two gaseous, and two pre-vaporised liquids) namely methane, propane, methanol and ethanol (CH_4, C_3H_8, CH_3OH, and C_2H_5OH), with measured values of $\boldsymbol{\alpha_{Cr}}$ benchmarked against corresponding published values of $\boldsymbol{K_{ext}}$ derived using the well characterised counter-flow technique.

As discussed earlier in Chapters 4 and 5 for a no ignition theoretical outwardly propagating spherical flame to exhibit a non-linear characteristic beyond the critical turning point, (depicted by $\boldsymbol{\alpha_{Cr}}$ **Figure 6.1**), flame propagation had to be both ignited with a low enough energy to minimise spark influence and flame thickness effect [77] on the early stage flame growth and heavily influenced by stretch. As such results were presented at conditions where these sensitive measurements were possible and the curvilinear trend was evident in the raw measured data. However in the cases where these characteristics were not dominant additional values of α_{Cr} were attained from a theoretical expression given by numerical application of the non-linear flame speed association [50] to a reduced dataset. In doing so, this potentially provided an alternative methodology for the derivation and analysis of extinction stretch rate, and explained the available database of nonlinear derived flame speed in literature, where low ignition energy had not been employed.

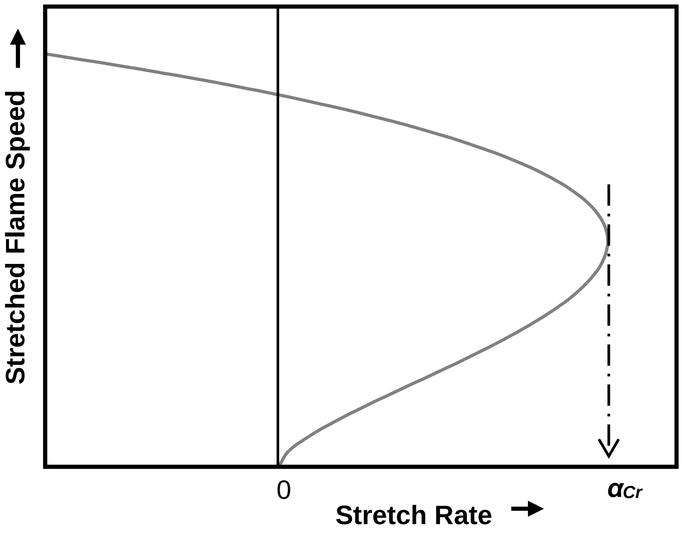

Figure 6.1 The non-linear association between stretch rate and flame speed relation to α_{Cr}

It is important to note that the effects of ignition energy and mixture ***Le*** on the flame kernel growth in an spherical flame by allowing for strongly stretched flames was investigated theoretically and experimentally by Ju and co-authors [77, 78, 139]. Their results showed that there is a critical flame radius, above which both the linear and non-linear extrapolation for flame speeds valid. Moreover, they suggested that this critical radius is the point past which a kernel can fully propagate as a successful ignition; however, no comparisons of the corresponding stretch rate value against extinction stretch rates were reported.

6.3 Results

As discussed previously a benchmarking study of the experimental system employed for this study had been undertaken previously [103], employing CH_4 in air to validate the performance and repeatability of the experimental methodology and subsequent data processing techniques. Here four fuels, already characterised in the literature were utilised to appraise the hypothesis of this study namely, a correlation between α_{Cr} and K_{ext}.

6.3.1 Laminar Burning Rate u_L and Markstein Length L_b

The fuel/air mixtures were characterised over a range of equivalence ratios whereby exaggerated nonlinear flame propagation were observed, corresponding to comparative data of critical stretch rates found within the literature. The values of u_L and L_b derived for the four aforementioned test case fuels characterised for this present study are presented in **Figure 6.2** and **Figure 6.3**, respectively. As can be seen datasets obtained by numerous other authors, utilising a range of experimental techniques and chemical kinetic simulations, are also presented thus allowing meaningful comparisons of results to be made.

All results from the present work were obtained using the non-linear methodology (**Eqn. 3.6**) and were in favourable agreement with previous studies. It is important to note that the selection of comparative data relied on the availability of the results that were found in literature. Laminar burning velocities of methane/air exhibited similar trends to the data presented by Varea et al. [45] and Halter et al. [51], who both employed a non-linear methodology, as well as Bradley et al. [44] who used the linear methodology and finally results modelled using the GRI-Mech [112] reaction mechanism. Data from Gu et al. [46], where the linear methodology was utilised, was limited up to equivalence ratio of 1.2. The counter-flow configuration used by Veloo et al. [75] for propane/air experiments also showed good agreement with the present work, together with the lower-temperature data derived by Chenglong et al. [140] using the linear methodology. For methanol/air flames there was good agreement between the present work and data presented by Holley et al. [8] derived using the counter-flow configuration, together with previous model predictions [113]. Finally experimental ethanol/air mixtures demonstrated good agreement for u_L when compared with data obtained by Bradley et al. [56], who used the linear methodology, and Holley et al. [8] who used the counter-flow configuration.

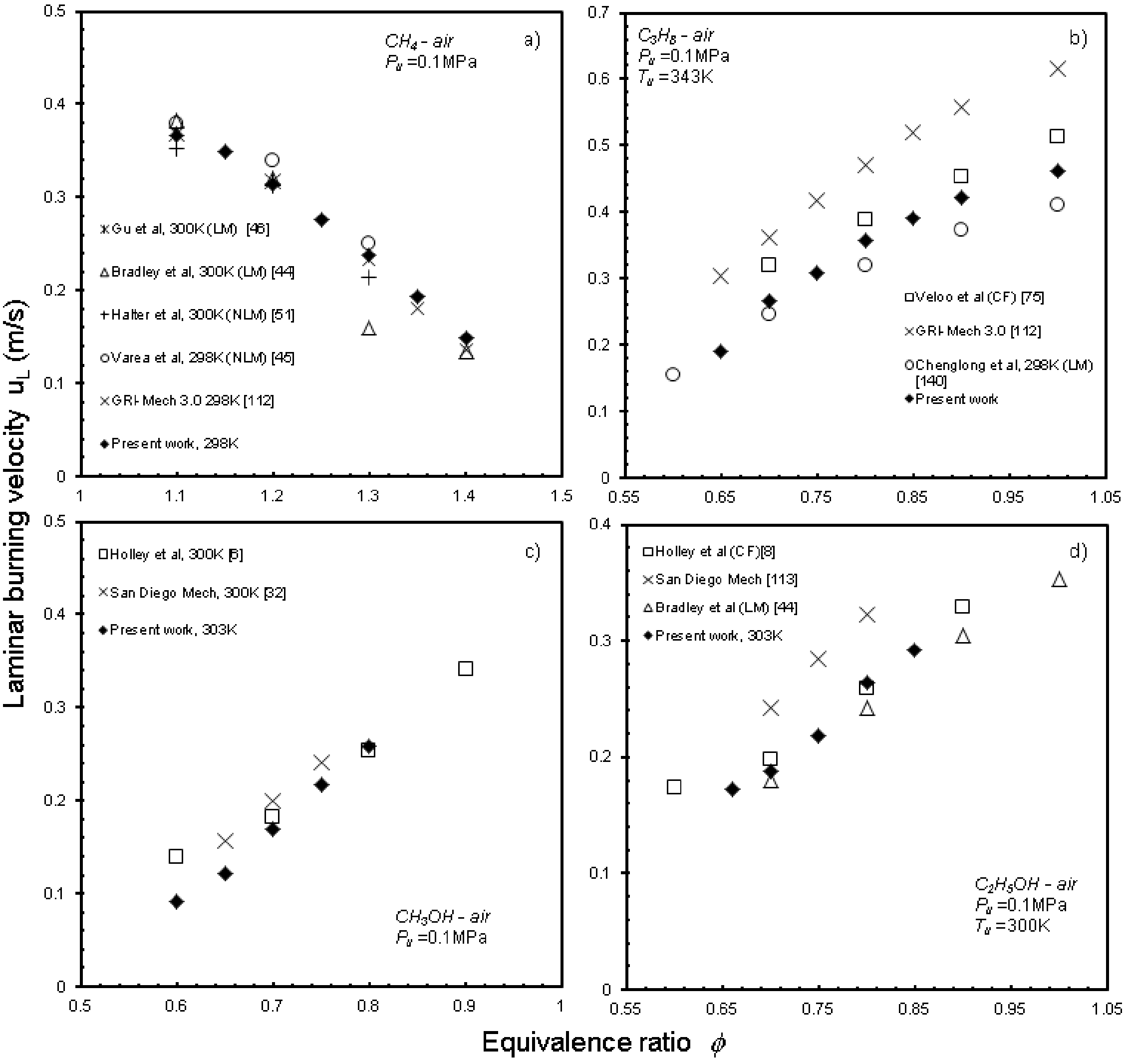

Figure 6.2 Measured Laminar Burning Velocity in the region of nonlinear propagation for a) methane, b) propane, c) methanol and d) ethanol respectively. Reactant pressure 0.1MPa, temperatures highlighted on plots. The corresponding nomenclature for LM, NLM and CF in the present study is linear methodology, non-linear methodology and counter-flow configuration, respectively.

Markstein lengths from the current dataset compare favourably with those obtained from analogous non-linear techniques; however there is an offset compared with the linearly derived data as anticipated, consistent with results from other recent studies [51], and with those with an anticipated offset resulting from an elevation in temperature [45, 115, 136, 140].

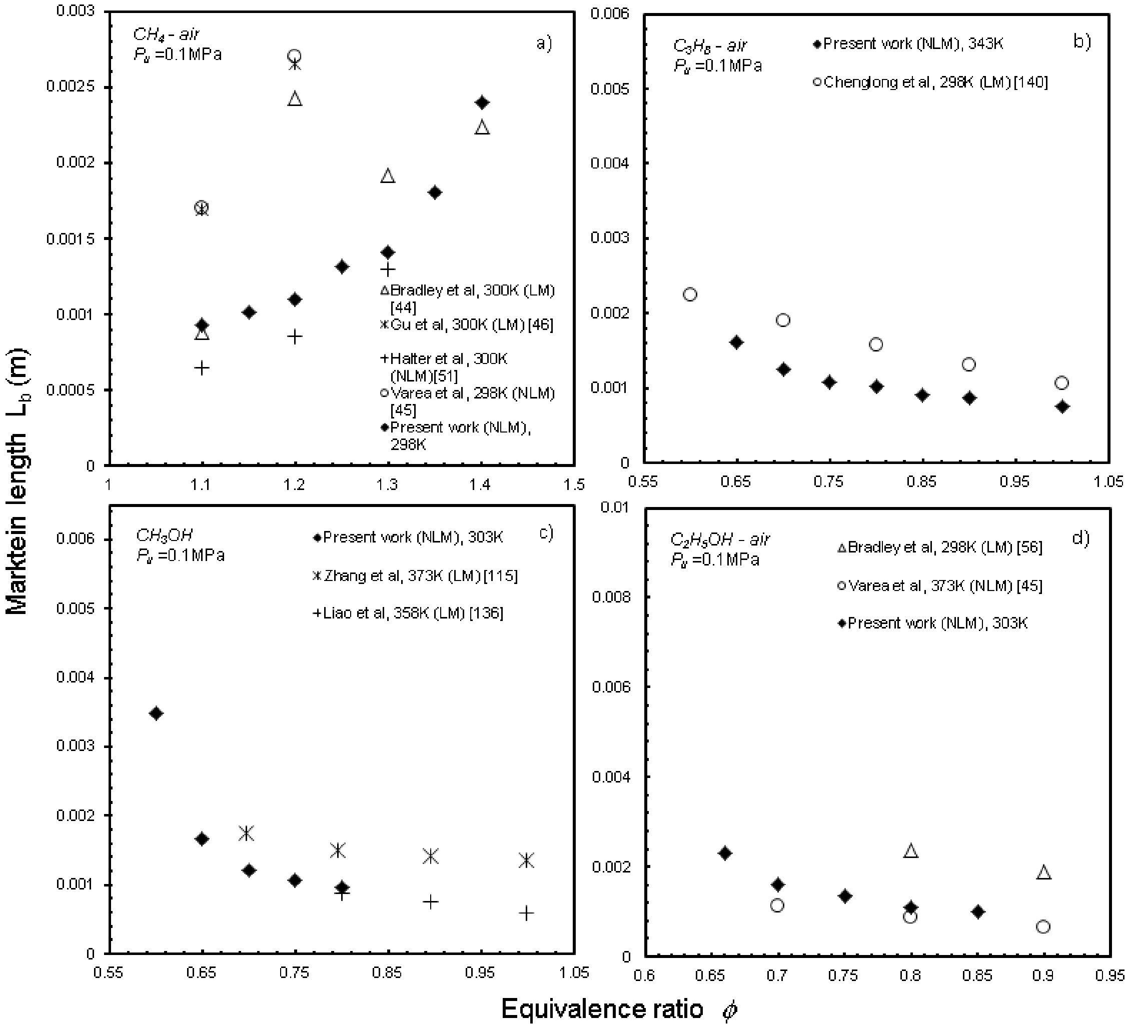

Figure 6.3 Measured Markstein Lengths in the region where nonlinear propagation for a) methane, b) propane, c) methanol and d) ethanol respectively. Reactant pressure 0.1MPa, temperatures highlighted on plots. The corresponding nomenclature for LM and NLM in the present study is linear methodology and non-linear methodology, respectively.

6.3.2 Critical stretch rate (a_{Cr})

The effect of ignition energy on early flame development and the relationship with stretch rate are now considered in detail. Experiments were conducted employing a range of spark energies to assess the influence on subsequent flame evolution at high stretch rates (small radii), as discussed in section 3.1.

Figure 6.4 and **Figure 6.5** show the influence of ignition energy on the early stages of flame propagation. Lean ethanol mixtures were used to demonstrate the observed trends, as ethanol requires relatively higher ignition energy to initiate combustion with the corresponding propagation more influenced by stretch. It is seen in **Figure 6.4** that an initial linear trend is observed in the region of highest stretch-rate (lower right in plots) which is an ignition effect, as has been discussed by previous authors [44, 78] and was thus removed from the derivation of critical stretch rate by taking adopting a minimum radius of 10 mm for which data is valid for the required data fit.

As can be seen in the case of the ultra-lean ethanol flame (**Figure 6.4**) by reducing the ignition energy too low (13.8 mJ) a non self-propagating flame kernel that did not provide sufficient heat release in relation to the diffusion resulted, causing a marginally lower flame speed in relation to stretch rate, and hence flame extinguishment, before the first turning point could be achieved. All higher ignition energies provided approximately the same conditions for displaying a self-sustaining ultra-lean flame demonstrating the effect of ignition energy on flame trajectory presented in **Figure 6.5**. According to Chen et al. [77] this flame reverse is provoked by the substantial flame thickening of the flame initiated by the lowest ignition energy before it reaches the maximum Karlovitz number (***Ka***).

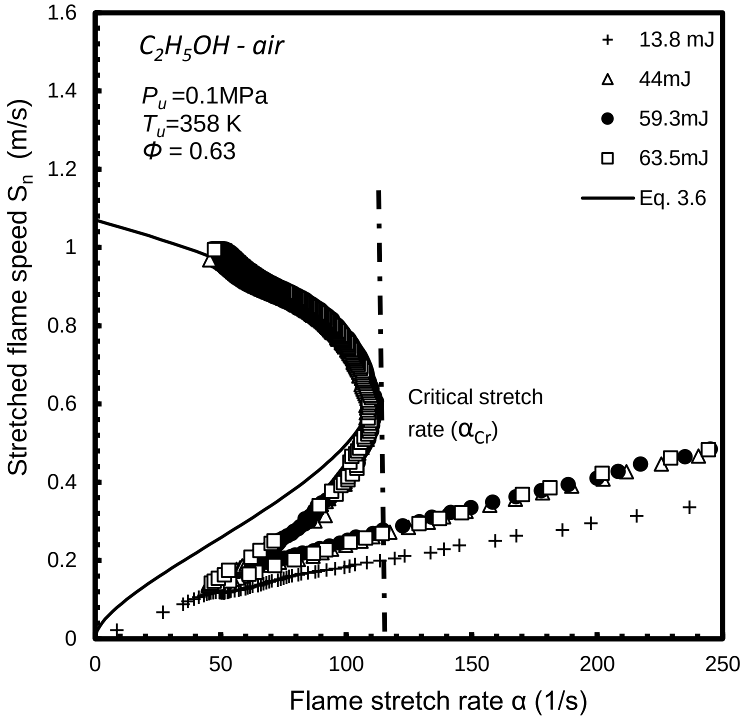

Figure 6.4 Lean ethanol flame propagation at φ = 0.63, 0.1MPa and 358K, with change in ignition energy.

In **Figure 6.5**, data is presented for ethanol-air at an increased equivalence ratio of 0.75 and a reduced initial temperature of 303K, this combination allowed a lowering of the minimum ignition energy, for self-propagating flames due to an increase in the flame temperature and heat release. Decreasing the ignition energy induced a clear change in the development of the stretched flame; however, it was observed that there was little difference in the fitted non-linear extrapolation equation if the aforementioned minimum 10 mm radius was applied for the relevant measurement points.

It is clearly observed that the overdriven flames witnessed at ignition energies of 10 and 86 mJ disguised the critical turning point in the plot, as has been observed by other authors [50, 108] emphasising the critical influence of low ignition energies in the application of this experimental methodology. Hence, in these cases where significant over driving of the flame are witnessed it was necessary to apply data-fitting and extrapolation to approximate α_{Cr}. In the case of further increased equivalence ratio even very low ignition energies overdrive the flame past this point, hence direct measurement of α_{Cr} is no longer viable meaning the extrapolation method must be adopted.

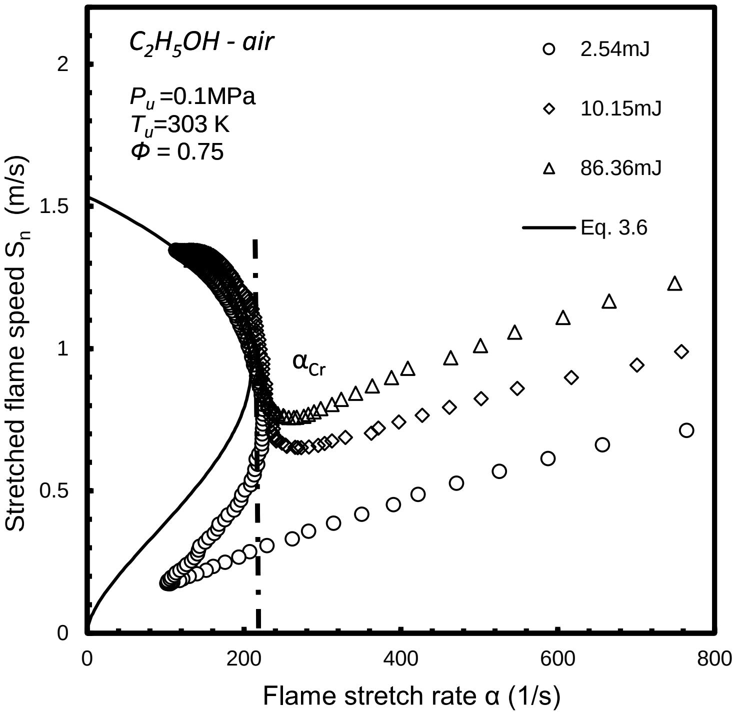

Figure 6.5 Lean ethanol flame propagation at φ = 0.75, 0.1MPa and 303K, with change in ignition energy.

To support the supposition that the extrapolation method is able to accurately predict the critical stretch limit that would have been derived through experimental measurement further data is presented in **Figure 6.6**. As can be seen a comparison between the critical point derived by extrapolation, using the non-linear equation utilising only valid data points measured at flame radii of between 10-38mm, to that measured experimentally utilising a low ignition energy are presented.

As can be seen little difference in α_{Cr} derived from either approach (three repeats averaging 5.7% difference), is observed thus strengthening the argument that a good approximation of α_{Cr} may be obtained by extrapolation of data from the upper part of the curve (radii 10-38mm) even when the critical point could not be directly measured due to the increased ignition energy which brought about an overdriven flame during the early stages of flame propagation. This also indicates that this technique, developed for the derivation of burning rate and Markstein Length may also be applied effectively to non-linear flame speed data generated previously using higher ignition energies, to predict α_{Cr} even though the data could not be used to directly measure it.

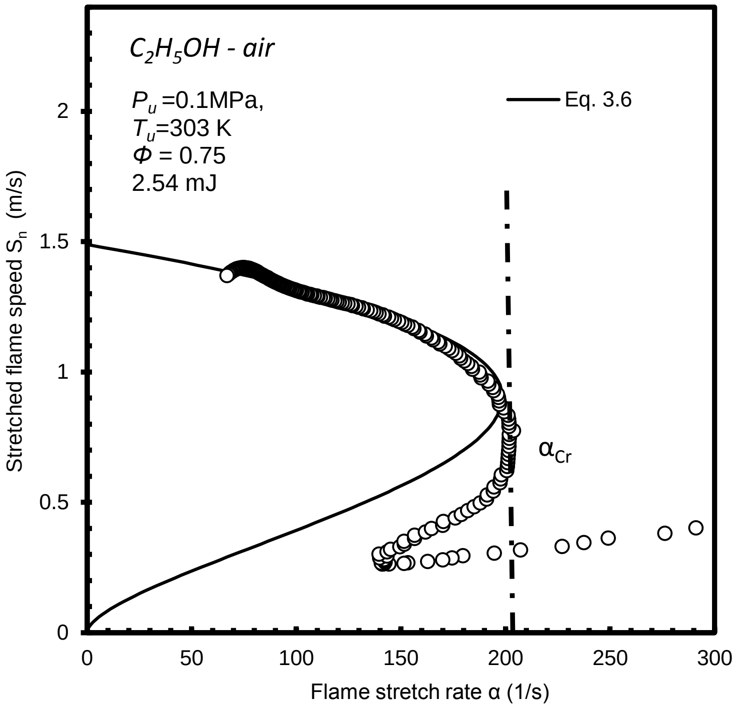

Figure 6.6. Measured critical stretch rate at low ignition energy for ethanol, φ = 0.75, 0.1 MPa and 303 K

To further support the proposed hypothesis of this chapter the following sections provide comparisons between the empirical α_{Cr} values obtained in this study for the different fuels at a range of different equivalence ratios, perceived to exasperate the effects of flame stretch and corresponding published K_{ext} values from counter-flowing flames using the counter-flowing flame methodology. Data points from the measured flame trajectory were used to present the measured α_{Cr} values if possible, however in the case of mixtures that had to be slightly overdriven, to achieve repeatable combustion then the value extrapolated from the non-linear extrapolation equation was presented, with the difference between measured and extrapolated data identified on each graph.

6.3.2.1 Methane/air

A comparison between values of α_{Cr} calculated in the present work, and K_{ext} from Egolfopoulos et al. [70] and Park et al. [74] is shown in **Figure 6.7** and **Figure 6.8** for rich and lean mixtures, respectively. In their respective works the authors utilised a single-flame configuration, which was preferred to the symmetric twin flame which was susceptible to instabilities, affecting both topology and response.

Complete non-linear flame trajectories were observed for Ø = 1.3 – 1.4 only in this study, and so the non-linear extrapolation equation was used to provide all further values as presented by white diamonds in **Figure 6.7** and **Figure 6.8.** Egolfopoulos et al [70] found qualitative and quantitative differences between the results obtained with and without heat loss; and they noted that adiabatic experimental results must be used with caution when interpreting realistic situations with heat loss. As can be seen in **Figure 6.7** there was good agreement in the extinction stretch rate characteristics proposed by both methodologies for rich flames with a strongly correlating trend with both the measured and extrapolated data, however it is noted that there is a larger variance near the peak burning velocity around ***Ø*** = 1.1.

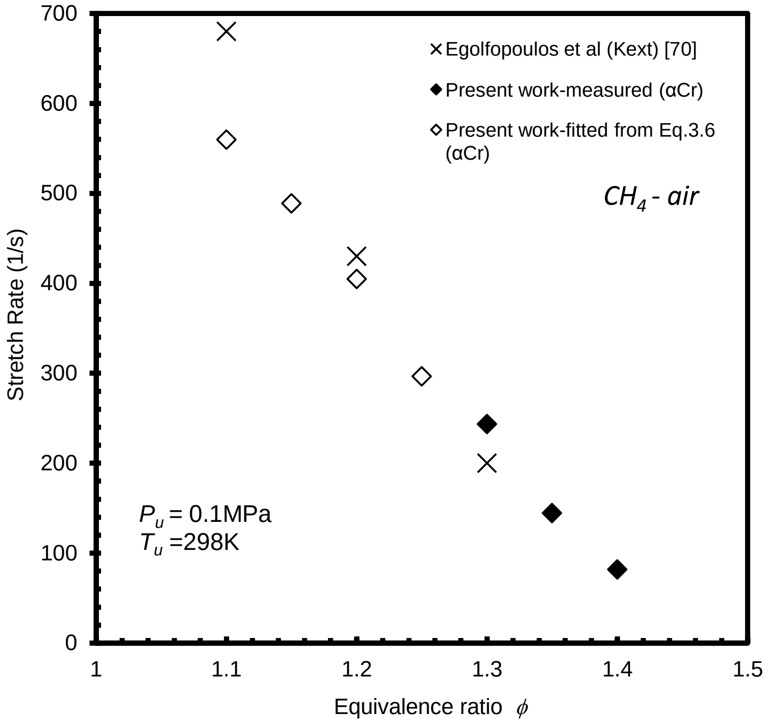

Figure 6.7. Comparison of experimental αCr against Kext for rich CH4/air mixtures at 0.1 MPa and 298 K.

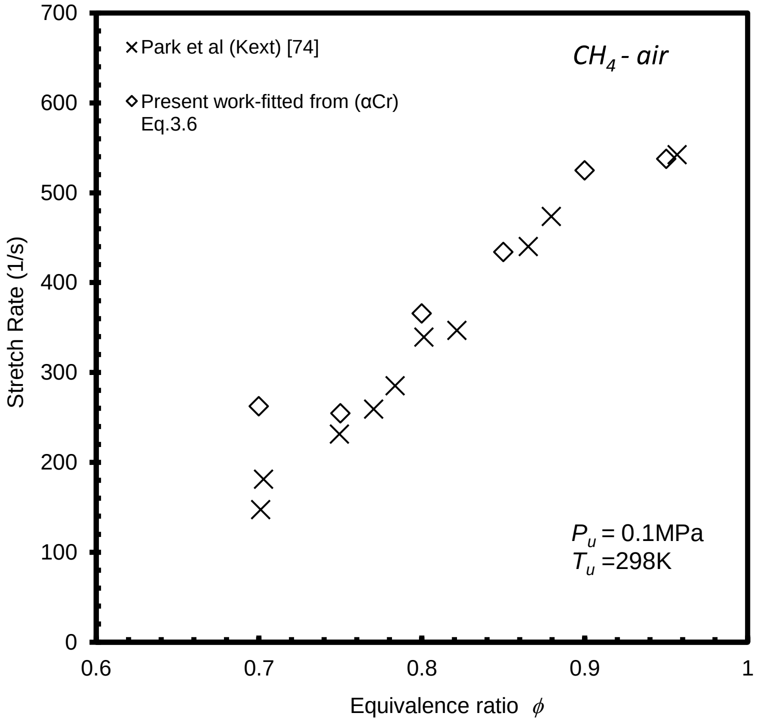

Figure 6.8. Comparison of experimental αCr against Kext for lean CH4/air mixtures at 0.1 MPa and 298 K

6.3.2.2 Propane/air

Lean propane/air mixtures, $\boldsymbol{\alpha_{Cr}}$ examined in this present work are compared to those obtained to values of $\boldsymbol{K_{ext}}$ taken from the results from Veloo et al. [75] in **Figure 6.9**. As can be seen for **Ø** = 0.65 – 0.75 full non-linear flame trajectories were observed and values of $\boldsymbol{\alpha_{Cr}}$ could be measured directly. For Ø = 0.8 – 1, flames were readily overdriven, requiring $\boldsymbol{\alpha_{Cr}}$ values to be derived using the non-linear extrapolation equation.

It is observed that the measured values of $\boldsymbol{\alpha_{Cr}}$ increased with equivalence ratio, following the same trends exhibited by the data presented by Veloo et al. [75]. As for the methane/air data, propane/air systems exhibited good agreement with those obtained using counterflow burners. Hence, for the two lower chain gaseous hydrocarbon fuels tested, $\boldsymbol{\alpha_{Cr}}$ provided a good approximation of $\boldsymbol{K_{ext}}$.

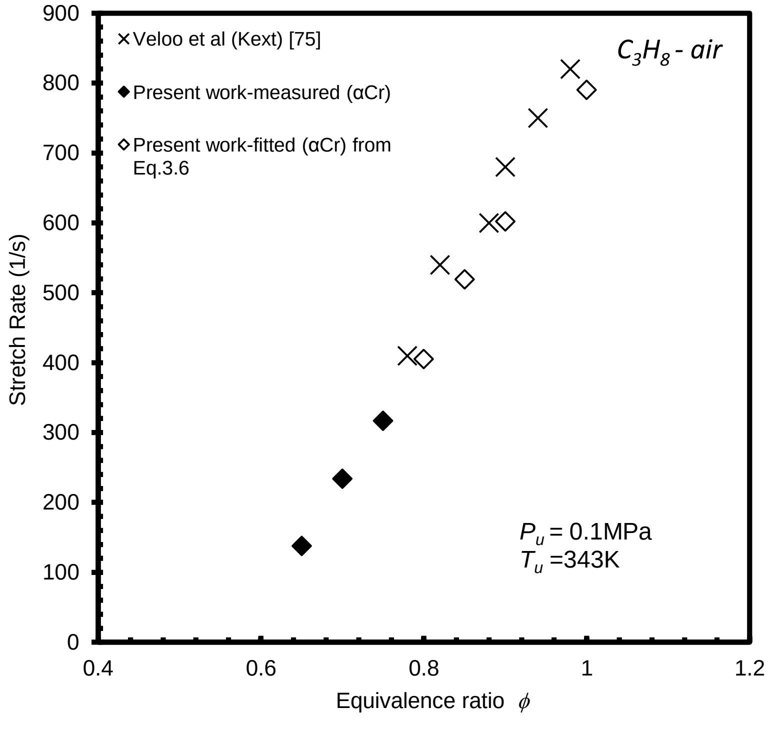

Figure 6.9. Comparison of experimental αCr against Kext for C3H8/air mixtures at 0.1 MPa and 343 K.

6.3.2.3 Methanol-air flames

Now the hypothesis of the present work is applied to the fuel vapour of two alcohols currently being proposed as sustainable energy alternatives to conventional fuel blends namely Methanol and Ethanol.

Figure 6.10 shows the comparison between α_{Cr} obtained from the present work and K_{ext} from Holley et al. [8] for lean methanol/air mixtures.

Results obtained in the present study showed an offset from the Holley et al experimentally derived counter-flow data [8], although both datasets demonstrate a similar trend in terms of change in stretch rate with equivalence ratio. One explanation for this offset could be inaccuracies in equivalence ratio which are notoriously harder to control in the case of liquid vapours compared with pure gaseous fuels, due to issues with complete evaporation and potential ‘dewing’ out of liquid fuels on any surfaces that are cooler than the saturation temperature of the vapour in question.

Furthermore, the experimental results derived in this study are closer to the trend lines predicted by published chemical kinetic schemes HD98, LDH03, and FDC00 as presented by Holley et al. As can be seen again full non-linear flame trajectories were only obtained over a limited range of equivalence ratio’s namely; between **Ø** = 0.6 – 0.65 only.

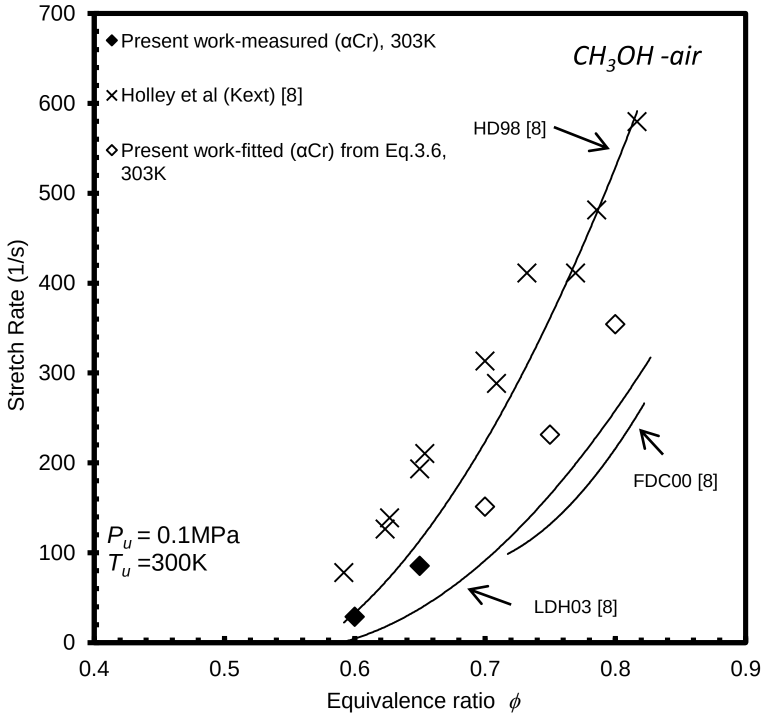

Figure 6.10. Comparison of experimental αCr against Kext for CH3OH/air mixtures at 0.1 MPa and 300 K.

6.3.2.4 Ethanol-air flames

Again present data for ethanol/air mixtures were compared against data from the literature presented by Holley et al. [8] and is given graphically in **Figure 6.11.**

As in the case of methanol, values of K_{ext} obtained for ethanol/air mixtures increased as the mixture became richer, and again the data presented here was lower than the comparable data presented by Holley et al. [8], with again a similar offset of approximately 0.5 in equivalence ratio.

Strangely the benchmarked values of laminar burning velocity derived from each experimental dataset as presented in **Figure 6.2** were very similar, indicating that both the mixture concentrations were correctly formulated and calculated, however as shown previously in the case of Markstein Length subtle changes which do not drastically effect burning rate can have a bigger influence on other characteristics.

Encouragingly, the gradients plotted between both alcohol datasets were for both cases similar, with, the current data comparing at least as or in some cases more favourably to the predictions from contemporary kinetic schemes FDC00 and MRN99.

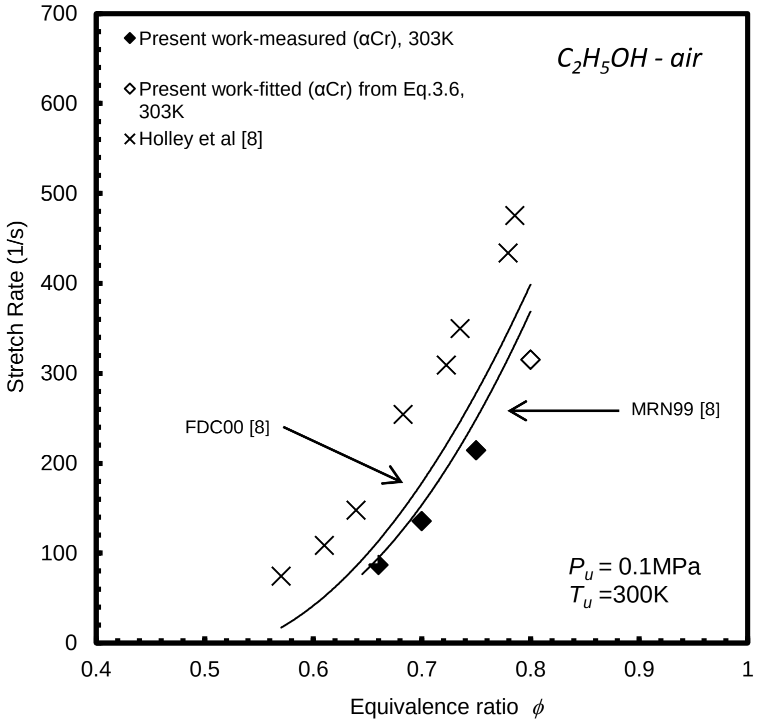

Figure 6.11. Comparison of experimental αCr against Kext for C2H5OH/air mixtures at 0.1 MPa and 300 K.

6.4 Discussion

The basic premise employed in this study concerned achieving minimal ignition energies, to reveal the sensitive early stages of flame front propagation, enabling the measurement or extrapolation of the critical stretch rate so that it could be compared with the values of extinction strain rate quoted in the literature. **Figure 6.12a** exemplifies the relationship between the Schlieren flame front radius (**r_{sch}**) and time, for the case of a weakly ignited lean ethanol/air mixture. In **Figure 6.12b** propagation of a typical stretched flame is shown for the same dataset, revealing the non-linear flame speed characteristic.

As can be seen the development of the flame may be subdivided into three distinct regions (a, b and c) which allows for further discussion.

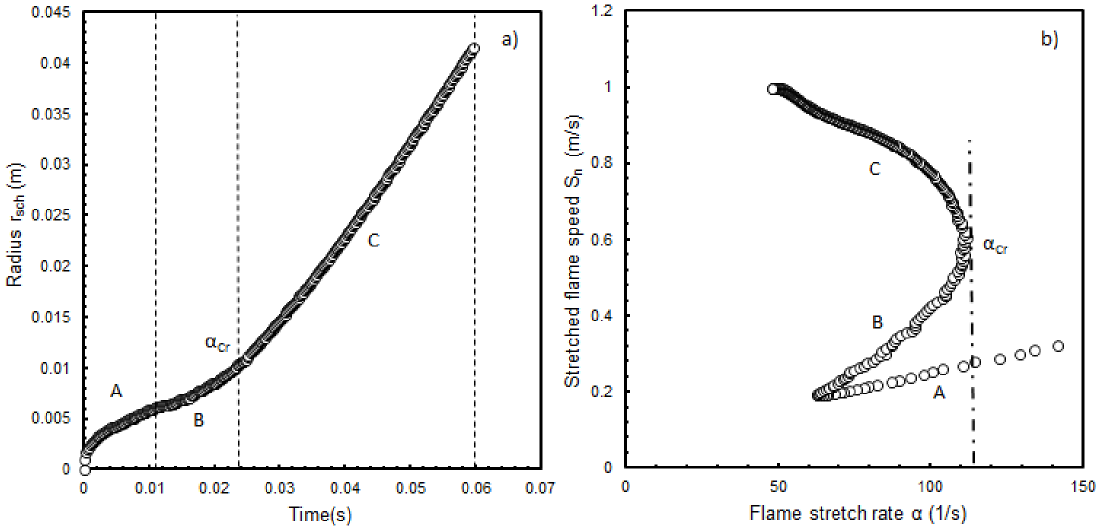

Figure 6.12. a) Relation between time after ignition and the Schlieren flame front radius (rsch) and b) Flame propagation trajectory at low ignition energy for ethanol.

It can be seen that in region A (**Figure 6.12a**) a rapid growth in flame radius is observed induced by conductive plasma transfer from the spark energy release, this acceleration in time slowed after the initial expansion. Within region B the influence of ignition dissipated, resulting in a change from the deceleration and potential for quenching originally observed in region A. These early stages of natural flame-kernel growth eventually reached the transition point $\boldsymbol{\alpha_{Cr}}$ after which the flame front started again to accelerate until it propagated in the traditional quasi-linear regime as depicted by region C. As such it may be postulated that the behaviour in region A is governed by the initial energy and heat released from the spark, whereas region B allowed the flame kernel to propagate under its natural non-linear rate of reaction which is heavily influenced by the effect of stretch, with gradually less influence from the spark discharge, finally resulting in a spark and stretch unaffected period of flame propagation until such a time that wall/pressure effects again affect the propagation rate.

As such in terms of stretch rate region A in **Figure 6.12b** represents the spark driven zone, where the flame decelerated with increasing radius, hence both S_n and α were observed to decrease, in accordance with both deceleration and radius increase. The tendency for decreasing speed with stretch rate in this zone suggested Lewis numbers (Le) of less than unity, and dominant reactant mass diffusivity. This was understandable given the small, highly stretched flame kernel, surrounded by cold unburned reactant. Heat release from the spark must thus be sufficient to raise the thermal conduction in proportion to reactant mass diffusion, and generate enough heat to enable the flame to become self-propagating. Taking this to the limit, region A would not exist, with flame growth starting at the origin as determined by the non-linear extrapolation equation (**Figure 6.5** - **Figure 6.7**), though in practice this limit could never be realised. These observations support the conclusions of Kim et al. [78] with reduced excess enthalpy from the spark ignition energy, prior to the first turning point. If the critical value of ignition energy is not high enough the ignition kernel will extinguish.

Whilst attaining enough relative heat release to propagate, the flame kernel was initially small, and therefore reactant mass diffusion was still a dominant influence as the flame started to accelerate. Hence, stretch rate rose with an increase in the velocity of propagation, as is observed in region B. The flame eventually reached a point where heat release and thermal conduction were in balance with the diffusivity of reactants entering the flame front. This point of apparent equi-diffusivity resulted in the critical turning point, denoted here as α_{Cr}, beyond which point the flame began to accelerate with decreasing stretch. This explanation was supported by the work of Wu et al. [141] who observed that extinction stretch rate K_{ext} decreased exponentially with Le. Wu concluded that strong spherical flames were observed in the region where Le was small, thus it was more difficult to extinguish the flame. This was also supported by the trends exhibited in **Figure 6.5** when the flame was overdriven, and ignition energy was increased enabling the flame to exist beyond the critical point. The increased energy provided greater heat release in relation to mass diffusion, and hence the influential region B was lost. The same mechanism that controls flame extinction in the counter-flow technique through Le, was interpreted similarly by Law [31]. Again these observations support Kim et al. [78] conclusions about the self-sustained nature of the flame without assistance from the spark. However, the flame is relatively cold and strongly stretched due to broadening of the reaction-diffusion zone, decreasing fuel diffusion to the reaction zone.

Finally, in region C the traditional stretched flame propagation was identified, with greater heat release to the surrounding reactants lowering flame temperature and speed. This effect diminished as curvature and stretch rate were reduced, and the flame front tended towards the planar limit, with flame speed correspondingly rising toward its unstretched limit. Hence it follows that the methodology presented can only be applied to self-sustaining stable reaction zones where $Le > 1$.

The data presented showed a clear correspondence between K_{ext} and α_{Cr}, qualitatively and quantitatively.

Finally, it is informative to reconsider the evaluation of α_{Cr} presented in **Figure 6.12b** and embedded within the non-linear extrapolation equation in light of the current dataset and proposed methodology. First, **Eqn. 6.1** presents $\alpha(S_n)$ as a function of S_n. Now α_{Cr}, defined as the critical turning point of $\alpha(S_n)$, may be determined explicitly via basic calculus (**Eqns. 6.2** and **6.3**). Hence, subject to assumptions inherent in the non-linear extrapolation equation **Eqn. 6.3** shows the critical (extinction) stretch rate to be a function of laminar burning rate, density ratio and Markstein length.

Given the similar combustion characteristics presented in **Figure 6.2** and **Figure 6.3** for the fuels chosen in this study, **Eq. 6.3** predicts that the critical stretch rates should also be quantitatively similar for these fuels under the ambient conditions considered.

$$\alpha(S_n) = -\frac{S_L}{2L_b}\left(\frac{S_n^2}{S_L^2}\right)\ln\left(\frac{S_n^2}{S_L^2}\right) \tag{6.1}$$

$$\frac{d\alpha}{dS_n} = -\frac{S_n}{S_L L_b}\ln\left(\frac{S_n^2}{S_L^2}\right) - \frac{S_n}{S_L L_b} = 0 \tag{6.2}$$

$$\alpha_{Cr} = \frac{u_L}{2eL_b}\left(\frac{\rho_u}{\rho_b}\right) \tag{6.3}$$

The extinction stretch rates for CH_4, CH_3OH, and C_2H_5OH, derived in the present work were plotted together in **Figure 6.13** as function of equivalence ratio. C_3H_8 mixtures were not presented due to the difference in initial temperature. Again the filled symbols represent data where non-linear $\boldsymbol{K_{ext}}$ flame trajectory was measured, and unfilled symbols were derived from extrapolation. CH_4 covered a broader range of equivalence ratios, as the full non-linear trajectory was also attainable for all three fuels.

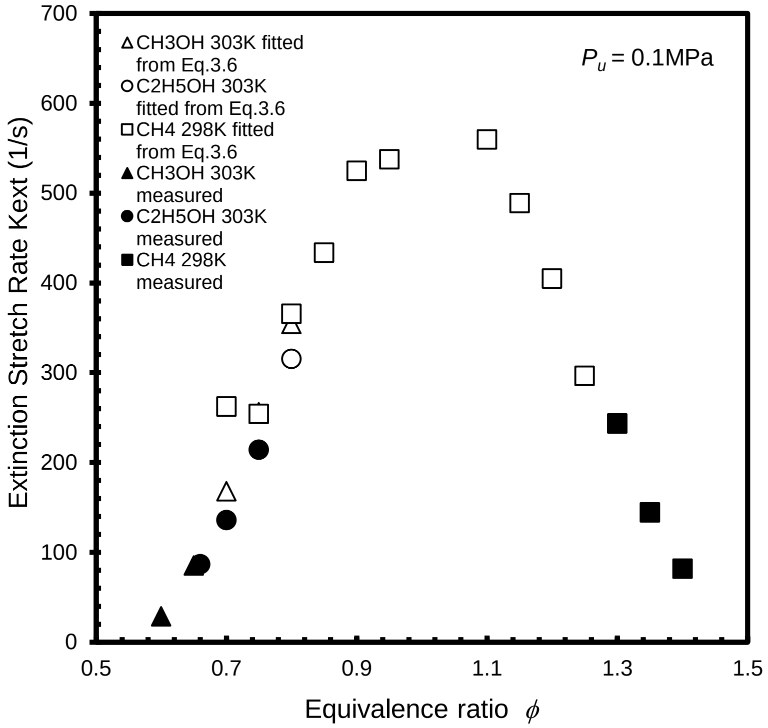

Figure 6.13. αCr from the present work for CH4, CH3OH, and C2H5OH at different equivalence ratios and 0.1MPa.

6.5 Conclusions

The optical technique applied in this study returned values of laminar burning velocity which compare favourably to previously published data for the four fuels investigated. Reasonable agreement was also shown for values derived of Markstein length, with a larger offset evident when compared to traditional linear derived data, in agreement with similar works reported in the literature.

A new approach for the determination of extinction stretch rate was appraised using an outwardly-propagating spherical flame configuration. Experiments conducted employing minimal ignition energy demonstrated how characteristics for propagating flames can be utilised to either measure directly or extrapolate the critical stretch rate.

The non-linear methodology developed generated laminar burning velocity trends which compare very favourably with previously published data for the four fuels investigated. Reasonable agreement was also obtained for derived Markstein lengths, though a larger difference was evident when compared to values obtained from traditional linearised data analysis.

This new methodology required determination of the maximum value of stretch rate corresponding to the turning point of the non-linear relationship between $\boldsymbol{S_n}$ and $\boldsymbol{\alpha}$. However, a reduced dataset must be carefully selected to avoid data influenced by ignition or confinement, hence avoiding inaccurate evaluation of the unstretched flame speed. If this dataset was inappropriately selected, there was potential for error in the interpretation and quantitative analysis of experimental results.

When data was compared to previous studies using the traditional counter-flow technique, a clear correlation was evident, showing the measured critical stretch rate to be representative of the extinction stretch rate as defined in the counter-flowing methodology. Better agreement between the techniques was found for gaseous fuels compared with fuel vapour from two alcohols currently being proposed as alternative fuels, though the latter show similar trends and good agreement with the chemical kinetic scheme used in these work. Extrapolation of the non-linear data enables utilisation of data generated through overdriven flames and/or previously processed using linear analysis, to provide accurate estimates of critical stretch rate and hence extinction stretch rates.

Chapter 7

“Anybody who has been seriously engaged in scientific work of any kind realizes that over the entrance to the gates of the temple of science are written the words ‘Ye must have faith’.”

Max Planck

Laminar Flame Propagation Characteristics through Ethanol Mists

7.1 Chapter Overview

Ethanol in air was chosen to benchmark Cardiff University’s large 35Litre ‘Cloud Chamber’ for preliminary investigation of flame propagation through fuel mists across a wide range of equivalence ratios. The data was subsequently compared to temperature corrected pure vapour mixtures in order to appraise the enhancement in flame speed reported in previous studies, and to compare qualitatively against conflicting published views outlined in literature presented earlier in Chapter 2.

Droplet mist characterisation was undertaken simultaneously prior to ignition, in order to analyse the transitory droplet formation using a Malvern Spraytec system previously discussed in Chapter 3. Higher flames speeds were observed when compared to the richer analogous pure vapour flame case. Based on mechanisms detailed elsewhere that provide a possible explanation for this enhancement full discussion and correlations that help to understand the nature of flame speed through droplet mists are presented.

7.2 Results

A droplet mist characterisation study was undertaken employing first ethanol in Nitrogen (N_2) - to validate the safety of the facilities and operating procedures - then using ethanol in air to validate the performance and repeatability of the experimental methodology and subsequent data processing techniques before combustion was investigated.

Flame propagation was subsequently studied through mists of fuel droplets using Cardiff University's DCCVC presented in Chapter 3. Quantitative comparisons of flames travelling through these fuel mists where made against vapour flames, allowing further comparison of interesting observations reported in the literature. Correlations of different variables are presented in order to help understand the nature of flame propagation through droplet mists. Details of both droplet sizing and combustion experiments are given below.

7.2.1 Droplet mist characterisation

To assess the size ranges of droplets that could be formed in the DCCVC measurements of ethanol/N_2 mixtures were undertaken using the aforementioned Malvern SprayTec laser diffraction analyser.

The parameter extensively used in atomization and combustion studies to describe the average fuel droplet size is that of Sauter Mean Diameter (D_{32}), defined in discrete form as:

$$D_{32} = \frac{\sum n_i D_i^3}{\sum n_i D_i^2} \tag{7.1}$$

Where D_i is the droplet diameter in the i th-size class that has n_i droplets. D_{32} is the ratio of the total droplet volume to the total droplet surface area. Thus, D_{32} relates the total amount of liquid fuel that requires vaporisation to the total surface area available for vaporisation, as such this parameter is an appropriate representation of the characteristic droplet size for combustion [31].

Summarising earlier comments describing the operability of the DCCVC, mist formation occurs when there is a rapid decompression of the combustion chamber brought about by the activation of a pneumatic cylinder which moves a piston, thus rapidly increasing the combustion chamber volume and hence decreasing both the ambient pressure and temperature. This abrupt change in ambient conditions forces super-saturated vapour out of its vapour phase, resulting in spontaneous nucleation and the formation of droplets.

The formation of such a mist is shown in **Figure 7.1** below, where Sauter Mean Diameter (D_{32}) is plotted as a function of time during the expansion of the aforementioned piston. Data in this case is presented for an 'inert atmosphere' experimentation without ignition, so as the quasi-steady period of droplet number and size could be determined. A mass of fuel m_{fuel} = 2.56 g, was injected at initial conditions T_0 = 295.2K and P_0 = 140 kPa to ensure that prior to expansion the airspace was fully saturated.

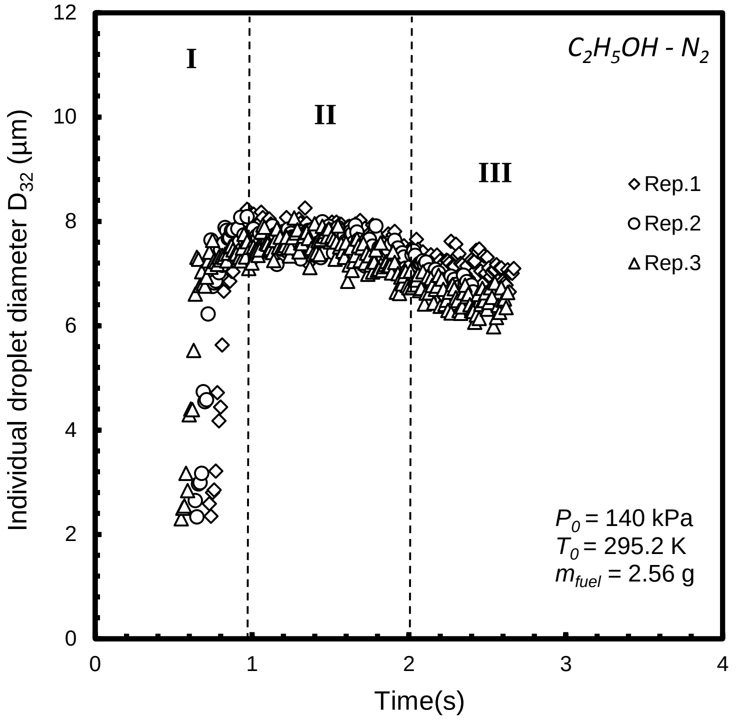

Figure 7.1 Individual Sauter mean diameter (D_{32}) of C_2H_5OH - N_2 as a function of time during expansion process for $Ø_o = 1.115$, $T_0 = 302K$ and $P_0 = 140$ kPa.

Three nominally identical repeats, resulting in decompressions from pre-expansion pressures of P_0 =140 kPa to approximately pre-ignition pressures of P =100 kPa after piston withdrawal, were conducted in order to assess the repeatability of the DCCVC. As can be seen ‘real time’ transient droplet diameter data is captured by the Spraytec measurement system allowing investigation of droplet growth and re-evaporation (Chapter 3).

Figure 7.1 shows the existence of three distinct droplet diameter evolution regimes, namely: a growth in droplet size from 2.5 µm at approximately 0.5 second after the start of the expansion to approximately 7.5 µm at 1 second (Regime I), a stable period of droplet diameter, at approximately 7.5 µm, which exists for a further 1 seconds (Regime II), before a droplet size reduction due to evaporation by heat transfer from the chamber boundaries, observed over the following few seconds (Regime III).

A minimum standard deviation between the three repeats was typically observed during the period between 1.7 and 2 s after start of expansion - towards the end of region II - therefore it was decided that this was the optimal time in which to perform the combustion ignition, hence reducing mist size variability from the combustion dataset.

In order to try and control the droplet size witnessed in the Region II similar tests were performed using ethanol-air mixtures at different initial temperatures. Comparable droplet growth regimes (Region I) are witnessed as to those in **Figure 7.1**, with a similar stabilisation period range for ignition time also being observed. A decrease in the D_{32} is observed with increasing initial temperature, which may be explained by the fact that a larger proportion of the vaporised liquid is being forced out of the saturated mixture due to the lower temperatures resulting in an increase in the measured droplet size.

To ensure accurate repeatable results, the control of D_{32} when investigating unstretched flame speed S_L, ignition was not initiated during Regime I, the period the piston is still in its retraction movement and when the droplets are growing. Therefore, in this study different droplet diameters were investigated by changing the pre-expansion temperature (T_0), with smaller droplet diameters being created by increasing the temperature from that of supersaturated condition.

Again it is seen that the first measurement captured by Spraytec, occurs at a time of approximately 0.5-0.6 seconds from the start of the expansion. And, again the stable region (Region II) still exists at the suggested ignition time of 2 seconds. From the figure it can be surmised that the droplet size growth is strongly dependant on pre-expansion conditions such as P_0, T_0, when expansion ratio defined as $\left(\frac{Vol_2}{Vol_1}\right)$ and given as $\O_o$, remains constant.

7.2.2 Combustion Trials

When satisfied that droplets were controllably and repeatedly produced, combustion trials were initiated (2 seconds after start of expansion) facilitating the investigation of two phase ethanol flames at different ambient conditions ($\boldsymbol{\varnothing_o}$, $\boldsymbol{D_{32}}$, $\boldsymbol{P}$, $\boldsymbol{T}$, and $\boldsymbol{\varnothing_l}$) to be investigated. Three such mixtures and their propagation development - captured as a series of Schlieren images - are displayed in columns from top to bottom showing their respective growth in **Figure 7.2**.

The flame propagation sequence of a lean mixture ($\boldsymbol{\varnothing_o} = 0.821$) is presented in column A of **Figure 7.2**, as can be seen the flame exhibits characteristics comparable to those witnessed when investigating pure vapour flame propagation of non-cracked, smooth, non-cellular flame surface area. However, as can be seen in column B when the overall mixture becomes richer, the onset of cellularity is observed starting; at 11 ms for $\boldsymbol{\varnothing_o} = 1.184$ and becoming earlier as the mixture becomes progressively richer, starting at 7.6 ms for the richest mixture ($\boldsymbol{\varnothing_o} = 1.506$) presented in column C. All these trends agree well with the works of Lawes et al. [92] and Bradley et al. [108].

These observations suggest that the presence of cellularity in droplet flame propagation may affect the resulting flame properties, with the effects becoming more pronounced as liquid equivalence ratio ($\boldsymbol{\varnothing_l}$) increases coupled with an increase of the overall equivalence ratio ($\boldsymbol{\varnothing_o}$). The analysis of the effects of droplets in laminar flame propagation is fully discussed in the following section.

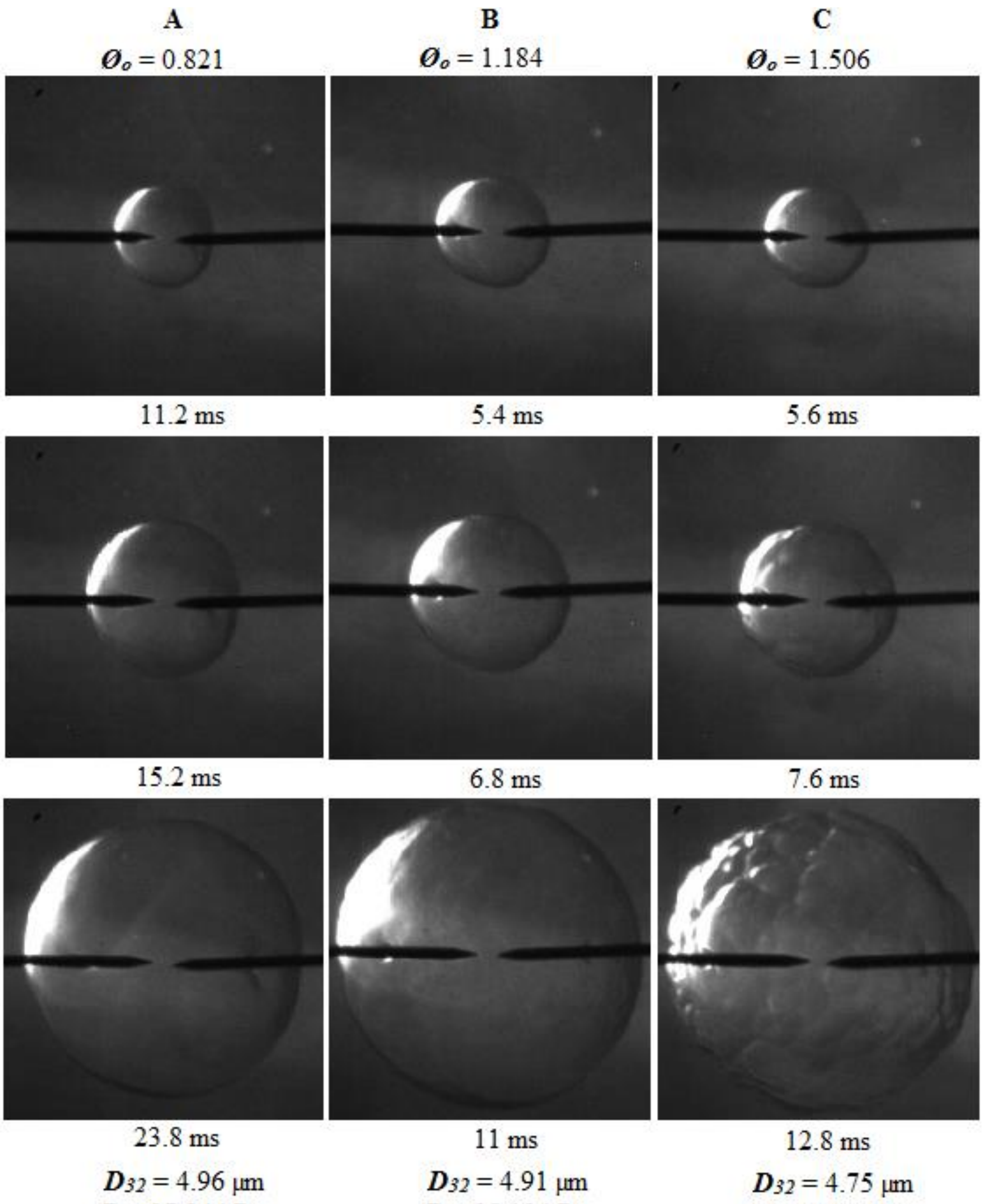

Figure 7.2. Sequence of Schlieren images of droplet flame propagation at different conditions.

7.2.3 Comparison of Laminar flame propagation through mists and vapour

Laminar flame speeds of both mist and vapour flames were measured for ethanol/air mixtures at various equivalence ratios and temperatures at a fixed pre-combustion pressure (***P***) close to atmospheric pressure (1000mbar). Averages of three repetitions are reported at differing combustion mist droplet diameters.

Vapour loadings for the pressure and temperature conditions were calculated using values obtained from the Antoine Equation saturation curve [142], ensuring fully saturated mixtures were present before expansion, for the base line droplet diameter case. As vapour experiments cannot be performed at nominally identical temperatures as those seen at the end of expansion in the droplet cases, in order to facilitate comparison studies a series of experiments for pure vapour at similar pressure conditions were conducted. Again 3 repetitions at each equivalence ratio were undertaken, however to allow comparison to be made 4 different initial temperatures, namely 30, 50, 85 and 100 °C were characterised.

Linear extrapolation was subsequently used in order to obtain a ‘temperature corrected’ flame speed at a corresponding temperature witnessed after expansion in the droplet case.

The effect of temperature on ethanol vapour flames at different AFR’s, is shown in **Figure 7.3a**, with an increase in flame speed observed with increasing temperature, as would be expected. As can be seen at the richer conditions due to the limited vapour pressures data could not be obtained at the lower temperatures leading to limited data points from which a linear extrapolation could be conducted.

As such in order to validate the measured linear extrapolation gradients calculated values of flame speed at varying temperatures were obtained by chemical kinetic modelling using the San Diego [113] mechanism in the Premix coded package CHEMKIN™ with the results given in **Figure 7.3b**.

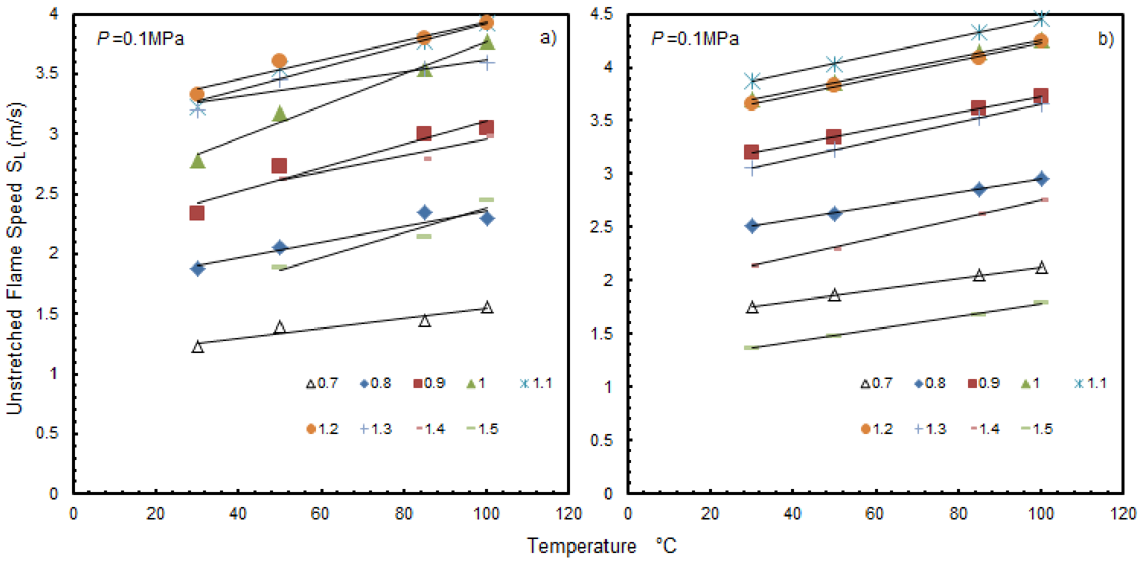

Figure 7.3. Linear extrapolation used in order to obtain the flame speeds at the corresponding temperature drop (a) experimentally and (b) by chemical kinetic modelling.

As can be seen the effect of temperature on flame speed –represented by the gradient of the fitted linear trend lines – is comparable between both the experimental and modelled results, hence, this gradient could be used to correct flame speeds witnessed at the higher temperatures required to facilitate the vapour experiments to predict flame speeds that would be observed if the thermodynamics allowed vapour experiments to be conducted at the lower temperatures – observed after piston expansion – used to generate the mists.

Figure 7.4 shows a comparison of measured unstretched flame speed as a function of overall equivalence ratio ($\boldsymbol{\emptyset_o}$) for both mist and temperature corrected vapour flames, derived using the standard unstretched derivation method described in earlier chapters.

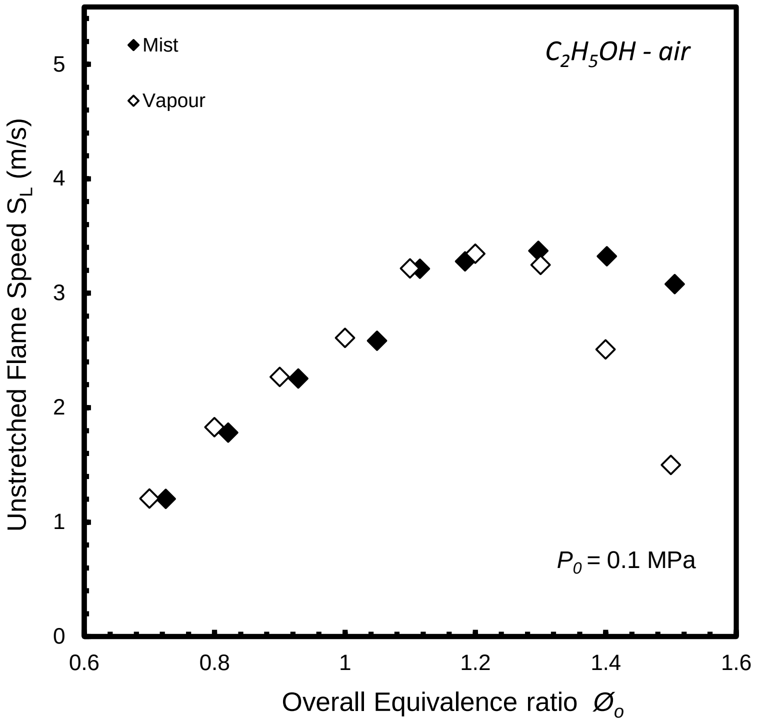

Figure 7.4. Experimentally determined mist and corresponding vapour laminar unstretched flame speed (S_L) as a function of $Ø_o$ at different conditions.

It is observed that in the case of lean combustion, the measured mist laminar flame speeds were subtly lower than those of their comparable vapour flames. An opposite trend was seen in the case of rich combustion – from $\boldsymbol{Ø_o}$ = 1.2966 to 1.506 – where a notably higher flame speed measurement was observed. One possible explanation for this enhancement maybe that cellularity, observed in the richer cases (**Figure 7.2**) could provoke an enhancement in flame speed compared to the smooth vapour case. This cellular instability maybe is the result of the spontaneous effect of droplet diameter stratification due to a convective instability peculiar to fluids with inhomogeneous mass densities subjected to gravity and small thermal gradients; however, another mechanism maybe that the droplets in the rich case, are not fully evaporated in the flame preheat zone, thus creating fuel air ratios entering the flame zone similar to stoichiometry.

It should be noted that the maximum droplet size for lean mixtures in this work was circa 18 µm.

Unfortunately due to limitations in available piston expansion ratio and associated overall temperature reduction, larger droplet diameters in this study could not be repeatedly obtained. This maximum droplet diameter is lower than that reported by Bradley et al. [95] of 23 and 31 µm which showed an enhancement of flame speed at flame radius of 48 mm during lean combustion ($\boldsymbol{Ø_o}$ = 0.8).

However, in the same study Bradley et al. [95] also reported a flame speed increase as droplet diameters decreased for rich combustion ($\boldsymbol{Ø_o}$ = 1.2), following the same trend as the present work.

As the unstretched derivation method of flame speed is reliant on spherical flames in order to derive stretch it was postulated that the cellularity witnessed in rich cases may be inducing an error in the data processing which lead to the observed trend of increased flame speed witnessed during rich combustion through droplets. As such in accordance with suggestions of Bradley et al. [95] an analysis of flame speed at a spatial position where there are minimal stretch rate effects was undertaken. Due to the size of the viewing windows in this study the maximum radius which could be analysed before pressure effects became dominant was at a flame radius of 38mm (defined in Chapter 3) as such the instantaneous flame speed at this flame radius was derived ($\boldsymbol{S_{L38}}$), and is analogous to the flame speed measured by Bradley et al. [95] at 48mm ($\boldsymbol{S_{L48}}$). Along with the $\boldsymbol{S_{L38}}$ spatial flame speed a maximum measured flame speed ($\boldsymbol{S_{Lmax}}$) was also derived, from data in the limited flame radius range deemed spark, pressure and cellularity unaffected, these flame speeds are presented in **Figure 7.5a** and **Figure 7.5b**, respectively.

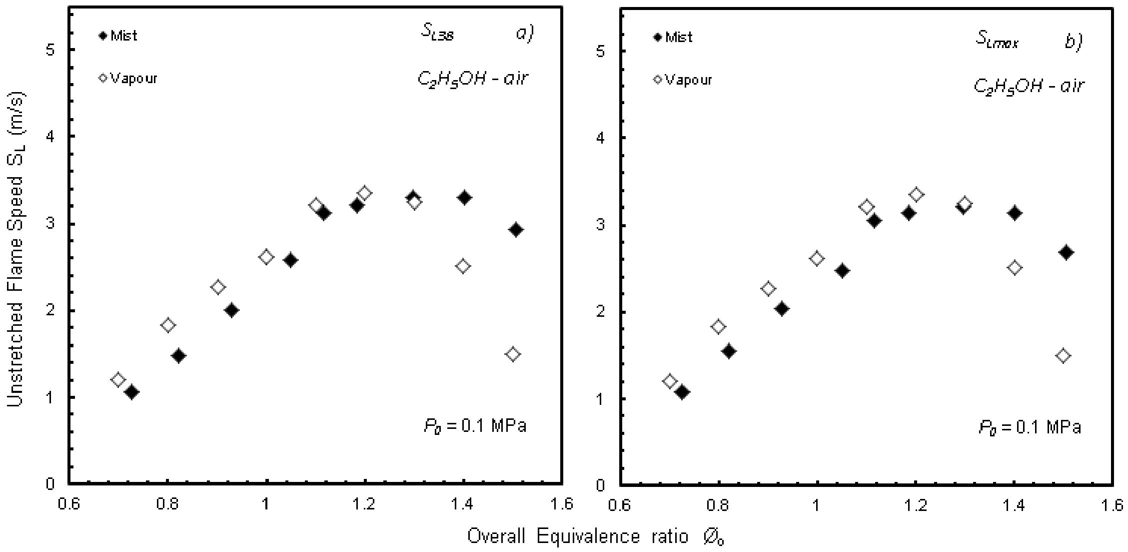

Figure 7.5. Experimentally determined mist and corresponding vapour laminar unstretched flame speed (S_L) as a function of $Ø_o$ at different conditions for (a) radius of 38 mm, and (b) radius at maximum flame speed.

As can be seen the same general trend of decreased burning rate during lean combustion and enhancement on the rich side are observed, in agreement to the results found using contemporary processing techniques exhibited in **Figure 7.4**. However, it is seen that a larger difference is observed between the measured mist and corresponding vapour flame speed in **Figure 7.5a** when looking at the speed at a point furthest from the point of ignition. These findings supported that the presence of droplets induce an enhancement of flame speed compared to a comparable vapour case, however do not enhance flame speeds to values greater than those observed at stoichiometry. Further discussion into this phenomena is presented in section 7.3.

From the same datasets an investigation of the variation of L_b with $Ø_o$ for mist and vapour flames under the same conditions is also presented. L_b in this case is calculated using the same analysis techniques presented earlier for single phase flames, with data presented in **Figure 7.6**.

As such data marked as grey diamonds in **Figure 7.6** corresponds to points affected by cellularity, thus at these points L_b values calculated by single phase analysis- aimed at laminar flame growth, where stretch is assumed from a spherical growth - must be carefully interpreted, and should not be compared with the corresponding vapour cases as the actual stretch rates at these points is almost certainly much higher than predicted by the laminar assumption, due to the cellular structure.

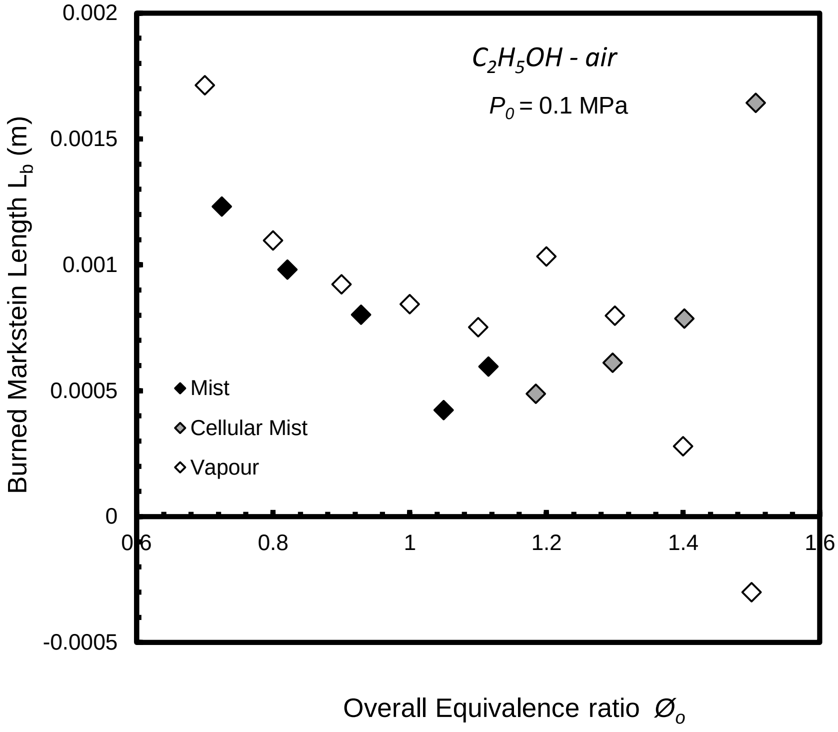

Figure 7.6. Variation of L_b with $Ø_o$ for mist and vapour flames under the same conditions.

However, it can be seen that if a linear extrapolation is applied to the mist flames values before cellularity affects the data, it can be surmised that at equivalence ratios of greater than 1.5 there is a change in polarity of Markstein Length for both vapour and mist ethanol flames.

Having observed subtle variations in ***S_L*** and ***L_b***, it was deemed necessary to study the effect of different ***D_{32}*** sizes - especially for rich mixtures – to determine whether further enhancement could be shown.

7.2.4 Effects of D_{32} on flame speed for mist flames

The effect of D_{32} on unstretched flame speed (S_L) at different $Ø_o$ and T_o, was subsequently studied, whilst aiming to maintain constant ambient pressure (***P)*** conditions at atmospheric pressure after piston expansion so as this data set could show the existence of an optimum droplet size which favoured further enhancement of S_L, thus supporting the simulated enhancements reported by Polymeropoulos [85].

Figure 7.7 shows the variation of S_L with D_{32} for different equivalence ratio's and initial temperatures. As discussed earlier the rapid decompressions took place from pre-expansion pressures P_0 = 140 kPa resulting in pre-combustion pressures P = 100 kPa.

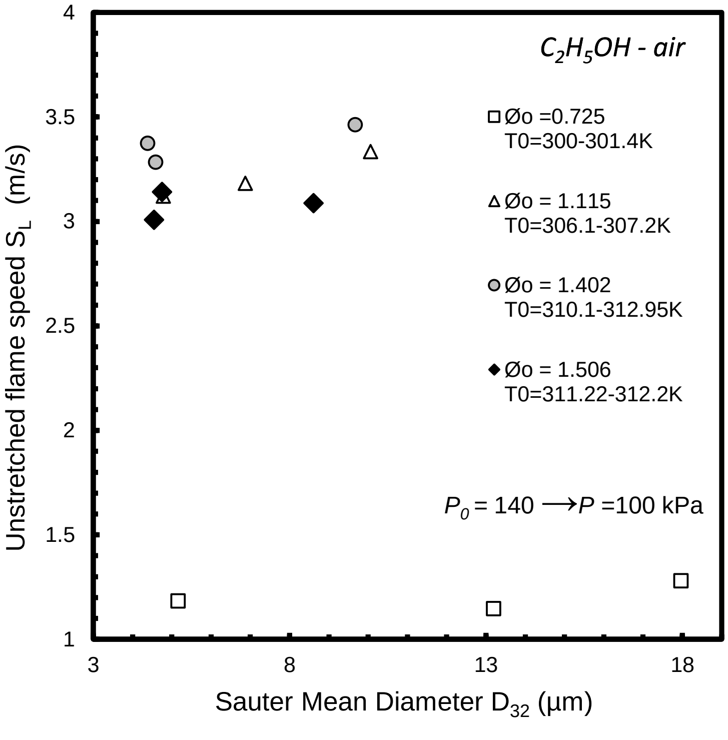

Figure 7.7. Variation of S_L with D_{32} for different $Ø_o$ and T_0 at constant P after rapid decompression.

As discussed earlier the droplet diameter (D_{32}) size was controlled by increasing the initial temperature (T_0) before volume expansion and subsequent ignition time, giving a decrease in D_{32} size as T_0 increased, from the super-saturation temperature. Bradley et al. [95] presented in their work an increase in S_L as D_{32} also did at lean mixtures driven by sufficiently large droplets (23 and 31 µm), meaning that mist flame S_L is higher than that of the analogous vapour flame. However, due to the limitations of the Cardiff University's DCCVC the maximum D_{32} size (18 µm) obtained was unable to reach the aforementioned flame speed enhancement.

For mixtures at $Ø_o$ = 1.402 all droplet diameters were smaller than those at $Ø_o$ = 1.115; nevertheless, a higher S_L was obtained at the richer mixture for all comparable diameter sizes. Furthermore, although the mist flame at $Ø_o$ = 1.402 was tested at a higher pre-ignition temperature T than that of $Ø_o$ = 1.115, if applying a temperature correction to allow for increases in flame speed with initial temperature witnessed in the case of gaseous flames then an opposite tendency suggesting that the enhancement was fostered by an 'optimum' small droplet diameter at rich mixtures. Trends exhibited by Bradley et al. [95] showed that flame speed (S_{48}) increased as droplet diameters decreased for rich combustion ($Ø_o$ = 1.2). However, it should be noted that due to temperature being used to control droplet size then different volumes of fuel are held in the liquid phase at small and larger droplet size meaning it is not at this time possible to decouple whether any subtle differences observed are a result of droplet size or differences in the liquid to vapour ratio.

For mixtures at $Ø_o$ = 1.506 the S_L reached with small droplet diameter was similar to those at comparable droplet size for $Ø_o$ = 1.115. However, again, although it can be argued that the T was higher for $Ø_o$ = 1.506 than that for the leaner mixture ($Ø_o$ = 1.115), this would contradict the trends observed when comparing between the pure vapour cases in **Figure 7.4** and in **Figure 7.5** which S_L for $Ø_o$ = 1.506 is much lower than that of $Ø_o$ = 1.115.

Finally, tests at lower initial pre-expansion pressures (***P_0***) were undertaken varying ***D_{32}*** in order to obtain the effects on ***S_L*** at different rich equivalence ratios, for which the optimum droplet sizes could be generated. The results are given in **Figure 7.8**. Pre-expansion pressures either ***P_0*** = 130 kPa or ***P_0*** = 120 kPa were utilised resulting in a pre-ignition pressure of ***P*** = 82 kPa and ***P*** = 89 kPa, respectively.

Again, polynomial extrapolation was used in order to obtain the flame speeds at the corresponding pre-combustion pressure. Theoretical values were calculated by chemical kinetic model using San Diego [113] mechanism in the Premix coded package CHEMKIN™ testing four different initial pressures, namely 0.5, 0.7, 0.9 and 1 bar, for each point of the three different equivalence ratios presented in **Figure 7.8**.

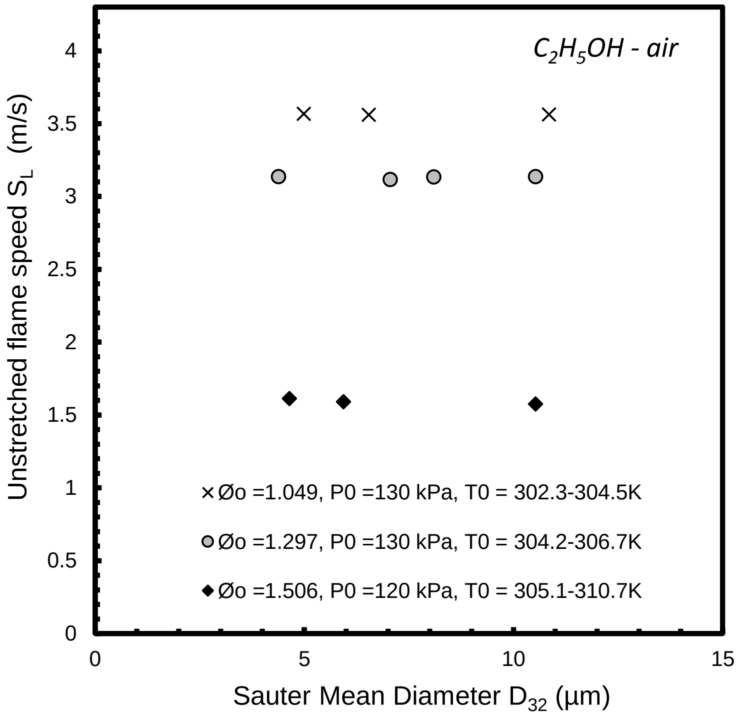

Figure 7.8. Variation of S_L with D_{32} for different $Ø_o$, T_0 and P_0 after rapid decompression.

As described earlier in order to fix the droplet size at a perceived optimum, tests at selected lower pre-expansion pressures (***P_0***) were performed compared with pressures used for data presented in previous figures. To achieve these droplet sizes the rate of piston retraction was reduced; however, as it can be seen in **Figure 7.8** the maximum D_{32} measured using this configuration was 11 µm at these initial conditions, thus in this test configuration an extension the range of droplet diameters for the analysis was not possible.

In all $Ø_o$ and, hence, $Ø_l$, at different conditions the presence of an optimum droplet diameter enhanced S_L values was not observed repeating the general trend seen **Figure 7.7**. It is important to note that although smaller droplet diameters were obtained at higher pre-expansion temperatures, lower S_L values were obtained, however there would obviously be lower fuel in the 'wet' droplet phase for these cases meaning any enhancement may be more difficult to observe or that the larger inter-droplet distances may be limiting any enhancement.

7.3 Discussion of experimental results

The sequence of Schlieren images displayed in **Figure 7.2** illustrates two scenarios: the first which even at high stretch rates (α) droplet flames remained smooth and free of wrinkles and cells resulting in lower S_L values than those of corresponding gaseous flames, this is in agreement with previous works presented by Lawes et al. [92]. The second scenario highlighted that at low stretch rates spherical flames became more cellular in the case of droplet combustion, provoking an enhancement in the droplet flame speeds at specific conditions comparing to those of the analogous gaseous flames.

A possible explanation for the first scenario is given by the mechanism presented by Bradley et al. [95] – presented by **Figure 7.9**– in which they stated that after relatively small droplets cross the front of preheat zone, almost complete evaporation takes place provoking a substantial reduction in the final temperature of the reaction zone, due to the associated evaporation enthalpies. This energy loss and resultant temperature reduction evolves in a reduction in the measured flame speed compared to the benchmark gaseous flame, a trend again shown in this study as presented in **Figure 7.4** of the present work and in agreement with the temperature effects shown in **Figure 7.3**.

On the other hand, the second scenario could be explained by the presence of small droplets in the preheat zone of rich mixtures boosting intrinsic Darrieus-Landau [143, 144] thermodiffusive instabilities and wrinkling at these conditions [95]. Extensive studies of flame instabilities and the formation of cellular structures during spherical gaseous explosions have been undertaken by Bradley et al. [145] supporting this phenomena.

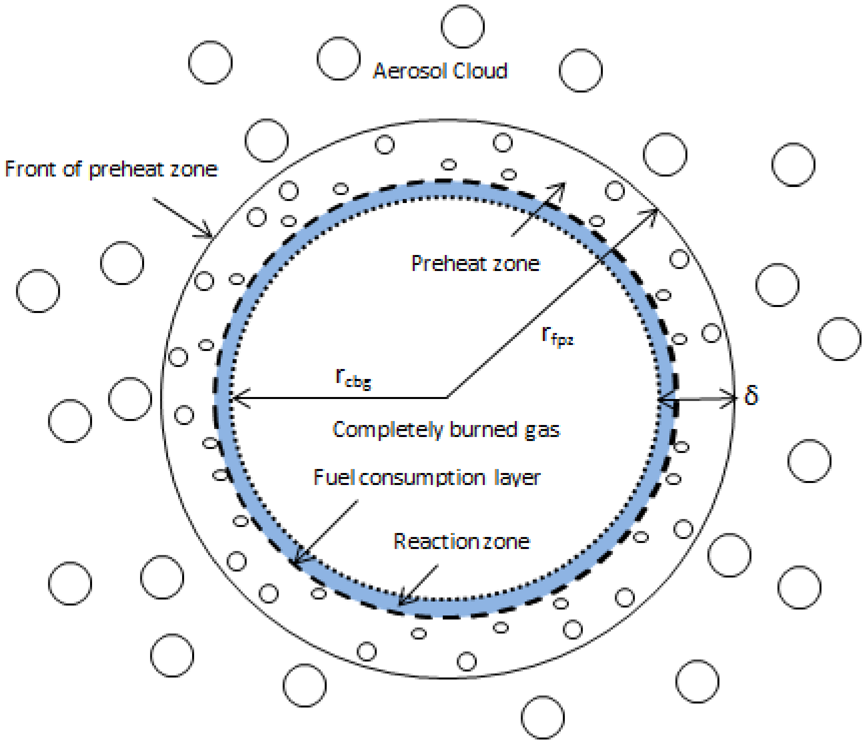

Figure 7.9. Spherically expanding aerosol flame configuration with evaporation completed in the preheat zone [95].

According to Bradley et al. [95] the presence of droplets in richer mixtures causes the existing gaseous instabilities to become further intensified resulting in additional flame wrinkling. This process in turn provokes higher values of flame speed when compared to the corresponding gaseous flame. It is important to note that Bradley's et al. [95] results are expressed in terms of mass burning velocity and the comparisons through the present work are qualitative.

Another complementary explanation of this enhancement is given by Neophytou and Mastorakos' [94] whom developed a mechanism for conducting simulations for n-heptane and n-decane. According to the authors the surviving droplets that cross the preheat zone in rich mixtures create effective equivalence ratio ($Ø_{eff}$) conditions which have similar properties to that of a stoichiometric state. Moreover, the oxidiser is completely consumed in the reaction zone and the droplets left behind are pyrolysed. The resulting reactive radicals during ethanol pyrolysis such as CH_3, H, OH, etc. [146] diffuse back to the oxidation zone causing faster reaction rates, hence, the aforementioned flame speed enhancement is seen. Neophytou and Mastorakos [94] defined the $Ø_{eff}$ as 'the equivalence ratio, based on the mass fraction of the carbon element in the gas, at the location where the heat release becomes a maximum'.

Regarding the shift in L_b direction for the droplet flames reported in **Figure 7.6**, these trends obtained in the present work could be qualitatively explained in similar fashion as discussed by Lawes et al. [92] using heat and mass diffusion effect represented by Le. According to Bradley and Harper's [130] study of flame instabilities for a broad variety of mixtures, they state that the relationship between L_b and Le behaves linearly. Again two scenarios were utilised in order to describe the L_b behaviour: the first one corresponds to the decrease of L_b with $Ø_o$ up to an inflection point which occurred at $Ø_o = 1.184$, and the second one in which the opposite trend was observed after the aforementioned turning point. In the first scenario the droplets evaporation through the preheat zone absorb heat as they reduce their size causing a reduction in the heat diffusion from the reaction zone; along with a plausible small diffusion of droplet mass. Consequently, the presence of the droplets evaporation foster the reduction of ***Le*** and, hence, $\boldsymbol{L_b}$. Conversely, the second scenario could be elucidated using Neophytou and Mastorakos' [94] mechanism. The surviving droplets that enter the rich mixtures preheat zone promote $\boldsymbol{Ø_{eff}}$ conditions in which these droplet are pyrolysed due to the complete consumption of the oxidizer. The resulting reactive radicals bring about faster reaction rates encouraging the necessary heat diffusion from the reaction zone to increase ***Le*** and, hence, $\boldsymbol{L_b}$.

The existence of an optimum droplet size that favoured the enhancement of $\boldsymbol{S_L}$ suggested by simulations and reported by Polymeropoulos [85] was not observed. However, small droplet sizes in the rich side not only could favour the onset of instabilities, but also gives the range of plausible droplet diameters that survive in the preheat zone fostering the creation of an $\boldsymbol{Ø_{eff}}$ necessary to obtain the enhancement mechanism proposed by Neophytou and Mastorakos [94].

7.4 Conclusions

The modification of the Cardiff University's constant volume combustion chamber used to measure gaseous mixtures properties was undertaken in order to study droplet flame propagation characteristics. With the new modified rig (DCCVC) a variety of different mists were generated and the resultant flame properties measured and compared with those of corresponding gaseous flames at the same conditions. The main findings were:

- After analysing the transitory droplet formation the ignition time was set at 2 s after the start of measurements given by Spraytec system, to ensure the most stable droplet sizes.

- Mist flames and vapour flames characteristics were compared quantitatively at different condition for a wide range of equivalence ratios.
- Through analysis of Schlieren images it was noted that the onset of instabilities in mist flames occurred earlier, resulting in flame speeds higher than those of vapour flames at the same conditions.
- Qualitatively comparisons with the sparse previous works found in literature were made finding agreement with the trends reported in the present work for ethanol-air mixtures.
- The variation of L_b with $Ø_o$ was investigated for mist and vapour flames under the same conditions highlighting a shift in L_b direction at certain conditions, by correlating this behaviour with the onset of instabilities at certain D_{32} values an enhancement in flame speed could be shown for rich mist flames.

Chapter 8

"The scientific man does not aim at an immediate result. He does not expect that his advanced ideas will be readily taken up. His work is like that of the planter - for the future. His duty is to lay the foundation for those who are to come, and point the way."

Nickola Tesla

Conclusions and Future Work

The aim and main objectives of this study specified in Chapter 1 have been broadly achieved, whilst areas for further research have been identified.

Main achievements of the work

- All previous extinction stretch rate research studies have determined this parameter using the traditional well-established counter-flowing flame technique, leaving the study of alternative methodologies of its determination relatively unexplored. In this thesis such an approach using outwardly propagating spherical flames within a constant volume combustion chamber has been developed and appraised. This was achieved by studying methane, propane, ethanol and methanol flames in a fully-confined cylindrical constant volume chamber used for laminar flame speed characterisation operating at different initial conditions.

- A re-analysis of a detailed experimental investigation into the effect of water vapour as a suppressant on freely propagating methane flames using Cardiff University's previous cloud-combustor has been undertaken. A low energy ignition system was employed to enable the elusive early non-linear stages of the flame propagation against stretch rate to be captured. Moreover, the increased Markstein length derived for the 15 % water loading case was attributed to non-linear trends in the stretched flame speed data showing that the unsteady outwardly spherically flame transition at high water loadings and low ignition energies caused a flame speed reversal phenomenon at a critical point. The trajectory prescribed is similar to those captured and analysed using the by the non-linear methodology employed in this thesis.

- Experiments conducted utilising low ignition energies showed promise for directly measuring a proposed critical stretch rate experimentally, so long as the subset of data employed was carefully selected to avoid external influences. Furthermore, it was also observed that the non-linear correlation from previous overdriven studies employed can be used to approximate this value.

- By comparison to previous studies using the more established counter-flow burner technique this study shows that critical stretch rate is representative of the extinction stretch rate with the following trends observed: increases in equivalence ratio increased the critical stretch rate, decreasing initial pressure brought about a reduction in critical stretch rate, and with increasing initial temperature the observed critical extinction limit increased.

- When data for the four chosen fuels was compared to previous studies using the traditional counter-flow technique, better agreement between the techniques was found for gaseous fuels compared with fuel vapour from two alcohols currently being proposed as alternative fuels, though the latter show similar trends and good agreement with the chemical kinetic scheme used in this work. Extrapolation of the non-linear data enables utilisation of data generated through overdriven flames and/or previously processed using linear analysis, to provide accurate estimates of critical stretch rate and hence extinction stretch rates. Critical extinction stretch rate limits demonstrated a universal curve for the chosen fuels, represented simply in terms of the laminar burning rate, Markstein length and expansion ratio.

- A new experimental facility has been developed and commissioned that enables concurrent droplet size measurement within the practical ‘transition size range’ and laminar flame characterisation for a propagating flame for the first time.

- Ethanol in air was chosen to benchmark and investigate droplet flame propagation across a wide range of equivalence ratios at the same conditions as those of corresponding gaseous flames in order to study the reported enhancement in other works, and to compare qualitatively against conflicting published views reported in literature. It can be concluded that this enhancement was observed at rich mixtures for small droplet diameters.

- The onset of instabilities resulted in mist flame speeds that were higher than those of vapour flames at the same conditions. The mechanisms that may fostered this enhancement and may be applicable are considered to be that of small droplet diameters that survive in the preheat zone foster the creation of conditions which have similar properties to that of a stoichiometric state favouring this enhancement.

- The variation of Markstein length with overall equivalence ratio for mist and vapour flames under the same conditions highlights a shift in Markstein length direction at specific conditions. This behaviour correlates with the onset of instabilities at certain Sauter mean diameter values that favoured the enhancement in mist flames.

Future Work

The extinction stretch rate obtained using outwardly propagating flames agreed well in some cases with a single-jet wall non adiabatic plate configuration in the present work. However, the global stretch in the expanding flame configuration induced by the hot gases would change the dynamic of the flame and its growth, hence, it would be interesting to study how comparable are the results obtained using the opposed-jet and single jet wall adiabatic configurations and how the sensitivity of the approximate formulation should be affected. Furthermore, measurements at higher pressures and for other alternative mixtures such as those containing variable hydrogen fractions and water vapour should be investigated due to its impact in the sensitivity change of the combustion properties.

In the laminar flame propagation through mists investigation different conditions for the same equivalence ratio were achieved changing the initial expansion pressure; nevertheless, a variation of the preselected instant for ignition during expansion (Regime I in **Figure 7.1**) is suggested due to the required mist characteristics could be broaden facilitating the study of an optimum droplet size that favoured the enhancement of unstretched flame speed and, hence, laminar burning rate.

Markstein length measurements of the mist flames were calculated by single phase analysis – aimed at laminar flame growth, where stretch is assumed from a spherical growth; however, a different method should be developed to obtained more precise values of the points affected by cellularity in order to compared with the corresponding vapour cases as the actual stretch rates at these points is almost certainly much higher than predicted by the laminar assumption, due to the cellular structure.

The maximum droplet size at lean mixtures obtained in the present work was 18 µm due to limitations and difficulties of cooling the cloud chamber in order to obtain larger droplet diameters. Therefore, in order to obtain larger range of diameters it is suggested a second piston addition resulting in a better expansion control along with the use of a cooling system for lower temperatures achievement.

Better temperature data acquisition system should be utilized owing that live temperature readings were not able to be obtained during rapid decompression due to the limitation in time response from two k-type thermocouples, hence, avoiding the temperature drop approximation using the ideal gas law.

Further work should be centred on the use of the Cardiff University's new, large 35Litre 'Cloud Combustor' developed and commissioned enabling larger droplet sizes measurement within the practical 'transition size range' and turbulent flame characterisation for power generation, suppressing propagation and transportation applications using alternative fuel mixtures.

Appendix A – Relationship between Le – Lb, and calculations of some related parameters

According to Law [31] it is clear that practically all flame configurations adopted in the determination of the unstretched flame speed S_L suffer stretch. These stretch effects have to be subtracted out when determining u_L from stretched flames.

For a given stretch rate α, the global responses of a stretched flame depend on global properties such as flame thickness (δ), and ***Le***, recognising that δ is needed in the evaluation of ***Ka*** (**Eq. A.6**).

Conventionally, ***Le*** is evaluated based on the freestream properties of the mixture, with the mass diffusivity being that of the deficient reactant and the abundant inert. This evaluation therefore embodies two assumptions, namely ***Le*** is only a diffusive property of the flame, and it is only applicable to sufficiently off-stoichiometric mixtures. The potential inadequacy of the first assumption can be appreciated by recognising that since the flame is a diffusive-reactive system, ***Le*** should be a global diffusive-reactive property.

Specifically, the progress of the individual reactions obviously depends on the availability and concentrations of the intermediates, which in turn depend on the transport aspects of the mixture and the flame structure. Therefore, although ***Le*** is superficially a parameter representing the transport of the freestream reactants, there are many intermediates, with different diffusivities, that could affect the entire reaction progress and manifest their effects through some nonequidiffusive phenomena. As such, ***Le*** is fundamentally a flame-dependent property.

The extraction of ***Le*** is conducted based on the response of stretched flames, which is sensitive to ***Le*** variations. **Equation A.1** expresses the result of how the flame speed varies linearly with the stretch rate for small α.

$$S_L - S_n = L_b \alpha \qquad \text{(A.11)}$$

Where L_b is the slope of the linear variation and is called the Markstein length (based on the downstream burning velocity) of the flame, measuring its response to stretch rate variation. However, S_n is also given by **Eq. A.2** as

$$S_n \approx S_L + \left[\frac{Ze}{2} \left(\frac{1}{Le} - 1 \right) - 1 \right] \left(\frac{\delta \rho_u}{\rho_b} \right) \alpha \qquad \text{(A.12)}$$

Where ***Ze*** is the Zel'dovich number, ρ_u and ρ_b are the unburned and burned gas density, respectively. Thus equating the slopes of both equations, we have **Eq. A.3**.

$$L_b = \left[\frac{Ze}{2} \left(\frac{1}{Le} - 1 \right) - 1 \right] \left(\frac{\delta \rho_u}{\rho_b} \right) \tag{A.13}$$

From which ***Le*** can be determined.

Equation A.1 can also be expressed in the following form:

$$\frac{S_n}{S_L} = 1 - Ma \cdot Ka \tag{A.14}$$

Where ***Ma*** and ***Ka*** are the respective Markstein and Karlovitz numbers defined thus:

$$Ma = \frac{L_b}{\delta} \tag{A.15}$$

$$Ka = \frac{\delta}{S_L} \cdot \alpha \tag{A.16}$$

With ***δ*** representing the flame thickness, defined as the quotient of thermal diffusivity (***k***) to the laminar burning velocity.

Appendix B – Matlab Script

```
clear all

path(path,'D:\try');
fileFolder = fullfile('D:','try');
dirOutput = dir(fullfile(fileFolder, '*.tif'));
fileNames = {dirOutput.name}';
tic

r=1;
A1 = imread( fileNames {r} );
B0 = edge (A1, 'canny', 0.06);
%figure, imshow (B0), title ('B0');
B = imcrop (B0, (307,293,77,96));

offset = 1;

for x = 30:40;
for k = 1:55;

    A = imread( fileNames {k} );
    D0 = edge (A, 'canny', 0.06);
    D = imcrop (D0, (307,293,77,96));
    %figure, imshow (D), title ('D');
    E = D-B;
    %figure, imshow (E), title ('E');
    t = 1/5000 ;

    C = imcrop ( E, (x, 2, 0, 92));
    %C = imcrop ( E,(140, 180, 530, 70));
    %figure, imshow (C), title ('C');


    ll1 = find ( C==1, 1, 'first');
    rr1 = find ( C==1, 1, 'last');

    lcol = ll1;
    lcol1 = ceil(lcol);

    rcol= (93-(93-rr1));
    rcol1= ceil(rcol);


    if ((isempty(ll1))||(isempty(rr1)))
        fd(k) = 0;
        P(k) = 0;
    else
        fd(k) = rcol1-lcol1;
        P(k) = (93-((lcol1*93)-ll1));
    end;
```

```
end

Tfd = transpose (fd);
%TP = transpose (P);

xlswrite('Result.xls',Tfd,1,sprintf('A%d',offset));
offset = offset + size(Tfd,1);

%xlswrite('Result.xls',TP,1,'B1');
end
```

Appendix C – Calculation of the partial pressures of both the fuel and oxidizer

$$\mathrm{AFR}_{\mathrm{actual}} = \frac{\mathrm{m}_{\mathrm{ox}}}{\mathrm{m}_{\mathrm{fuel}}} \tag{1}$$

$$\phi = \frac{\mathrm{AFR}_{\mathrm{stoich}}}{\mathrm{AFR}_{\mathrm{actual}}}$$

$$\mathrm{AFR}_{\mathrm{actual}} = \frac{\mathrm{AFR}_{\mathrm{stoich}}}{\phi} \tag{2}$$

Rearranging (1) and (2)

$$\mathrm{m}_{\mathrm{fuel}} = \frac{\phi\,\mathrm{m}_{\mathrm{ox}}}{\mathrm{AFR}_{\mathrm{stoich}}} \tag{3}$$

Using the ideal gas Law

$$\mathrm{PVol} = \mathrm{nRT} \tag{4}$$

where

$$\mathrm{n} = \frac{\mathrm{m}}{\mathrm{M}} \tag{5}$$

So rearranging (4) and substituting for (5) gives

$$\mathrm{P} = \frac{\mathrm{mTR}}{\mathrm{MVol}} \tag{6}$$

Dalton's Law of Partial pressure states

$$\mathrm{P}_{\mathrm{T}} = \mathrm{P}_{\mathrm{i}} + \mathrm{P}_{\mathrm{j}} + \mathrm{P}_{\mathrm{k}} \cdots$$

Where P_T represents the total pressure as the summated total of individual gas (n_x) partial pressure constituents. For an ideal gas the ratio of partial pressures is the same as the mole fraction, where

$$\mathrm{x}_{\mathrm{i}} = \frac{\mathrm{P}_{\mathrm{i}}}{\mathrm{P}_{\mathrm{T}}} = \frac{\mathrm{n}_{\mathrm{i}}}{\mathrm{n}_{\mathrm{T}}}$$

So

$$\mathrm{P}_{\mathrm{i}} = \mathrm{P}_{\mathrm{T}}\mathrm{x}_{\mathrm{i}} = \mathrm{P}_{\mathrm{T}}\frac{\mathrm{n}_{\mathrm{i}}}{\mathrm{n}_{\mathrm{T}}}$$

In this case the pressure is made of the partial pressures of the fuel, and of the oxidiser.

$$\mathrm{P}_{\mathrm{T}} = \mathrm{P}_{\mathrm{fuel}} + \mathrm{P}_{\mathrm{ox}}$$

Substituting for the rearranged ideal gas equation (6), gives

$$P_T = \left[\left(\frac{m_{fuel}T_{fuel}R}{M_{fuel}Vol}\right)+\left(\frac{m_{ox}T_{ox}R}{M_{ox}Vol}\right)\right] \qquad (7)$$

The universal gas constant, and volume of the chamber do not change and therefore allow the equation to be rearranged to give

$$\frac{P_T V}{R} = \left[\left(\frac{m_{fuel}T_{fuel}}{M_{fuel}}\right)+\left(\frac{m_{ox}T_{ox}}{M_{ox}}\right)\right] \qquad (8)$$

Rearranging (1) gives

$$m_{ox} = m_{fuel}AFR_{actual} \qquad (9)$$

Substituting (9) into (8) gives

$$\frac{P_T V}{R} = \left[\left(\frac{m_{fuel}T_{fuel}}{M_{fuel}}\right)+\left(\frac{m_{fuel}AFR_{actual}T_{ox}}{M_{ox}}\right)\right] \qquad \Rightarrow \frac{P_T V}{R} = m_{fuel}\cdot\left[\left(\frac{T_{fuel}}{M_{fuel}}\right)+\left(\frac{AFR_{actual}T_{ox}}{M_{ox}}\right)\right]$$

Rearranging to give

$$m_{fuel} = \frac{\left(\frac{P_T Vol}{R}\right)}{\left[\left(\frac{T_{fuel}}{M_{fuel}}\right)+\left(\frac{AFR_{actual}T_{ox}}{M_{ox}}\right)\right]} \qquad (10)$$

And similarly rearranging (1) to give

$$m_{fuel} = \frac{m_{ox}}{AFR_{actual}}$$

Allows for substitution into (10) to give

$$m_{ox} = \frac{\left(\frac{P_T Vol}{R}\right)}{\left[\left(\frac{T_{ox}}{M_{ox}}\right)+\left(\frac{T_{fuel}}{AFR_{actual}M_{fuel}}\right)\right]} \qquad (11)$$

The masses can be used to calculate the number of moles using (5)

$$n_{fuel} = \frac{\left(\frac{P_T Vol}{R}\right)}{M_{fuel}\left[\left(\frac{T_{fuel}}{M_{fuel}}\right)+\left(\frac{AFR_{actual}T_{ox}}{M_{ox}}\right)\right]} \qquad \Rightarrow n_{fuel} = \frac{\left(\frac{P_T Vol}{R}\right)}{\left(T_{fuel}+\frac{M_{fuel}AFR_{actual}T_{ox}}{M_{ox}}\right)}$$

And similarly

$$\Rightarrow n_{ox} = \frac{\left(\frac{P_T Vol}{R}\right)}{\left(T_{ox} + \frac{M_{ox} T_{fuel}}{AFR_{actual} M_{fuel}}\right)}$$

Thereby allowing for the calculation of the partial pressures of both fuel and oxidiser

$$P_{fuel} = P_T \left(\frac{n_{fuel}}{n_{ox} + n_{fuel}}\right) \tag{12}$$

$$P_{ox} = P_T \left(\frac{n_{ox}}{n_{ox} + n_{fuel}}\right) \tag{13}$$

References

1. Schumann, J. and S. Vossoughi. *Unconventional gas resources in the U.S.A.* in *AIP Conference Proceedings*. 2011.

2. International Energy Agency. *World Energy Outlook 2012 Chapter 7 - Renewable Energy Outlook*. 2012 [20/09/2013]; Available from: http://www.worldenergyoutlook.org/media/weowebsite/2012/WEO2012_Renewables.pdf.

3. Pielke Jr, R.A., *The British Climate Change Act: a critical evaluation and proposed alternative approach.* Environmental research letters, 2009. **4**(2).

4. Energy Information Administration, U.S. *International Energy Outlook 2013*. [26/09/2013]; Available from: http://www.eia.gov/forecasts/ieo/pdf/0484(2013).pdf.

5. Schornick, J.F., R.T. Farr, and J.K. DiCampli, *Liquid biofuels in the aeroderivative gas turbine*, in *General Electric Report, Houston, Texas, USA. 2011 Available from:* *http://www worldenergy. org/docu ments/congresspapers/119. pdf [June 2011]2010.*

6. Moreira, J.R. and J. Goldemberg, *The alcohol program.* Energy Policy, 1999. **27**(4): p. 229-245.

7. Thomas, V. and A. Kwong, *Ethanol as a lead replacement: Phasing out leaded gasoline in Africa.* Energy Policy, 2001. **29**(13): p. 1133-1143.

8. Holley, A.T., Dong, Y., Andac, M. g. and Egolfopoulos, F.N, *Extinction of premixed flames of practical liquid fuels: Experiments and simulations.* Combustion and Flame, 2006. **144**(3): p. 448-460.

9. Wang, C.H., G.J. Ueng, and J.J. Jehng, *The extinction limits and near-limits behaviors of premixed ethanol/air flame.* International Communications in Heat and Mass Transfer, 1997. **24**(5): p. 695-708.

10. Lefebvre, A.H. and D.R. Ballal, *Gas Turbine Combustion. Alternative Fuels and Emissions*. 2010, Boca Raton, FL CRC Press.

11. Power Technology, *Ethanol Power Plant, Minas Gerais, Brazil*, 2012 [25/09/2013]; Available from: http://www.powertechnology.com/projects/ethanol-power-plant/.

12. General Electic, G. *Feasibility of Methanol as Gas Turbine Fuel*. 2001; Available from: http://www.methanol.org/Energy/Resources/Fuel-Cells/GE-White-Paper.aspx.

13. Institute, M. *Electricity*. 2014, [10/03/2014]; Available from: http://www.methanol.org/Energy/Turbines-and-Electricity.aspx?lang=es-ES.

14. Electric Power Research Institute, E. *Operational Flexibility Guidelines for Gas Turbine Low NOx Combustion Systems*. 2011 [01/10/2013]; Available from: http://www.epri.com/abstracts/Pages/ProductAbstract.aspx?ProductId=000000000001022094.

15. Cameron, L.R.J. and P.J. Bowen, *Novel cloud chamber design for 'transition range' aerosol combustion studies.* Process Safety and Environmental Protection, 2001. **79**(4): p. 197-205.

16. Griffiths, J.F. and J.A. Barnard. Flame and Combustion, ed. B.A. Professional. Vol. 3rd Edition. 1995, Galsgow.

17. Rallis, C.J. and A.M. Garforth, *The determination of laminar burning velocity.* Progress in Energy and Combustion Science, 1980. **6**(4): p. 303-329.

18. Liberman, M.A., *Introduction to physics and chemistry of combustion : explosion, flame, detonation*, 2008, Springer: Berlin.

19. Kuo, K.K., *Principles of combustion*. 2nd ed. ed. 1986, Hoboken, NJ John Wiley and Sons.

20. Bunsen, R. and H. Roscoe, *Photochemische Untersuchungen.* Annalen der Physik, 1857. **177**(6): p. 235-263.

21. Mallard, E. and H. Le Chatelier, *Recherches expérimentales et théoriques sur la combustion des mélanges gazeux explosives*, 1883, H.Dunod et E. Pinat: Paris.

22. Zeldovich, Y.B. and D.A. Frank-Kamenetsky, Acta Physicochim, 1938. **9**: p. 341.

23. Lewis, B. and G.v. Elbe, *Flame Propagation.* Proc. Combust. Inst., 1937. **2**: p. 183-188.

24. Stevens, F.W., *A constant pressure bomb*, 1923, National Advisory Committee for Aeronautics (NACA), Technical Report. p. 305-310.

25. Chamberlin, D.S. and D.R. Clarke, *Flame Speed of Hydrogen Sulfide.* Proc. Combust. Inst., 1928. **1**: p. 33-35.

26. Fiock, E.F. and C.F. Marvin, *The Measurement of Flame Speeds.* Chemical Reviews, 1937. **21**(3): p. 367-387.

27. Lewis, B. and G. von Elbe, *Theory of Flame Propagation.* Chemical Reviews, 1937. **21**(2): p. 347-358.

28. Powling, J., *A New Burner Method for the Determination of Low Burning Velocities and Limits of Inflammability.* Fuel, 1949. **28**: p. 25-28.

29. Botha, J.P. and D.B. Spalding, *The Laminar Flame Speed of Propane/Air Mixtures with Heat Extraction from the Flame.* Proceedings of the Royal Society of London. Series A. Mathematical and Physical Sciences, 1954. **225**(1160): p. 71-96.

30. Tanford, C. and R.N. Pease, *Theory of Burning Velocity. II. The Square Root Law for Burning Velocity.* The Journal of Chemical Physics, 1947. **15**(12): p. 861-865.

31. Law, C.K., *Combustion Physics*. 2006, New York: Cambridge University Press.

32. Lieuwen, T., *Unsteady Combustor Physics*. 2012, Cambridge University Press.

33. Lewis, B. and G. Von Elbe, *Combustion, flames and explosions of gases. Third edition*. 1987. 763.

34. Andrews, G.E. and D. Bradley, *Determination of burning velocities: A critical review.* Combustion and Flame, 1972. **18**(1): p. 133-153.

35. Andrews, G.E. and D. Bradley, *The burning velocity of methane-air mixtures.* Combustion and Flame, 1972. **19**(2): p. 275-288.

36. Tseng, L.K., M.A. Ismail, and G.M. Faeth, *Laminar burning velocities and Markstein numbers of hydrocarbon/air flames.* Combustion and Flame, 1993. **95**(4): p. 410-426.

37. Wheeler, R.V., J. Chem. Soc. (London), 1918. **113**(840).

38. Payman, W., *Normal" Propagation of Flame in Gaseous mixtures.* Proc. Combust. Inst., 1928. **1**: p. 51-60.

39. Coward, H.F. and W. Payman, *Problems in Flame Propagation.* Proc.Combust. Inst., 1937. **2**: p. 189-193.

40. Karlovitz, B., Denniston Jr, D. W., Knapschaefer, D. H., and Wells, F. E., *Studies on Turbulent flames: A. Flame Propagation Across velocity gradients B. turbulence Measurement in flames.* Symposium (International) on Combustion, 1953. **4**(1): p. 613-620.

41. Markstein, G.H., *Experimental and Theoretical Studies of Flame-Front Stability.* Journal of the Aeronautical Sciences (Institute of the Aeronautical Sciences), 1951. **18**(3): p. 199-209.

42. Markstein, G.H., *Nonsteady Flame Propagation*. 1964, New York: The Macmillan Co.

43. Lewis, W.K.L., *The Evaporation of a liquid into a gas.* Transactions of the American Society of Mechanical Engineers, 1922. **1849**: p. 325-340.

44. Bradley, D., P.H. Gaskell, and X.J. Gu, *Burning velocities, Markstein lengths, and flame quenching for spherical methane-air flames: A computational study.* Combustion and Flame, 1996. **104**(1-2): p. 176-198.

45. Varea, E., Modica, V., Vandel, A., and Renou, B., *Measurement of laminar burning velocity and Markstein length relative to fresh gases using a new postprocessing procedure: Application to laminar spherical flames for methane, ethanol and isooctane/air mixtures.* Combustion and Flame, 2012. **159**(2): p. 577-590.

46. Gu, X.J., Haq, M. Z., Lawes, M. and Woolley, R., *Laminar burning velocity and Markstein lengths of methane-air mixtures.* Combustion and Flame, 2000. **121**(1-2): p. 41-58.

47. Dowdy, D.R., Smith, D. B., Taylor, S. C. and Williams, A., *The use of expanding spherical flames to determine burning velocities and stretch effects in hydrogen/air mixtures.* Symposium (International) on Combustion, 1991. **23**(1): p. 325-332.

48. Taylor, S.C., *BURNING VELOCITY AND THE INFLUENCE OF FLAME STRETCH*, 1991, The University of Leeds.

49. Tahtouh, T., F. Halter, and C. Mounaïm-Rousselle, *Measurement of laminar burning speeds and Markstein lengths using a novel methodology.* Combustion and Flame, 2009. **156**(9): p. 1735-1743.

50. Kelley, A.P. and C.K. Law, *Nonlinear effects in the extraction of laminar flame speeds from expanding spherical flames.* Combustion and Flame, 2009. **156**(9): p. 1844-1851.

51. Halter, F., T. Tahtouh, and C. Mounaïm-Rousselle, *Nonlinear effects of stretch on the flame front propagation.* Combustion and Flame, 2010. **157**(10): p. 1825-1832.

52. Wu, C.K. and C.K. Law, *On the determination of laminar flame speeds from stretched flames.* Symposium (International) on Combustion, 1985. **20**(1): p. 1941-1949.

53. Vagelopoulos, C.M. and F.N. Egolfopoulos, *Laminar flame speeds and extinction strain rates of mixtures of carbon monoxide with hydrogen, methane, and air.* Symposium (International) on Combustion, 1994. **25**(1): p. 1317-1323.

54. Kurata, O., S. Takahashi, and Y. Uchiyama, *Influence of preheat temperature on the laminar burning velocity of methane-air mixtures.* SAE Technical Papers, 1994.

55. Bonhomme, A., L. Selle, and T. Poinsot, *Curvature and confinement effects for flame speed measurements in laminar spherical and cylindrical flames.* Combustion and Flame, 2013. **160**(7): p. 1208-1214.

56. Bradley, D., M. Lawes, and M.S. Mansour, *Explosion bomb measurements of ethanol-air laminar gaseous flame characteristics at pressures up to 1.4 MPa.* Combustion and Flame, 2009. **156**(7): p. 1462-1470.

57. Ishizuka, S. and C.K. Law, *An experimental study on extinction and stability of stretched premixed flames.* Symposium (International) on Combustion, 1982. **19**(1): p. 327-335.

58. Maruta, K., Yoshida, M., Ju, Y. and Niioka, T., *Experimental study on methane-air premixed flame extinction at small stretch rates in microgravity.* Symposium (International) on Combustion, 1996. **26**(1): p. 1283-1289.

59. Guo, H., Ju, Y., Maruta, K., Niioka, T. and Liu, F., *Radiation extinction limit of counterflow premixed lean methane-air flames.* Combustion and Flame, 1997. **109**(4): p. 639-646.

60. Choudhuri, A.R., M. Subramanya, and S.R. Gollahalli, *Flame extinction limits of H2-CO fuel blends.* Journal of Engineering for Gas Turbines and Power, 2008. **130**(3).

61. Yu, G., C.K. Law, and C.K. Wu, *Laminar flame speeds of hydrocarbon + air mixtures with hydrogen addition.* Combustion and Flame, 1986. **63**(3): p. 339-347.

62. Zhu, D.L., F.N. Egolfopoulos, and C.K. Law, *Experimental and numerical determination of laminar flame speeds of methane/(Ar, N2, CO2)-air mixtures as function of stoichiometry, pressure, and flame temperature.* Symposium (International) on Combustion, 1989. **22**(1): p. 1537-1545.

63. Egolfopoulos, F.N., P. Cho, and C.K. Law, *Laminar flame speeds of methane-air mixtures under reduced and elevated pressures.* Combustion and Flame, 1989. **76**(3-4): p. 375-391.

64. Egolfopoulos, F.N. and C.K. Law, *Chain mechanisms in the overall reaction orders in laminar flame propagation.* Combustion and Flame, 1990. **80**(1): p. 7-16.

65. Egolfopoulos, F.N., D.L. Zhu, and C.K. Law, *Experimental and numerical determination of laminar flame speeds: Mixtures of C2-hydrocarbons with oxygen and nitrogen.* Symposium (International) on Combustion, 1991. **23**(1): p. 471-478.

66. Law, C.K., D.L. Zhu, and G. Yu, *Propagation and extinction of stretched premixed flames.* Symposium (International) on Combustion, 1988. **21**(1): p. 1419-1426.

67. Tsuji, H. and I. Yamaoka. *EXPERIMENTAL STUDY OF EXTINCTION OF NEAR-LIMIT FLAMES IN A STAGNATION FLOW*. 1981.

68. Tsuji, H. and I. Yamaoka, *Structure and extinction of near-limit flames in a stagnation flow.* Symposium (International) on Combustion, 1982. **19**(1): p. 1533-1540.

69. Sato, J., *Effects of lewis number on extinction behavior of premixed flames in a stagnation flow*. Symposium (International) on Combustion, 1982. **19**(1): p. 1541-1548.

70. Egolfopoulos, F.N., H. Zhang, and Z. Zhang, *Wall effects on the propagation and extinction of steady, strained, laminar premixed flames.* Combustion and Flame, 1997. **109**(1-2): p. 237-252.

71. Kee, R.J., Miller, J. A. Evans, G. H. and Dixon-Lewis, G., *A computational model of the structure and extinction of strained, opposed flow, premixed methane-air flames.* Symposium (International) on Combustion, 1989. **22**(1): p. 1479-1494.

72. Egolfopoulos, F.N. and P.E. Dimotakis, *A comparative numerical study of premixed and non-premixed ethylene flames.* Combustion Science and Technology, 2001. **162**(1-6): p. 19-35.

73. Egolfopoulos, F.N., *Geometric and radiation effects on steady and unsteady strained laminar flames.* Symposium (International) on Combustion, 1994. **25**(1): p. 1375-1381.

74. Park, O., Veloo, P. S., Liu, N. and Egolfopoulos, F. N., *Combustion characteristics of alternative gaseous fuels.* Proc. Combust. Inst. , 2011. **33**: p. 887-894.

75. Veloo, P.S. and F.N. Egolfopoulos, *Studies of n-propanol, iso-propanol, and propane flames.* Combustion and Flame, 2011. **158**(3): p. 501-510.

76. Crayford, A.P., Bowen, P.J, de la Rosa, D. and Tam V. H. Y., *Laminar Burning Characteristics of Methane/Water-Vapour/air Flames*, in *Proceedings of the European Combustion Meeting 2011*2011: Cardiff, UK.

77. Chen, Z., M.P. Burke, and Y. Ju. *Effects of Lewis number and ignition energy on the determination of laminar flame speed using propagating spherical flames*. 2009.

78. Kim, H.H., Won, S. H., Santner, J., Chen, Z. and Ju, Y., *Measurements of the critical initiation radius and unsteady propagation of n-decane/air premixed flames.* Proceedings of the Combustion Institute, 2013. **34**(1): p. 929-936.

79. Rooney, P.E. and G.I. Sivashinsky, *A theoretical study of propagation and extinction of nonsteady spherical flame fronts.* SIAM Journal on Applied Mathematics, 1989. **49 (4)**: p. 1029-1046.

80. De La Rosa, D., Bowen, P. J., Crayford, A. P. and Valera-Medina, A., *Influence of ambient conditions on laminar burning velocity, ignition and flame extinction for ethanol-air mixtures*, 2012. p. 273-283.

81. Mizutani, Y. and A. Nakajima, *Combustion of fuel vapor-drop-air systems: Part I—Open burner flames.* Combustion and Flame, 1973. **20**(3): p. 343-350.

82. Mizutani, Y. and A. Nakajima, *Combustion of fuel vapor-drop-air systems: Part II—Spherical flames in a vessel.* Combustion and Flame, 1973. **20**(3): p. 351-357.

83. Hayashi, S., S. Kumagai, and T. Sakai, *PROPAGATION VELOCITY AND STRUCTURE OF FLAMES IN DROPLET-VAPOR-AIR MIXTURES.* Combustion Science and Technology, 1977. **15**(5-6): p. 169-177.

84. Wilson, C.T.R., *Condensation of Water Vapour in the Presence of Dust-Free Air and Other Gases.* Phil Trans R Soc A, 1897. **189**: p. 265-307.

85. Polymeropoulos, C.E., *Flame Propagation in Aerosols of Fuel Droplets, Fuel Vapor and Air.* Combustion Science and Technology, 1984. **40**(5-6): p. 217-232.

86. Burgoyne, J.H. and L. Cohen, *The Effect of Drop Size on Flame Propagation in Liquid Aerosols.* Proceedings of the Royal Society of London. Series A. Mathematical and Physical Sciences, 1954. **225**(1162): p. 375-392.

87. Ballal, D.R. and A.H. Lefebvre, *Flame propagation in heterogeneous mixtures of fuel droplets, fuel vapor and air.* Symposium (International) on Combustion, 1981. **18**(1): p. 321-328.

88. Law, C.K. and S.H. Chung, *An Ignition Criterion for Droplets in Sprays.* Combustion Science and Technology, 1980. **22**(1-2): p. 17-26.

89. Law, C.K., S.H. Chung, and N. Srinivasan, *Gas-phase quasi-steadiness and fuel vapor accumulation effects in droplet burning.* Combustion and Flame, 1980. **38**(C): p. 173-198.

90. Myers, G.D. and A.H. Lefebvre, *Flame propagation in heterogeneous mixtures of fuel drops and air.* Combustion and Flame, 1986. **66**(2): p. 193-210.

91. Greenberg, J.B., A.C. McIntosh, and J. Brindley, *Instability of a flame front propagating through a fuel-rich droplet-vapour-air cloud.* Combustion Theory and Modelling, 1999. **3**(3): p. 567-584.

92. Lawes, M., Y. Lee, and N. Marquez, *Comparison of iso-octane burning rates between single-phase and two-phase combustion for small droplets.* Combustion and Flame, 2006. **144**(3): p. 513-525.

93. Nomura, H., Kawasumi, I., Ujiie, Y. and Sato, J., *Effects of pressure on flame propagation in a premixture containing fine fuel droplets.* Proceedings of the Combustion Institute, 2007. **31 II**: p. 2133-2140.

94. Neophytou, A. and E. Mastorakos, *Simulations of laminar flame propagation in droplet mists.* Combustion and Flame, 2009. **156**(8): p. 1627-1640.

95. Bradley, D., Lawes, M.,cLiao, S. and Saat, A., *Laminar mass burning and entrainment velocities and flame instabilities of i-octane, ethanol and hydrous ethanol/air aerosols.* Combustion and Flame, 2014.

96. Atzler, F., Demoulin, F. X., Lawes, M., Lee, Y. and Marquez, N., *Burning rates and flame oscillations in globally homogeneous two-phase mixtures (flame speed oscillations in droplet cloud flames).* Combustion Science and Technology, 2006. **178**(12): p. 2177-2198.

97. Greenberg, J.B., A.C. McLntosh, and J. Brindley, *Linear stability analysis of laminar premixed spray flames.* Proceedings of the Royal Society A: Mathematical, Physical and Engineering Sciences, 2001. **457**(2005): p. 1-31.

98. Lawes, M. and A. Saat. *Burning rates of turbulent iso-octane aerosol mixtures in spherical flame explosions*. 2011.

99. Bradley, D., Lawes, M.,vLiu, K. and Mansour, M. S., *Measurements and correlations of turbulent burning velocities over wide ranges of fuels and elevated pressures.* Proceedings of the Combustion Institute, 2013. **34**(1): p. 1519-1526.

100. Research, D.o.C.a.I., *Schlieren Methods*. Vol. 31. 1963: National Physical Laboratory.

101. Lawes, M., Ormsby, M. P., Sheppard, C. G. W. and Woolley, R., *Variation of turbulent burning rate of methane, methanol, and iso-octane air mixtures with equivalence ratio at elevated pressure.* Combustion Science and Technology, 2005. **177**(7): p. 1273-1289.

102. Crayford, A.P., *Suppression of Methane-Air Explosions with Water in the form of 'Fine' Mists*, 2004, University of Wales Cardiff.

103. Pugh, D.G., O'Doherty, T., Griffiths, A. J., Bowen, P. J., Crayford, A. P. and Marsh, R., *Sensitivity to change in laminar burning velocity and Markstein length resulting from variable hydrogen fraction in blast furnace gas for changing ambient conditions.* International Journal of Hydrogen Energy, 2013. **38**(8): p. 3459-3470.

104. Dreizler, A., Lindenmaier, S., Maas, U., Hult, J., Aldén, M. and Kaminski, C. F., *Characterisation of a spark ignition system by planar laser-induced fluorescence of OH at high repetition rates and comparison with chemical kinetic calculations.* Applied Physics B: Lasers and Optics, 2000. **70**(2): p. 287-294.

105. Pugh, D., *PhD Thesis Combustion characterisation of compositionally dynamic steelworks gases*, in *School of Engineering*2013, Cardiff University.

106. Mansour, M.S., *Fundamental Study of Premixed Combustion Rates at Elevated Presure and Temperature*, 2010, University of Leeds.

107. Egolfopoulos, F.N., Hansen, N., Ju, Y., Kohse-Höinghaus, K., Law, C. K. and Qi, F., *Advances and challenges in laminar flame experiments and implications for combustion chemistry*. Progress in Energy and Combustion Science, 2014. **43**(0): p. 36-67.

108. Bradley, D., Hicks, R. A., Lawes, M., Sheppard, C. G. W. and Woolley, R., *The measurement of laminar burning velocities and Markstein numbers for iso-octane-air and iso-octane-n-heptane-air mixtures at elevated temperatures and pressures in an explosion bomb.* Combustion and Flame, 1998. **115**(1-2): p. 126-144.

109. Lamoureux, N., N. Djebaïli-Chaumeix, and C.E. Paillard, *Laminar flame velocity determination for H2-air-He-CO2 mixtures using the spherical bomb method.* Experimental Thermal and Fluid Science, 2003. **27**(4): p. 385-393.

110. Pink, I.P., *Critical analysis of combustion characteristics of the Cardiff Cloud Combustor* 2006, University of Wales Cardiff.

111. Clavin, P., *Dynamic behavior of premixed flame fronts in laminar and turbulent flows.* Progress in Energy and Combustion Science, 1985. **11**(1): p. 1-59.

112. Smith GP, B.C., Frenklach M, Gardiner WC. *GRI Mech3.0 chemical kinetic mechanism*. 1999; Available from: http://www.me.berkeley.edu/grimech.

113. Williams, F.A. *Center for Energy Research*. 01/11/2009; Available from: http://web.eng.ucsd.edu/mae/groups/combustion/index.html.

114. Burke, M.P., Chen, Z., Ju, Y. and Dryer, F. L., *Effect of cylindrical confinement on the determination of laminar flame speeds using outwardly propagating flames.* Combustion and Flame, 2009. **156**(4): p. 771-779.

115. Zhang, Z., Huang, Z., Wang, X., Xiang, J. and Miao, H., *Measurements of laminar burning velocities and Markstein lengths for methanol-air-nitrogen mixtures at elevated pressures and temperatures.* Combustion and Flame, 2008. **155**: p. 358 - 368.

116. Prathap, C., A. Ray, and M.R. Ravi, *Investigation of nitrogen dilution effects on the laminar burning velocity and flame stability of syngas fuel at atmospheric condition.* Combustion and Flame, 2008. **155**(1-2): p. 145-160.

117. MalvernInstrumentsLtd. *Spraytec Installation manual*. 1999; Available from: http://www.malvern.com.

118. MalvernInstrumentsLtd. *Spraytec User Manual*. 2007; Available from: http://www.malvern.com.

119. MalvernInstrumentsLtd. *Spraytec RTSizer Software user manual*. 2005; Available from: http://www.malvern.com.

120. Perry, R.H., D.W. Green, and J.O. Maloney, *Perry's chemical engineers' handbook.* 7th [International] ed ed. 1998, New York McGraw-Hill.

121. Mawhinney, J. and J. Richardson, Fire Technol., 1997. **33**(1): p. 54-90.

122. Acton, M.R., P. Sutton, and M.J. Wickens, *Investigation of the mitigation of gas cloud explosions by water sprays.* Gas engineering and management, 1991. **31**(7-8): p. 166-172.

123. Jones, A. and G.O. Thomas, *Mitigation of small-scale hydrocarbon-air explosions by water sprays.* Chemical Engineering Research and Design, 1992. **70**(A2): p. 197-199.

124. Thomas, G.O., *The quenching of laminar methane-air flames by water mists.* Combustion and Flame, 2002. **130**(1-2): p. 147-160.

125. Yang, W. and R.J. Kee, *The effect of monodispersed water mists on the structure, burning velocity, and extinction behavior of freely propagating, stoichiometric, premixed, methane-air flames.* Combustion and Flame, 2002. **130**(4): p. 322-335.

126. Modak, A.U., Abbud-Madrid, A., Delplanque, J. P. and Kee, R. J., *The effect of mono-dispersed water mist on the suppression of laminar premixed hydrogen-, methane-, and propane-air flames.* Combustion and Flame, 2006. **144**(1-2): p. 103-111.

127. Lentati, A.M. and H.K. Chelliah, *Dynamics of water droplets in a counterflow field and their effect on flame extinction.* Combustion and Flame, 1998. **115**(1-2): p. 158-179.

128. Sapko, M.J., A.L. Furno, and J.M. Kuchta, *QUENCHING METHANE-AIR IGNITIONS WITH WATER SPRAYS.* US Bur Mines Rep Invest, 1977(8214).

129. Ilbas, M., Crayford, A. P., Yilmaz, I., Bowen, P. J. and Syred, N., *Laminar-burning velocities of hydrogen-air and hydrogen-methane-air mixtures: An experimental study.* International Journal of Hydrogen Energy, 2006. **31**(12): p. 1768-1779.

130. Bradley, D. and C.M. Harper, *The development of instabilities in laminar explosion flames.* Combustion and Flame, 1994. **99**(3–4): p. 562-572.

131. Monteiro, E., Bellenoue, M., Sotton, J., Moreira, N. A. and Malheiro, S., *Laminar burning velocities and Markstein numbers of syngas-air mixtures.* Fuel, 2010. **89**(8): p. 1985-1991.

132. Tang, C., Huang, Z, Jin, C., He, J, Wang, J, Wang, X and Miao, H, *Laminar burning velocities and combustion characteristics of propane–hydrogen–air premixed flames.* International Journal of Hydrogen Energy, 2008. **33**(18): p. 4906-4914.

133. Miao, H., Ji, M., Jiao, Q., Huang, Q. and Huang, Z., *Laminar burning velocity and Markstein length of nitrogen diluted natural gas/hydrogen/air mixtures at normal, reduced and elevated pressures.* International Journal of Hydrogen Energy, 2009. **34**(7): p. 3145-3155.

134. Miao, H., Jiao, Q., Huang, Z. and Jiang, D., *Measurement of laminar burning velocities and Markstein lengths of diluted hydrogen-enriched natural gas.* International Journal of Hydrogen Energy, 2009. **34**(1): p. 507-518.

135. Huang, Z., Zhang, Y., Zeng, K., Liu, B., Wang, Q. and Jiang, D., *Measurements of laminar burning velocities for natural gas-hydrogen-air mixtures.* Combustion and Flame, 2006. **146**(1-2): p. 302-311.

136. Liao, S.Y., Jiang, D. M., Huang, Z. H., Shen, W. D., Yuan, C. and Cheng, Q., *Laminar burning velocities for mixtures of methanol and air at elevated temperatures.* Energy Conversion and Management, 2007. **48**(3): p. 857-863.

137. Liao, S.Y., Jiang, D. M., Huang, Z. H.,Zeng, K. and Cheng, Q., *Determination of the laminar burning velocities for mixtures of ethanol and air at elevated temperatures.* Applied Thermal Engineering, 2007. **27**(2-3): p. 374-380.

138. Law, C.K. and C.J. Sung, *Structure, aerodynamics, and geometry of premixed flamelets.* Progress in Energy and Combustion Science, 2000. **26**(4–6): p. 459-505.

139. Chen, Z. and Y. Ju, *Theoretical analysis of the evolution from ignition kernel to flame ball and planar flame.* Combustion Theory and Modelling, 2007. **11**(3): p. 427-453.

140. Chenglong, T., Zuohua, H., Jiajia, H., Chun, J., Xibin, W. and Haiyan, M., *Effects of N2 dilution on laminar burning characteristics of propane-air premixed flames.* Energy and Fuels, 2009. **23**(1): p. 151-156.

141. Wu, Y.C. and Z. Chen, *Asymptotic analysis of outwardly propagating spherical flames.* Acta Mechanica Sinica/Lixue Xuebao, 2012. **28**(2): p. 359-366.

142. Perry, R.H. and D.W. Green, *Perry's Chemical Engineers's Handbook*. 7th ed. 1997: McGraw Hill.

143. Darrieus, G., *Propagation d'un front de flamme: assai de the´orie des vitesses anomales de de´flagration par developpement spontane´ de la turbulence.*, in *6th Int. Cong. Appl. Mech.*1946: Paris.

144. Landau, L.D. and E.M. Lifshitz, *Fluid Mechanics*. 1987, Oxford: Pergamon.

145. Bradley, D., Sheppart, C. G. W., Woolley, R., Greenhalgh, D. A. and Lockett, R. D., *The development and structure of flame instabilities and cellularity at low Markstein numbers in explosions.* Combustion and Flame, 2000. **122**(1-2): p. 195-209.

146. Li, J., A. Kazakov, and F.L. Dryer, *Experimental and numerical studies of ethanol decomposition reactions.* The Journal of Physical Chemistry A, 2004. **108**(38): p. 7671-7680.